High Resolution Frequency to Time Domain Transformations Applied to the Stepped Carrier MRIS Measurements

Final Technical Report

June 24, 1992

Performed for NASA Langley Research Center

by

North Carolina State University
Department of Electrical and Computer Engineering
Box 7911
Raleigh, NC 27695

under NASA Grant NAG-1-1219

for the period

January 1, 1991 to June 30, 1992

NASA Technical Officer: Robert T. Neece
Principal Investigator: Sasan H. Ardalan

Abstract

Ybarra, Gary A. High Resolution Target Range Estimation in Inhomogeneous Media Using Millimeterwave Radar*. (Under the direction of Sasan H. Ardalan.)

Two narrow-band radar systems are developed for high resolution target range estimation in inhomogeneous media. They are reformulations of two presently existing systems such that high resolution target range estimates may be achieved despite the use of narrow bandwidth radar pulses. A double sideband suppressed carrier radar technique originally derived in 1962, and later abandoned due to its inability to accurately measure target range in the presence of an interfering reflection, is rederived to incorporate the presence of an interfering reflection. The new derivation shows that the interfering reflection causes a periodic perturbation in the measured phase response. A high resolution spectral estimation technique is used to extract the period of this perturbation leading to accurate target range estimates independent of the signal-to-interference ratio. A non-linear optimal signal processing algorithm is derived for a frequency-stepped continuous wave radar system. The resolution enhancement offered by optimal signal processing of the data over the conventional Fourier Transform technique is clearly demonstrated using measured radar data. A method for modelling plane wave propagation in inhomogeneous media based on transmission line theory is derived and studied. Several simulation results including measurement of non-uniform electron plasma densities that develop near the heat tiles of a space re-entry vehicle are presented which verify the validity of the model.

* This work was supported in part by the National Aeronautics and Space Administration Langley Research Center under Grant NAG-1-1219.

Table of Contents

List of Tables

List of Figures

List of Symbols

AFE	Aeroassist Flight Experiment
AM	amplitude modulation
AR	autoregressive
ARMA	autoregressive moving average
BW	bandwidth
c	free-space velocity of light ($3 \cdot 10^8$ m/s)
CFD	computational fluid dynamics
CW	continuous wave
$\delta(t)$	Dirac Delta unit impulse function
dco	digitally controlled oscillator
Δf	frequency increment beween steps
DSBSC	double sideband suppressed carrier
E	electric field
EM	electromagnetic
ε_r	relative permittivity or dielectric constant
f	frequency
f_c	critical frequency for electron plasma
FM	frequency modulation
F_M	modulation frequency
Γ	reflection coefficient
γ	propagation constant

H	magnetic field
$H(j\omega)$	frequency response
$h(t)$	impulse response
HP	Hewlett-Packard
IFFT	Inverse Fast Fourier Transform
J	objective function
LS	least squares
μ	permeability
MRIS	Microwave Reflectometer Ionization Sensor
N_e	electron density
PropMod	Propagation Modelling program
$\theta(f)$, $\theta(\omega)$	phase of the frequency response
Radar	radio detection and ranging
RCG	reaction cured glass
SIR	signal to interference ratio
t_d	time delay
TE	transverse electric
TM	transverse magnetic
v_g	group velocity
ω	angular frequency
z_0	characteristic impedance
z_p	plasma turning point standoff distance

Chapter 1

Introduction

This dissertation presents the reformulation of two presently existing radar systems such that narrow-band pulses may be utilized while achieving high resolution target ranging. Conventional pulsed radar achieves high resolution by transmitting large bandwidth pulses. If the medium in which the target is embedded has a frequency dependent inhomogeneity, then a wide-band pulse would be smeared in time due to dispersion because different frequency components of the pulse will travel at different velocities. The detection process used to measure the target range from the received pulses will produce significant error. Therefore, high resolution is not achievable using conventional pulsed radar if the propagation path contains any medium with a frequency dependent inhomogeneity.

The two radar systems developed in this dissertation are a frequency-stepped double sideband suppressed carrier (DSBSC) system and a frequency-stepped continuous wave (CW) system. Specifically, the stepped DSBSC process is derived to incorporate the presence of an interfering reflection. The derivation shows that the interfering reflection causes a periodic perturbation in the measured phase sequence. It is demonstrated that by applying a high resolution spectral estimation technique to these measurements, accurate target range estimates may be detected. For the stepped CW technique, a new optimal signal processing algorithm is derived for extracting highly resolved target range estimates. The range resolution achievable using the new optimal processing algorithm is clearly demonstrated using measured radar data.

In order to simulate the performance of the two radar systems, a model for electromagnetic (EM) plane wave propagation in inhomogeneous media is derived. Simulation results using this model are presented in the context of measuring non-uniform electron plasma densities that develop near the thermal protection heat tiles of a space re-entry vehicle. However, the model is much more general and can be used to simulate accurately EM propagation in any inhomogeneous medium.

1.1 Microwave and Millimeterwave Radar

There presently exist several schemes which utilize electromagnetic (EM) energy to determine the distance from an antenna to a reflective target. The process of detecting a target and its range using EM energy is referred to as radar, an acronym for **Ra**dio **D**etection **a**nd **R**anging. The primary objectives of a radar system are to determine the presence of a target and also its range, or distance from some reference point to the target. Other target properties that are capable of being detected by certain radar systems are its location, velocity, and physical dimensions [Collins, Skolnik]. The radar systems developed in this dissertation are specifically designed for estimating target range. However, with further signal signal processing, target velocity can be extracted from the data produced by either system. This extension remains as future research and is not addressed in this dissertation.

There are two main performance measures of a target range estimate: accuracy and resolution [Artech84, Wehner, Bird]. Accuracy refers to the difference between the true and estimated values of the range. Resolution is the

ability to detect two or more distinct scatterers when they are at approximately the same range. These two performance measures of range estimation are often confused and careful attention should be given to their difference.

The electromagnetic spectrum contains a very wide range of frequencies that are currently used for radar measurements. Radars can be designed and developed at any frequency at which EM energy can be generated and controlled. Most radar systems utilize frequencies in the microwave and millimeterwave regions. The frequency ranges associated with microwaves and millimeterwaves overlap. Together they span the EM spectrum from approximately 300 MHz to 300 GHz. The radars presented in this dissertation are designed to operate within this frequency range.

A radar system is typically designed to achieve superior performance for a specific set of measurement circumstances. For example, many applications require a long detection range [Artech 84]. In order to detect targets at long ranges, careful selection of the radar operating frequency is critical to avoid atmospheric absorption. Examples of other measurement circumstances which may dictate constraints on system design are need for covertness, tracking ability, classification or identification, adverse weather performance, and volume search [IEEE]. The radars developed in this dissertation do not consider these constraints. They are developed solely for the general purpose of producing accurate and highly resolved target range estimates. Specific system details that may be required for a particular application remain the responsibility of the specific system designer.

Traditional pulsed (constant frequency) radars rely on a narrow pulsewidth to provide the range resolution Δr, which is directly proportional to the pulsewidth [Wehner]

$$\Delta r \approx ct_p \tag{1.1.1}$$

where c is the velocity of EM propagation and t_p is the time duration of the radar pulse. A popular high resolution variation of traditional pulsed radar is frequency-chirp pulsed radar which has a range resolution Δr_s

$$\Delta r_s \approx \frac{c}{2\beta} \tag{1.2.1}$$

where β is the bandwidth of the frequency-chirped pulse. Frequency chirping is achieved by frequency modulating the transmitter pulse. The range resolution objective of the radar systems developed in this dissertation is on the order of 5 mm. In order to achieve this resolution using either traditional pulsed radar or its high resolution chirp variation would require a pulse with a minimum bandwidth of 30 GHz. If the target is embedded in a frequency dependent inhomogeneity, such a pulse would be smeared in time due to the dispersive medium and the range estimate will be highly erroneous. Hence, an alternative approach to the pulsed radar technique is required.

1.2 The Microwave Reflectometer Ionization Sensor

The primary motivation for this study has been a prospective NASA shuttle mission called the *Aeroassist Flight Experiment* (AFE). In this experiment, a small spacecraft is to be deployed by the shuttle and accelerated to atmospheric entry velocity. The unmanned craft will then be flown through the earth's atmosphere. During the 600s aeropass, the high temperature in the proximity of the non-ablating heat tiles will generate a dynamic electron plasma. The aerodynamic friction created will slow the craft, providing an aerobraking action. Following the aeropass, the AFE vehicle will attain a low earth orbit to be retrieved by the shuttle. One purpose of this experiment is to gather information for the development of aerobraking technology, which requires an accurate measurement of the electron plasma density profile. The plasma profile data will be used to confirm or improve the flow field predictions made by computational fluid dynamics. The system which will perform the plasma density measurements is called the Microwave Reflectometer Ionization Sensor (MRIS). The MRIS antennas will be mounted behind the stagnation region tile where the plasma flow field is expected to be laminar. Polarization is not an issue because the plasma density is expected to be constant in the transverse plane.

There exist several predictions of the plasma density profiles that are to be measured. One such prediction, based on Computational Fluid Dynamics (CFD), is considered to be one of the better predictions presently available [Ybarra2]. An example of a CFD predicted profile is shown in Fig. 1.2.1.

The distance values shown are referenced to the outer surface of the heat tiles of the AFE vehicle. Distances referenced from the heat tiles are referred to as *standoff* distances.

Electron plasma may be characterized by its relative dielectric constant [Chen] given by

$$\varepsilon_r = 1 - \frac{q^2 N}{m\varepsilon_0\omega^2(1-j\frac{\nu}{\omega})} \qquad (1.2.3)$$

where q is the electron charge, N is the electron density, m is electron mass, ε_0 is the permittivity of free space, ω is the angular frequency of propagating electromagnetic (EM) energy, and ν is the plasma collision frequency.

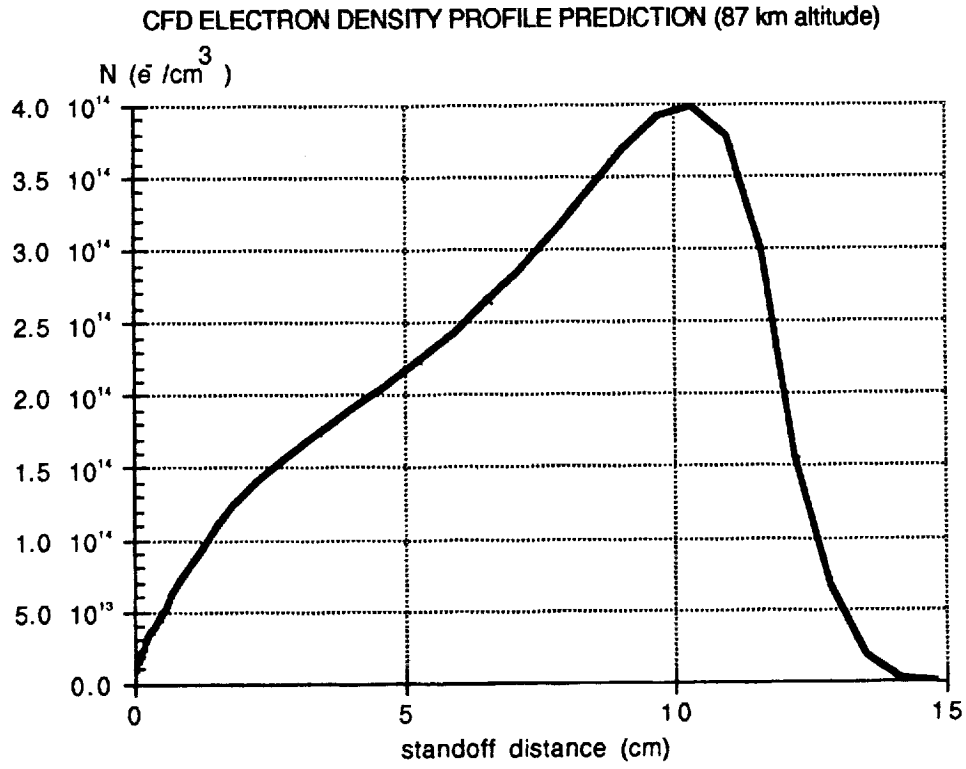

Figure 1.2.1 Computational fluid dynamics (CFD) prediction of the electron density profile at 87 km altitude.

$$\varepsilon_r = 1 - \frac{81N}{f^2} \tag{1.2.4}$$

where the EM frequency f is in kHz, and the electron density N is in e^-/cm^3. Unlike other materials, the group velocity v_g of EM energy in a plasma is the free-space velocity c scaled by $\sqrt{\varepsilon_r}$.

$$v_g = c\sqrt{\varepsilon_r} = c\sqrt{1 - \frac{81N}{f^2}} \tag{1.2.5}$$

There exists a critical frequency f_{cr} for a given electron density which occurs when $\varepsilon_r = 0$. At this point in the plasma, called the *turning point*, the plasma becomes a perfect reflector. That is, at the turning point, the reflection coefficient becomes $\Gamma = -1$, and interestingly the group velocity goes to zero. For frequencies much greater than f_{cr} , $\varepsilon_r \approx 1$ and the plasma behaves similar to free space. For Frequencies less than f_{cr} , $\varepsilon_r < 0$ the plasma behaves similar to a waveguide below its cut-off frequency. That is, only evanescent modes are present and no propagation occurs. As an example of a plasma density distance measurement, consider the CFD profile in figure 1.2.1. Suppose an EM wave is launched at a frequency of 140 GHz. The critical density, N_c, at this frequency may be calculated from (1.2.4) to be $2.42 \cdot 10^{14}$ e^-/cm^3 and is located at a standoff distance of 6 cm. The EM wave will penetrate into the plasma until it is reflected at the turning point and returns as an echo. If the round-trip travel time is measured and an average velocity of propagation is assumed, then an estimate of the standoff distance can be made. Although this technique is impractical due to the extremely small time interval, it serves to illustrate the plasma density measurement concept. The velocity of energy propagation in the

plasma varies with the electron density profile according to (1.2.5). However, if the electron density variation is linear with distance, then the average group velocity is approximated well by the convenient value c/2, where c is the free space velocity of light. Consider a linear electron density profile and its corresponding dielectric profile as shown in figure 1.2.2.

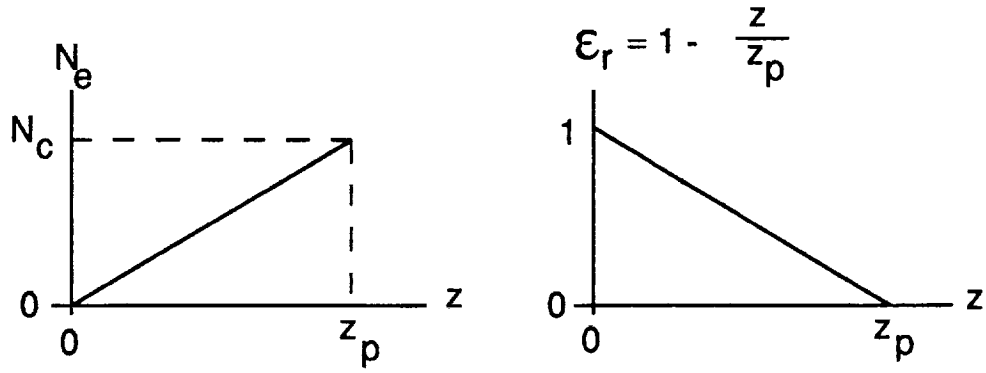

Figure 1.2.2 Linear electron plasma density profile and the corresponding dielectric profile.

The value of distance z_p is the location of the plasma turning point. It is assumed here that only a single EM frequency (monochromatic) is launched into the plasma. The group delay t_d within the plasma may be obtained analytically by integrating the inverse of the group velocity over distance.

$$t_d = \int_0^{z_p} \frac{dz}{v(z)} \qquad v(z) = c\sqrt{\varepsilon_r} = c\sqrt{1 - \frac{z}{z_p}} \tag{1.2.6}$$

$$t_d = \frac{1}{c} \int_0^{z_p} \frac{dz}{\sqrt{1 - \frac{z}{z_p}}} = \frac{z_p}{c} \int_0^1 \frac{du}{\sqrt{u}} = \frac{2z_p}{c} \sqrt{u} \Big|_0^1 = \frac{2z_p}{c} \tag{1.2.7}$$

This shows that the virtual distance to the turning point is twice the actual distance. Therefore the average group velocity is c/2 in an electron plasma whose density profile is linear with distance. The CFD predicted profile shown in Fig. 1.2.1 is not exactly linear, but it is close enough to warrant the use of c/2 as a first approximation to the average velocity.

It has been predicted by CFD that electron densities in the range of 10^{12} - 10^{15} e^-/cm^3 are expected to be encountered in the measurement range of 0-15 cm from the heat tile during the aeropass. In order to measure this electron density range, frequencies of 9-284 GHz would be required. Due to the MRIS system space and weight constraints, as well as practical microwave and millimeter wave sources, four center frequencies have been selected by NASA: 20, 44, 95, and 140 GHz. Thus, only four densities will be measured. Measurement of these four densities will be performed sequentially and repeated continuously for the first 500 seconds of the aeropass, and therefore can be tracked as a function of time. This information should provide enough data to accurately approximate the electron density profile as a function of time.

In order to launch an EM wave into the plasma, an antenna is mounted behind the heat tiles of the AFE vehicle. The propagation path is illustrated in Fig. 1.2.3. The thermal protection heat tile has a dielectric constant ε_r= 1.36. Thus, a small dielectric discontinuity occurs at the vacuum-tile interface which will cause a small strength spurious reflection. However, there is a thin Reaction Cured Glass (RCG) coating on the outer surface of the heat tile whose dielectric constant ε_r is 4.8. Therefore, a significant spurious reflection will occur at the tile-RCG interface. This reflection is considered interference and represents a significant obstacle for the plasma density measurement.

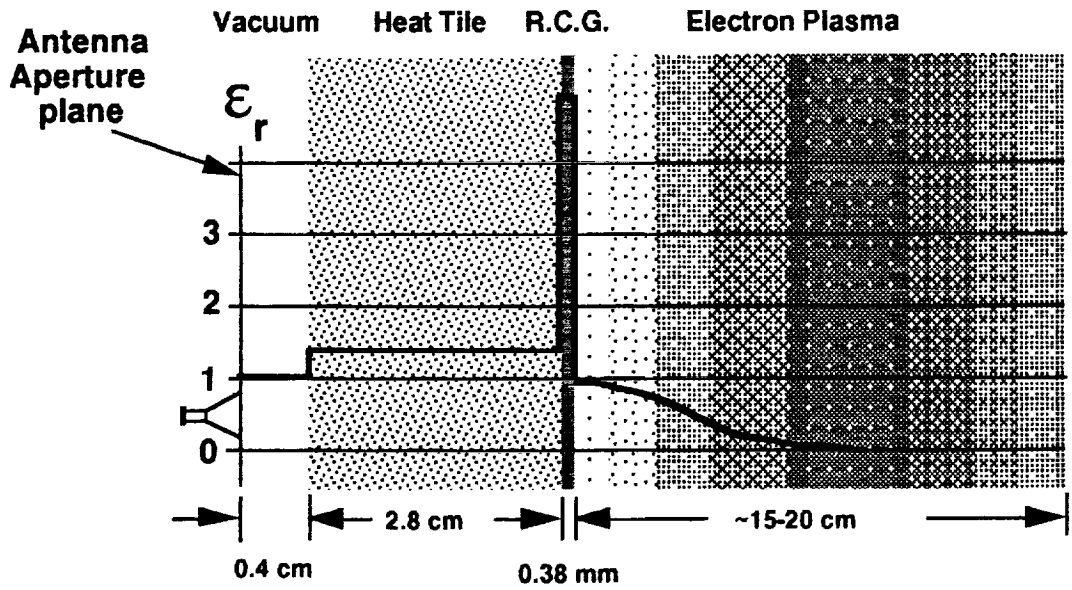

Figure 1.2.3 Microwave Reflectometer Ionization Sensor (MRIS) propagation path.

The simulation results that will be presented for the two radar systems developed in this dissertation will be in the context of measuring electron plasma densities as an example of measuring target range in frequency dependent inhomogeneous media. However, the systems are much more general and application dependency of their utility is not to be inferred.

1.3 Outline of Dissertation

This dissertation is organized as follows. In Chapter 2 a method for modelling EM planewave propagation in inhomogeneous media is derived. The derivation is based on the theory of transmission lines. An inhomogeneous medium is modelled by a cascade of thin slabs where each individual slab is

homogeneous. The boundary value problem for the electric and magnetic fields is solved at each slab boundary. It is demonstrated that for an exponential taper, as the thickness of the slabs approaches zero, the error in the fields generated by the model asymptotically approaches zero. The model is then used to illustrate the behavior of EM radiation in electron plasmas.

Chapter 3 presents the derivation of the frequency-stepped double sideband suppressed carrier (DSBSC) radar system. With certain modifications, this chapter appeared in [Ybarra2]. The newly derived system is an extension of the amplitude modulated (AM) CW technique [Nilssen] that was developed in the late 1950's as a result of the stimulated interest in radar from World War II. However, the AM CW technique was abandoned because severely erroneous target range estimates were obtained when an interfering reflection was present. The main contribution of this chapter is the derivation of the DSBSC system which includes the effect of an interfering reflection. It is shown that the interference can actually be used as a reference allowing accurate target range estimates to be extracted from the radar data, independent of signal to interference ratio. Simulation results for the DSBSC radar system are then presented in the context of measuring electron plasma densities.

The frequency-stepped continuous wave system is developed in Chapter 4. Several versions of this technique are currently in use [Artech 87, Bird, Davies1,2,3, Wehner]. The basic system that is examined in this chapter is a generalized system formulation of the Hewlett-Packard HP-8510 network analyzer [HP]. The function of this chapter is to present a detailed description of the mechanism by which the CW radar data is gathered. The objective of the stepped CW system is to extract frequency response samples from the

propagation path. Once the data is obtained, signal processing must be applied to generate the target range estimate. The standard approach is to take the Inverse Fast Fourier Transform (IFFT) of the frequency domain data resulting in a time domain impulse response. Peaks in the impulse response correspond to reflections whose time delay corresponds to the target range. Unfortunately, the range resolution offered by the IFFT is inversely proportional to the total bandwidth of the frequency range spanned by the frequency steps. This resolution handicap of the IFFT approach is the motivation for Chapter 5 which presents the derivation of an optimal signal processing algorithm for the stepped CW data. The range resolution enhancement offered by this new algorithm is clearly demonstrated by applying it to two different sets of physical measurements. The first set of data was obtained by measuring the reflection coefficient at the input of a coaxial verification standard [HP] terminated in a matched load by an HP-8510 network analyzer. These measurements were performed in the ECE Dept. microwave laboratory at NCSU. The second set of measurements were obtained at NASA Langley Research Center (LaRC). An HP-8510 network analyzer was used as a microwave source driving a test apparatus for the MRIS instrument. This apparatus is described in detail in Chapter 5. The optimal signal processing algorithm is applied to the MRIS test data and the results illustrate significant resolution enhancement over IFFT processing.

Finally, several future research objectives are proposed in Chapter 6 along with a final statement of the conclusions that have been drawn from the research comprising the dissertation.

Chapter 2

A Model for Electromagnetic Propagation in Inhomogeneous Media

In this chapter a method for modeling plane wave propagation of electromagnetic (EM) radiation in inhomogeneous media is derived and illustrated. The model uses cascaded slabs of homogeneous media and is based on the theory of EM wave propagation in transmission lines. Several applications have utilized the concept of cascaded slabs to model inhomogeneous media. It is well known that waveguides are dispersive [Collin]. One way of minimizing phase distortion due to dispersion is to implant slabs of dielectric in the waveguide [Keuster]. In the case of a single dielectric waveguide, analytical solutions are possible only for a few specific permittivity profiles in simple geometries. In general, the problem can only be solved numerically. Kuester examines the numerical problem for arbitrary dielectric profiles. However, his numerical solution is subject to the constraints that all media have constant permeability μ_0, and that the relative dielectric constant satisfies $\varepsilon_r \geq 1$ for all media. The model developed in this chapter is not bound by such constraints. One of the prevalent features of electron plasma is that its relative dielectric constant always satisfies $\varepsilon_r \leq 1$. Hence, a more general model is necessary for simulating propagation in plasma. In [Richmond] cascaded slabs of dielectric are used to model the effect of a temperature gradient on radomes. A very large temperature gradient in the radome of an aircraft often results from hypersonic flight through the atmosphere. The outer surface of the radome becomes hotter than the inside, resulting in a continuous variation in permittivity even if the radome was designed as a homogeneous structure.

Exact solutions in closed form are available only for a few special cases including linear and exponential inhomogeneities. In order to solve the radome problem, Richmond models the radome by a cascade of slabs, each of which is homogeneous. The procedure utilized is a step-by-step numerical integration of the first few terms of the power series expansion for the fields inside each slab. The technique is shown to produce results closely agreeing with experimental measurements. However, the case of frequency dependent inhomogeneities is not addressed and it is not clear how a reformulation could be made to incorporate frequency dependence. One of the primary contributions to this work from [Richmond] is the derivation of the relationship between slab thickness and modelling error. This topic will be discussed further in section 2.2.

Since the model developed in this chapter is intended for simulating EM plane wave propagation in any inhomogeneous medium, it must be capable of incorporating frequency dependence in both permeability μ and permittivity ε. There are several methods currently in use for modelling plane waves in plasmas which incorporate frequency dependence in their non-uniform permittivity. The majority of these methods approach the problem in terms of finding the solution to a Fredholm integral equation of either the first or second kind. The unknown profile index (either $\varepsilon(x)$ or $N_e(x)$) to be determined is contained in the integrand of one of the terms of the equation. Such approaches are termed profile inversion techniques [Ahn, Eden, Balanis1,2]. These profile inversion techniques appear to be as applicable to measuring inhomogeneous plasma densities as the cascaded slab model developed in this chapter. However, the solution of the Fredholm Integral equation for

arbitrary density profiles requires a linear approximation [Balanis2] as well as extensive computation. Therefore the need for developing other techniques for solving the plasma index profile problem exists. Reducing computational complexity while maintaining modelling accuracy is one of the primary motivations for current research in many engineering fields. The cascaded slab model developed in this chapter is implemented using the C programming language and incorporates the use of both recursive data structures and recursive programming techniques. The use of recursive programming techniques allows the simultaneous solution of all field quantities throughout the inhomogeneous medium. This leads to significantly reduced computation time over conventional programming techniques.

Other techniques for plasma density determination such as those based on the WKB approximation [Ahn, Bahar, Davies1,2,3] are capable of providing accurate profile density estimates only for certain profile shapes. The cascaded slab model developed in this chapter requires no constraints on the shape of the profile index for accurate characterization.

2.1 Electromagnetic (EM) Characterization of Inhomogeneous Media

Consider a vertically polarized EM plane wave propagating in a medium with permittivity ε_1 as illustrated in Fig. 2.1.1.

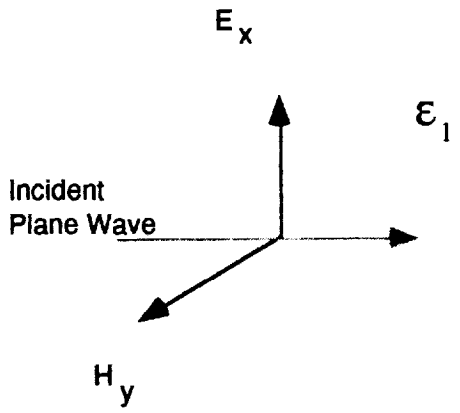

Figure 2.1.1. Plane Wave Propagation

It is assumed here that the electric field intensity varies only in the spatial direction x and the magnetic field varies only in the y direction. This assumption may be expressed analytically by the relations

$$E_y = E_z = 0 \qquad H_x = H_z = 0, \tag{2.1.1}$$

$$\frac{\partial E_x}{\partial x} = \frac{\partial E_x}{\partial y} = 0 \qquad \frac{\partial H_y}{\partial x} = \frac{\partial H_y}{\partial y} = 0 \tag{2.1.2}$$

Assuming time harmonic fields (sinusoidal), the time reduced form of Maxwell's two curl equations (Harrington) is

$$\frac{dE_x}{dz} = -j\omega\mu H_y \qquad \frac{dH_y}{dz} = -j\omega\varepsilon E_x \tag{2.1.3}$$

These equations are similar to the differential equations governing the relationship between voltage and current for lossless transmission lines,

$$\frac{dV}{dz} = -j\omega LI \quad \frac{dI}{dz} = -j\omega CV \tag{2.1.4}$$

Hence, the theory used to describe propagation in transmission lines applies equally as well to plane-wave propagation. Now consider the discontinuity at the boundary between two different media each having different dielectric constants as shown in Fig. 2.1.2. This condition is similar to the discontinuity that arises when two different transmission lines with different characteristic impedances are connected to each other as shown in Fig. 2.1.3.

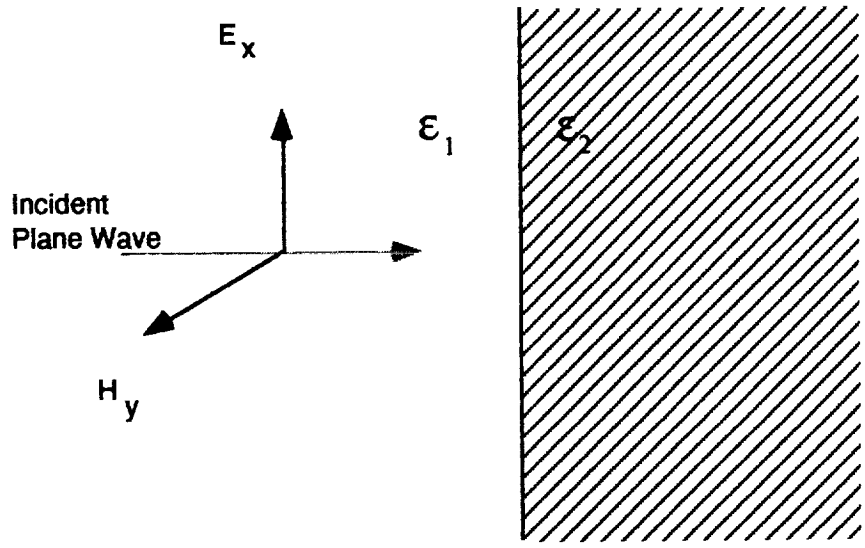

Figure 2.1.2. Plane wave incident normally on a dielectric discontinuity.

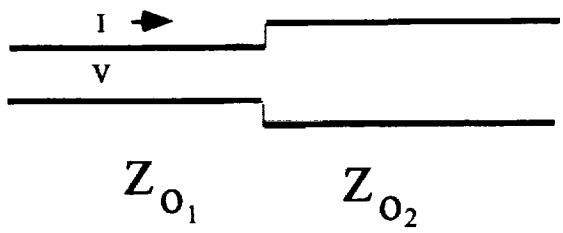

Figure 2.1.3. Transmission line discontinuity

The analogy between transmission lines and plane wave propagation (normal incidence) is summarized in Table 2.1.1. Note that the mismatch at the discontinuity is represented by a reflection coefficient for each case.

Table 2.1.1. Plane Wave-Transmission Line Analogy [Brown].

Transmission Line Quantity	*Symbol or Equation*	*Plane-Wave Quantity*	*Symbol or Equation*
Voltage	V	Electric field Intensity	E_x
Current	I	Magnetic field intensity	H_y
Inductance per unit length	L	Permeability	μ
Capacitance per unit length	C	Permittivity	ε
Characteristic impedance	$Z_0 = \sqrt{\frac{L}{C}}$	Intrinsic impedance	$\eta = \sqrt{\frac{\mu}{\varepsilon}}$
Phase-shift constant	$\beta = \omega\sqrt{LC}$	Phase-shift constant	$\beta = \omega\sqrt{\mu\varepsilon}$
Velocity of Propagation	$v = \frac{1}{\sqrt{LC}}$	Velocity of propagation	$v = \frac{1}{\sqrt{\mu\varepsilon}}$
Reflection Coefficient	$\Gamma_L = \frac{Z_L - Z_0}{Z_L + Z_0}$	Reflection coefficient at boundary between ε_1 and ε_2	$\Gamma = \frac{\eta_2 - \eta_1}{\eta_2 + \eta_1}$
Incident wave power	$P^+ = \frac{\lvert V^+\rvert^2}{2Z_0}$	Incident wave power density	$P^+ = \frac{\lvert E_x^+\rvert^2}{2\eta}$

Using the relationships provided by table 2.1.1, the problem of plane wave propagation through any number of discontinuities may be solved. Consider the system shown in figure 2.1.4 which is a cascade of multiple slabs each of which is homogeneous but whose combined structure is inhomogeneous. This problem may be solved by solving the equivalent transmission line problem shown also. Therefore, solving general transmission line networks is focussed upon first, and the problem of plane wave propagation is examined later in this section.

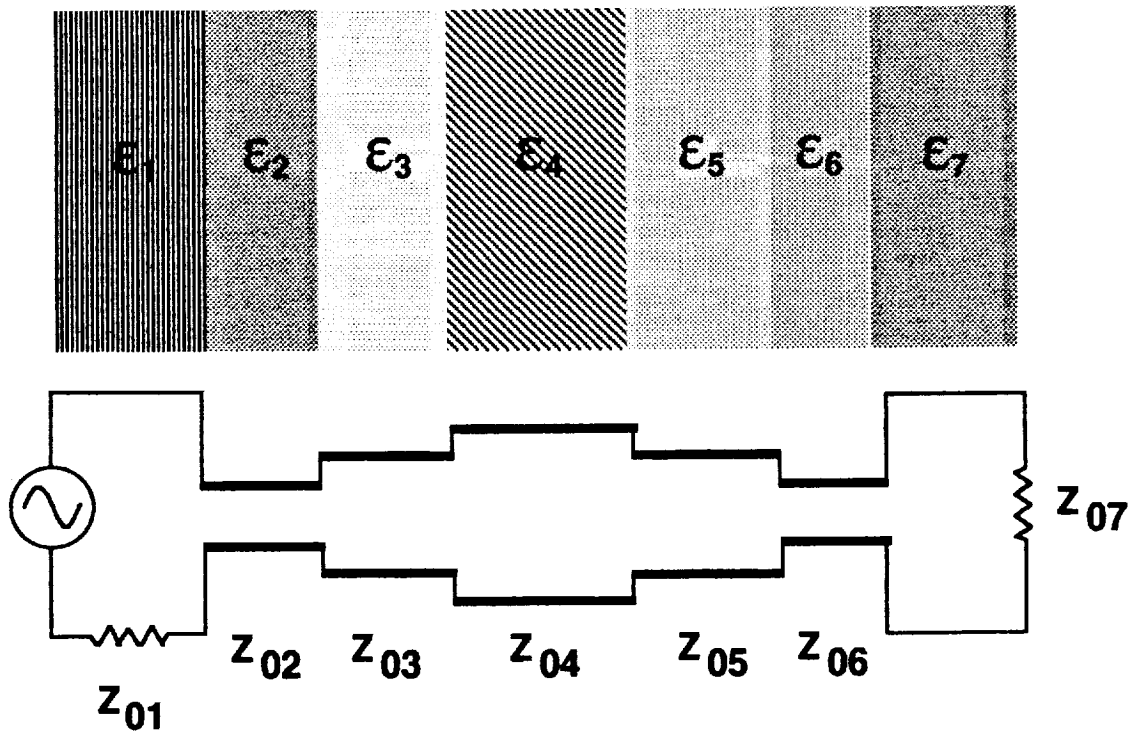

Figure 2.1.4. Modeling propagation through multiple layers of media as transmission line sections.

Consider the basic problem of simulating pulse transmission through a loaded transmission line. Assume that the pulse of interest is bandlimited with

a cutoff frequency of f_C . The pulse response can be obtained by first computing the frequency response of the network and then multiplying the frequency spectrum of the pulse by the frequency response of the transmission line network. Finally, the inverse Fast Fourier Transform (IFFT) of this product yields the time domain pulse response. Therefore, as a first step in calculating the frequency response of the network, the network response to a single sinusoid of frequency f_0 is analyzed. Consider the loaded transmission line connected to the generator V_S through a source impedance Z_S as shown in figure 2.1.5.

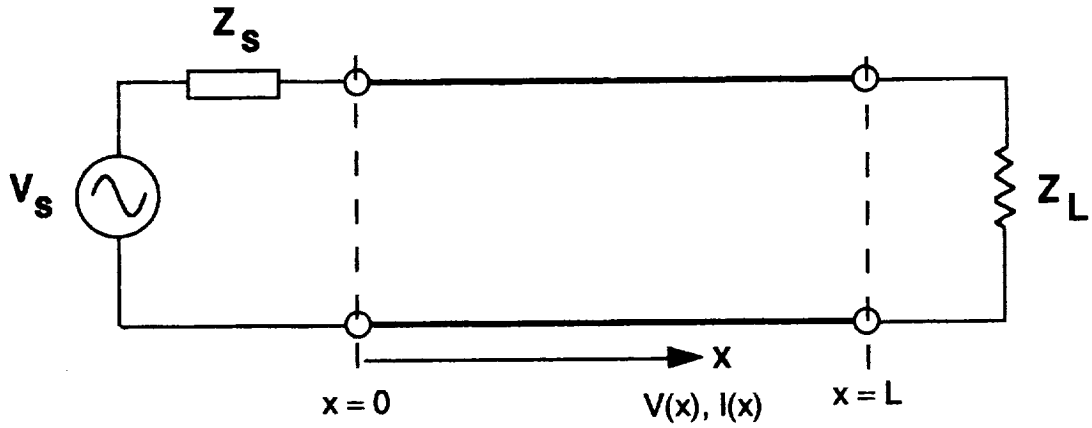

Figure 2.1.5. Generator connected to a loaded transmission line.

The voltage and current at any point on the transmission line can be obtained from the following expressions [LePage]

$$v(x) = \frac{V_s Z_0}{Z_0 + Z_s} e^{-\gamma x} \frac{1 + \Gamma_L e^{-2\gamma(L-x)}}{1 - \Gamma_s \Gamma_L e^{-2\gamma L}} \qquad (2.1.5)$$

$$i(x) = \frac{v_s}{z_0 + z_s} e^{-\gamma x} \frac{1 - \Gamma_L e^{-2\gamma(L-x)}}{1 - \Gamma_s \Gamma_L e^{-2\gamma L}} \tag{2.1.6}$$

In the above expressions the propagation constant γ is given by

$$\gamma = \sqrt{(r + j\omega l)(g + j\omega c)} \tag{2.1.7}$$

and the characteristic impedance z_0 of the transmission line is given by

$$z_0 = \sqrt{\frac{r + j\omega l}{g + j\omega c}} \tag{2.1.8}$$

where r,l,c, and g are the distributed resistance, inductance, capacitance, and conductance of the transmission line respectively. The expressions for the load and source reflection coefficients are

$$\Gamma_L = \frac{z_L - z_0}{z_L + z_0} \tag{2.1.9}$$

$$\Gamma_s = \frac{z_s - z_0}{z_s + z_0} \tag{2.1.10}$$

The expression for *v(x)* includes the superposition of all waves reflecting from the source and load mismatches. This can be seen by a Taylor series expansion of (2.1.5)

$$v(x) = \frac{v_s z_0}{z_0 + z_s} [\, e^{-\gamma x} + \Gamma_L e^{-\gamma(2L-x)} + \Gamma_L \Gamma_s e^{-\gamma(2L+x)} + \Gamma_L^2 \Gamma_s e^{-\gamma(4L-x)} + \Gamma_L^2 \Gamma_s^2 e^{-\gamma(4L+x)} + \ldots \,] \tag{2.1.11}$$

To obtain the shape of the pulse at the load, *v(L)* is evaluated at frequencies from *f=0* to *f=fc* in discrete steps where f_c is the cutoff frequency of the bandlimited pulse. Now consider the case where the boundary voltage and current are known on a section of transmission line as shown in figure 2.1.6.

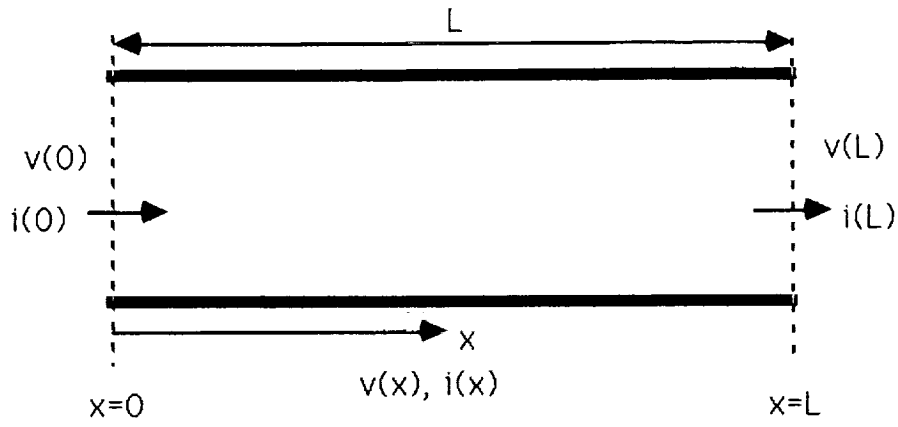

Figure 2.1.6. Section of transmission line with boundary voltages and currents

From (2.1.5) it can be shown that knowledge of the voltage at x=0, v(0), allows the voltage at any point along the line v(x) to be computed from the relation

$$\frac{v(x)}{v(0)} = e^{-\gamma x}\frac{1 + \Gamma_L e^{-2\gamma(L-x)}}{1 + \Gamma_L e^{-2\gamma L}} \qquad (2.1.12)$$

Similarly, the current at any point along the line i(x) may be computed by

$$\frac{i(x)}{i(0)} = e^{-\gamma x}\frac{1 - \Gamma_L e^{-2\gamma(L-x)}}{1 - \Gamma_L e^{-2\gamma L}} \qquad (2.1.13)$$

Thus, using (2.1.12) and (2.1.13) the voltage and current can be evaluated at any point on the transmission line given the boundary voltage and current. With the above preliminaries, a methodology for solving the simple network shown in figure 2.1.7 is presented. In this figure, terminal planes, or nodes have been labeled n_1 through n_5. To solve this network, that is to obtain the voltage and current at each node and at any location within the network, consider equation (2.1.5). This equation suggests that if the impedance at node n_1 were known, then the voltage and current at any location along the line can be calculated using knowledge of the source voltage and impedance. The first step is to obtain the impedance at n_1. This impedance is seen to consist of the parallel combination of the impedances looking into n_5 and n_2 from n_1.

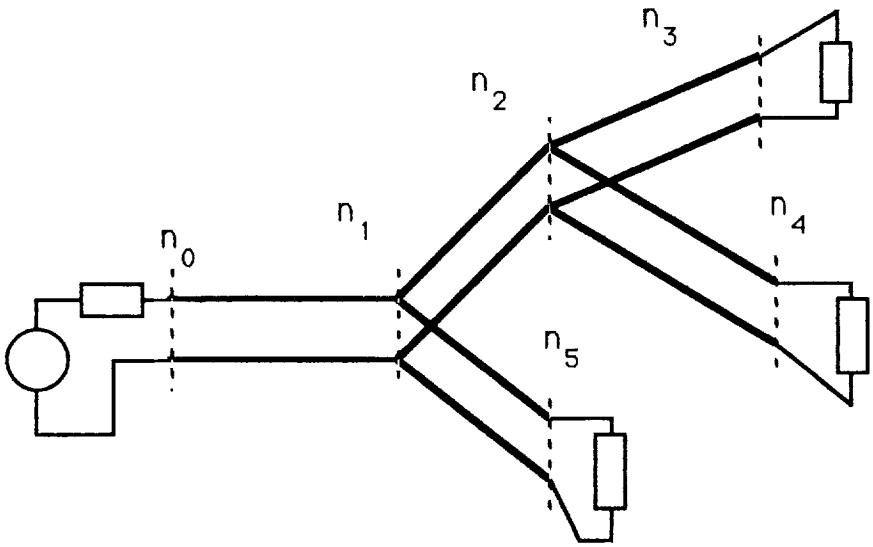

Figure 2.1.7. Simple transmission line network.

Consider the impedance looking into a single loaded transmission line as shown in figure 2.1.8.

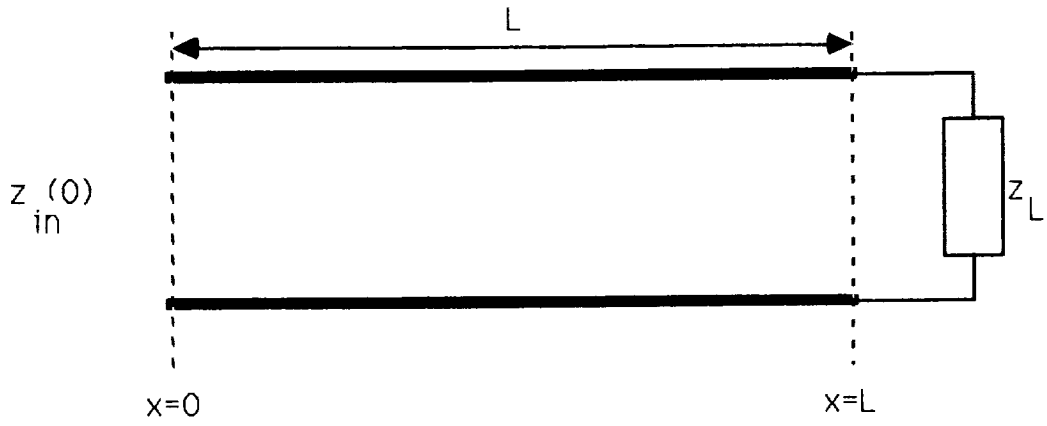

Figure 2.1.8. Input impedance of a loaded transmission line.

This impedance can be obtained from the relation [LePage]

$$Z_{in}(x) = \frac{1 + \Gamma_L e^{-2\gamma(L-x)}}{1 - \Gamma_L e^{-2\gamma(L-x)}} Z_0 \qquad (2.1.14)$$

The first step is to calculate the impedances looking into nodes n_3 and n_4 from n_2. The parallel combination forms the impedance at n_2. The impedance at n_1 is calculated by the parallel combination of the impedances looking into n_2 and n_5. Therefore, the following methodology may be used to solve the network. In the first pass, starting from the three loaded end nodes, the impedances are calculated, and the parallel combination of these impedances at the parent node forms the parent node impedance. Working backward in this manner, the impedance at the root node (n_1 in the example) is calculated. Using (2.1.5) and (2.1.6) the voltage and current at the root node n_1 may be calculated. Then using (2.1.12) and (2.1.13) and the boundary voltages and currents calculated

at the parent node, the voltage and current at each node in the network can be calculated.

In the special case of propagation through layers of different media, there are no branches. The transmission line analogy is illustrated in Figure 2.1.9.

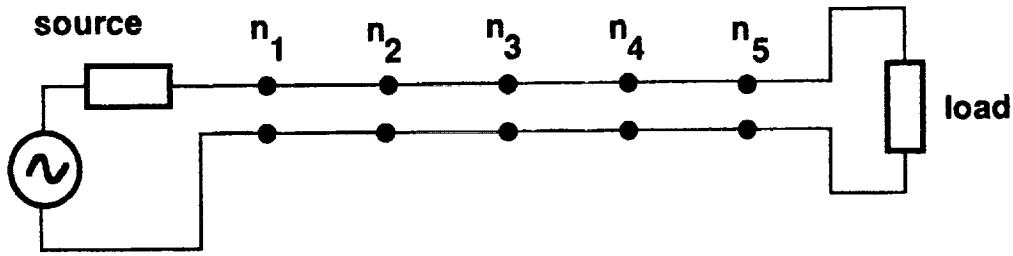

Figure 2.1.9. Network of cascaded sections.

In this case the impedance at node n_5 is computed first. Next, the impedance at node n_4 is computed and so forth until the total impedance looking into the network is obtained. In the next phase, the voltages and currents are computed starting from the source, node n_1, and then moving towards the load. Advanced computer programming techniques which utilize recursion can be implemented to efficiently perform these computations [Sobelman]. Transmission lines with a hundred thousand sections can be solved in only a few minutes of CPU time on a DEC 3100 workstation. It was shown by (2.1.3) and (2.1.4) that the plane wave propagation problem is equivalent to an analogous transmission line problem. Utilizing the relationships between transmission line parameters and those for plane wave propagation as illustrated in table 2.1.1 allows the fields within a system of cascaded slabs to be computed. In the next section, the accuracy of modelling inhomogeneous media with cascaded slabs is analyzed.

2.2 Accuracy of Modelling Inhomogeneous Media with Cascaded Slabs

In this section the accuracy of modelling an inhomogeneous medium with cascaded slabs is analyzed. Consider the transmission line illustrated in figure 2.2.1 which has an exponentially tapered characteristic impedance.

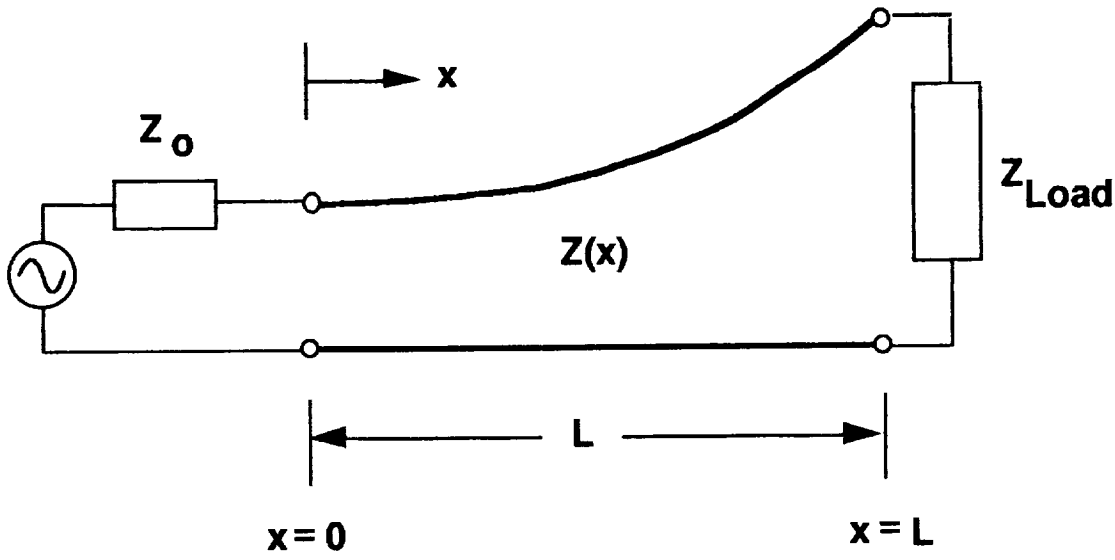

Figure 2.2.1 Exponentially tapered transmission line.

As a specific example, let the source have an impedance of 100 Ω, the load an impedance of 500 Ω, and total length of the exponentially tapered line be 10 m. The exponential taper can be created with two wire cable whose geometry is shown in figure 2.2.2.

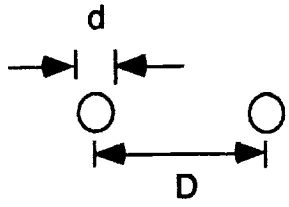

Figure 2.2.2 Parallel conductor transmission line geometry.

The distance separating the pair of conductors is D and the radius of each conductor is d. The characteristic impedance of this transmission line is [Brown]

$$Z_0 = 120 \ln\left(\frac{2D}{d}\right) \tag{2.2.1}$$

For the continuous exponential taper the normalized impedance anywhere along the line Z(x) is related to the geometry and load impedance through the relation

$$Z(x) = e^{\left[\frac{x}{L} \ln Z_{Load}\right]} \tag{2.2.2}$$

The exact differential equation relating the reflection coefficient to location along the line is [Collin]

$$\frac{d\Gamma}{dx} = j2\beta\Gamma - \frac{1}{2}\left(1 - \Gamma^2\right)\frac{d \ln Z(x)}{dx} \tag{2.2.3}$$

The exact solution to this Riccati differential equation for the input reflection coefficient is

$$\Gamma_i = \frac{A \sin\left(BL/2\right)}{B \cos\left(BL/2\right) + j\,2\beta \sin\left(BL/2\right)}$$

$$A = \frac{\ln Z_L}{L}, \quad B = \sqrt{4\beta^2 - A^2} \tag{2.2.4}$$

The normalized input impedance may be calculated from the input reflection coefficient using the relation

$$z_{in} = \frac{1 + \Gamma_{in}}{1 - \Gamma_{in}} \tag{2.2.5}$$

In order to test the model, sections of two wire transmission lines were cascaded. A comparison of the normalized input impedance as a function of θ obtained from the cascaded slab model and the exact solution to the Riccati equation (2.2.4 - 2.2.5) is shown in figures 2.2.3 and 2.2.4. The electrical length of the line θ is related to the wavelength λ and line length L through the relation

$$\theta = \beta L = \frac{2\pi}{\lambda} L \tag{2.2.6}$$

The best comparison is shown in figure 2.2.4 which is an enlarged view of figure 2.2.3. The simulation performed with 500 sections could not be distinguished from the exact solution. The conclusion is that the cascaded slab model produces the exact solution asymptotically as the number of sections is increased. The reason for this asymptotic exactness is that the model includes the effects of all reflections, not a simple approximation where second and higher order reflections are neglected.

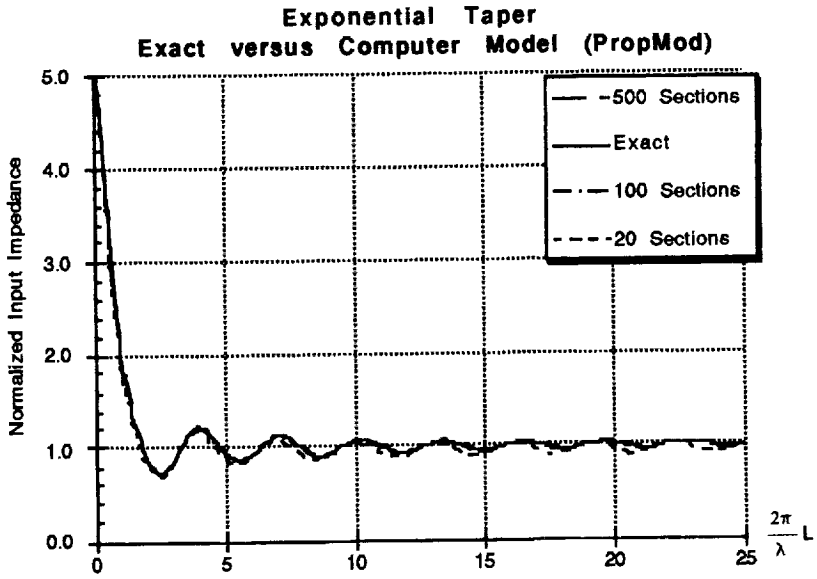

Figure 2.2.3 Comparison of the normalized input impedance produced by the cascaded slab model and the exact solution to the Riccati differential equation.

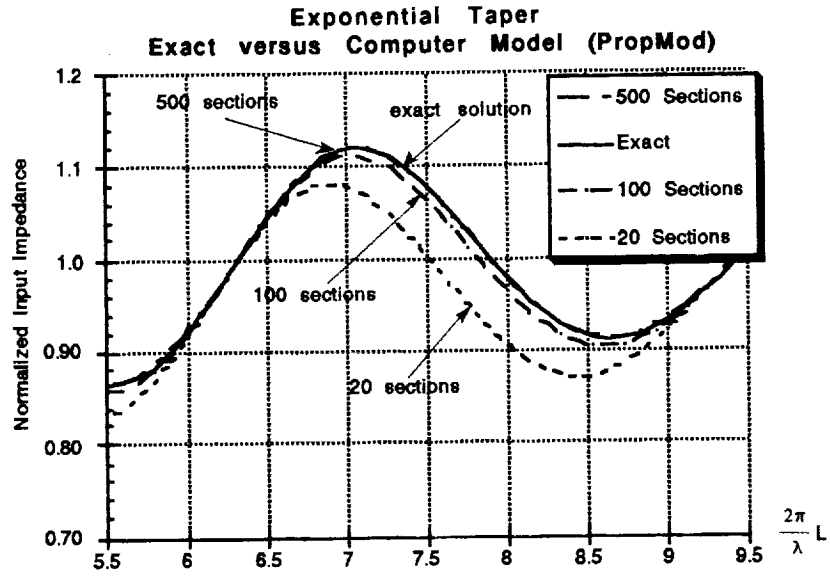

Figure 2.2.4 Detailed comparison of the normalized input impedance produced by the cascaded slab model and the exact solution to the Riccati differential equation.

From this single evaluation of the accuracy of modelling an exponentially tapered inhomogeneity, it remains unclear as to how many slabs are necessary to model accurately an arbitrary inhomogeneous medium. It has been shown [Richmond] that the error in modelling a frequency independent inhomogeneous medium with cascaded slabs is bounded by the two expressions

$$e(h) \le kh\sqrt{\varepsilon_r} \tag{2.2.7}$$

$$e(h) \le kh\left|\varepsilon_r' \sqrt{\varepsilon_r}\right|^{1/4} \tag{2.2.8}$$

where h is the slab thickness, k is the measurement uncertainty, ε_r' is the derivative of permittivity with respect to distance, and e(h) is the modelling error relative to the measurement error. The error bound (2.2.7) simply shows that reducing the step size reduces the modelling error. The more important of the two equations is (2.2.8) which shows that the step size h should be reduced when the slope of the permittivity profile is large (steep). This result obeys intuition since any spurious reflection will lead to modelling error. Spurious reflections will occur when the model produces discontinuities that are not present in the medium being modelled. When the profile slope is large, more slabs are needed to provide a smooth transition from one slab to the next. The derivation provided by Richmond considers only media with permittivity greater than one. Hence, the equations bounding the modelling error (2.2.7) and (2.2.8) cannot be applied to plasma profiles, where the permittivity is less than one. No error bound appears to exist in the literature for using cascaded slabs

to model inhomogeneous plasmas. The derivation of such a bound remains as future research stimulated by the work leading to this dissertation.

In order to model the plasma, the electron density profile is sliced into slabs of varying thickness, each characterized by its complex permittivity determined by (1.2.3). A dynamic slab thickness allocation algorithm should allocate slab thickness inversely proportional to the magnitude of the derivative of the dielectric profile with respect to distance as suggested by Richmond. This constraint is required to maintain smoothness in the dielectric profile of the model since the true inhomogeneous plasma has a continuous dielectric profile, and any sudden discontinuity in the dielectric will cause spurious reflections. With a plasma model, another consideration must be made. It is important that the modeling error be relatively small in the vicinity of the turning point. Therefore, considering slope and the turning point criterion, a dynamic slab width allocation algorithm was developed which considers both criteria in the allocation process. The algorithm is quite simple and is illustrated in figure 2.2.5. The number of sections per unit distance decreases linearly with increasing permittivity for linear profiles. Only 85% of the total allocation of sections are shown in the diagram. The remaining sections are evenly distributed between the turning point and the end of the profile which is located at a standoff distance of approximately 15 cm (see figure 1.2.1).

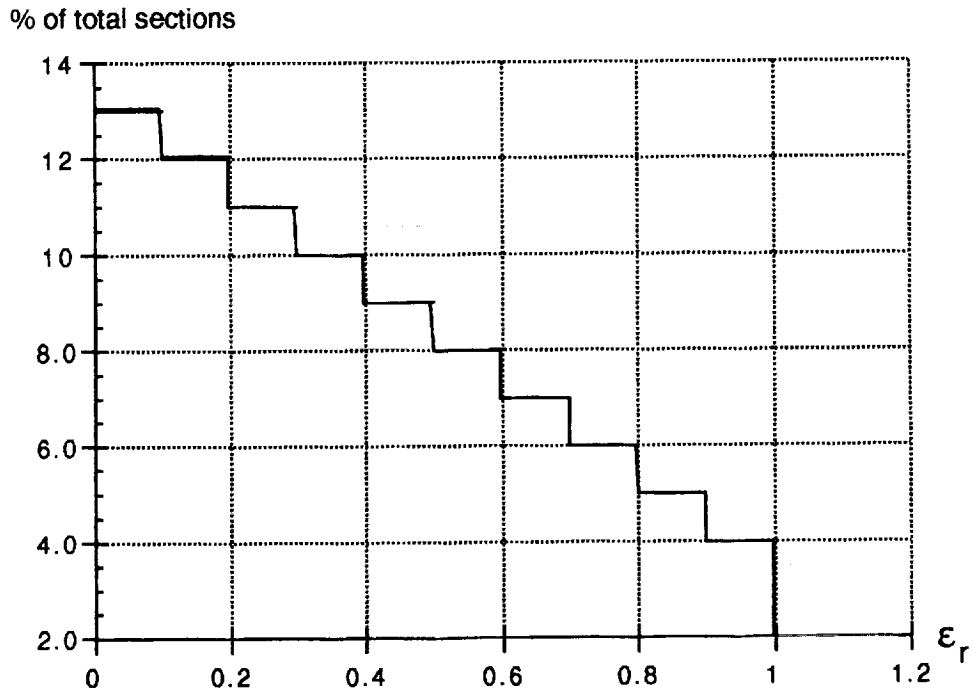

Figure 2.2.5 Dynamic allocation of plasma model slab widths.

Figure 2.2.6 shows what happens with this distribution for three differently shaped dielectric profiles. In the linear case, the slope is constant and therefore there is a linear increase in sections per distance as the turning point is approached. In the second case, the slope is near zero for nearly half the distance to the turning point and then the slope becomes increasingly larger (negative) causing the sections to compress nearer to the turning point. This is precisely what is desired, since the slope is steepest near the critical distance d_c. The third case shows the resulting trade-off between slope and dielectric value. The slope is large near the front edge of the profile and approaches zero near the critical point. Thus, the algorithm allocates relatively few sections in

the first few permittivity bins. However, this results in thinner slabs than would occur for a linear taper due to the large, negative slope in the permittivity profile. Then as the critical point is approached, the number of sections is increased because the permittivity is decreasing. However, because the slope approaches zero with increasing distance, the slab width actually increases slightly as the plasma turning point is approached, and a slope/turning point trade-off occurs as desired.

The total number of sections used in the slab model for accurate representation of the plasma was determined as follows. For the particular CFD profile used in the simulations, it was found that using more than 1000 sections made very little difference in any of the measurements. In order to assure an accurate plasma model for all measurement cases, 1500 sections were used in all simulations. Using 1500 sections resulted in section sizes ranging from a few microns to a few millimeters.

Although the cascaded slab model is capable of modelling accurately planewave propagation in plasmas, it must be pointed out that there is one significant drawback. In a physical measurement environment where the transmitted EM energy is emitted near the plasma, such as in the MRIS experiment, the resulting EM energy is not composed of planewaves. The energy spreads with range and no account of this energy spreading is currently provided by the cascaded slab model. Hence, one of the future research objectives is to include the effects of spherical wave transmission through the layers of media.

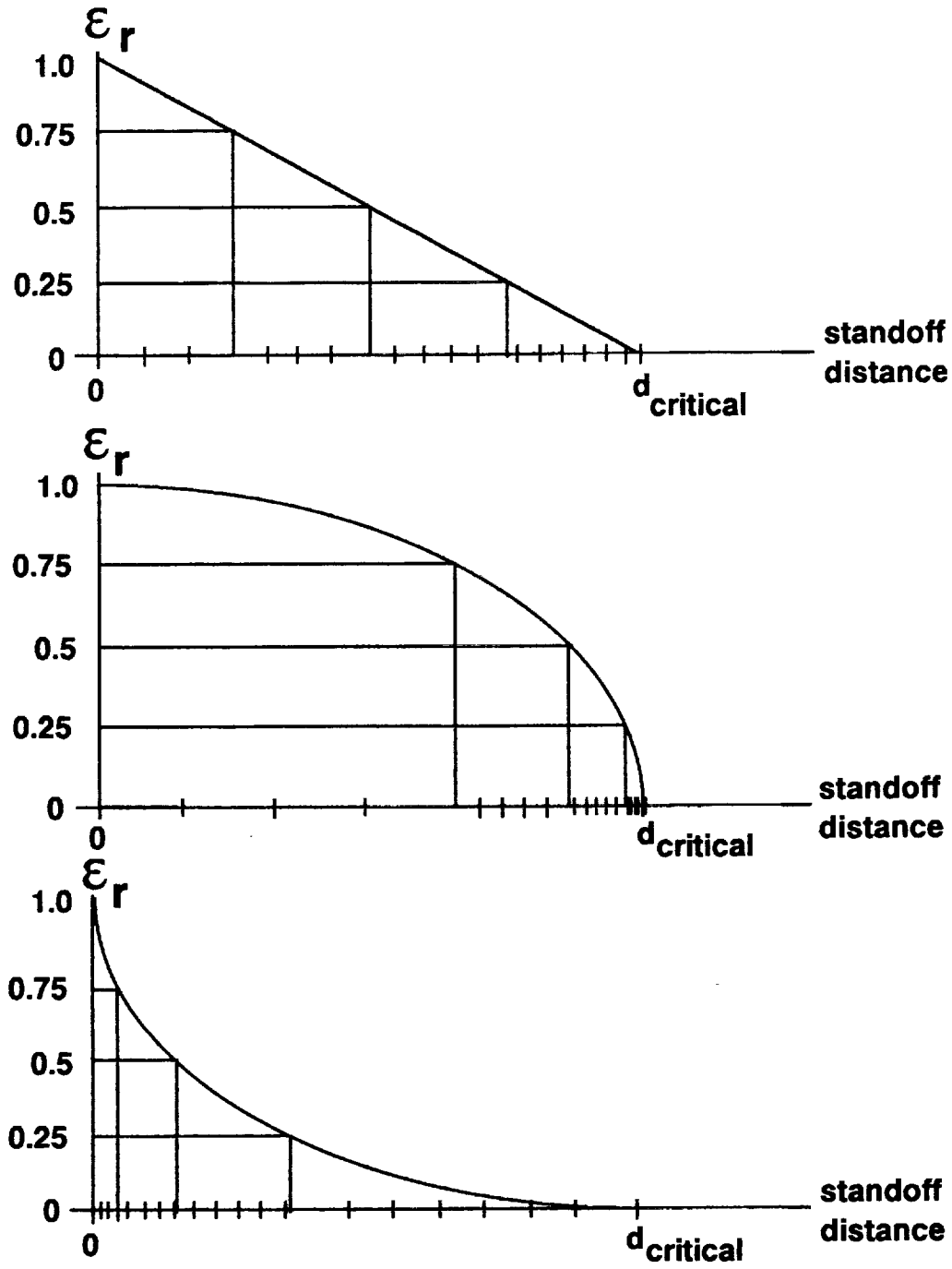

Figure 2.2.6 Illustration of the algorithm which dynamically allocates slab thicknesses in the plasma model for various permittivity profiles. Tick spacing indicates the relative number of sections used in the plasma model.

2.3 Obtaining Impulse and Frequency Responses of Channels Composed of Reflective Targets in Inhomogeneous Media

This section investigates the use of the cascaded slab model to obtain impulse and frequency responses of channels in which a reflective target is embedded in a dispersive, inhomogeneous medium. In each example, an electron plasma is used as the inhomogeneous medium. The electron plasma quantities used in the cascaded slab model are presented in table 2.3.1 [Chen].

Table 2.3.1. Electron plasma relationships used in the cascaded slab model.

Permittivity, n = electrons/cm^3	$\varepsilon = \varepsilon_0\varepsilon_r = \varepsilon_0\left(1 - \frac{81\,n}{f_{kHz}^2}\right)$
Intrinsic Impedance	$\eta = \sqrt{\frac{\mu}{\varepsilon}} = \frac{\eta_0}{\sqrt{1 - \frac{81\,n}{f_{kHz}^2}}}$
Propagation Constant	$\gamma = \alpha + j\,\beta = j\,\omega\sqrt{\mu_0\varepsilon_0}\sqrt{1 - \frac{81\,n}{f_{kHz}^2}}$
Group Velocity	$v_g = \frac{d\omega}{d\beta} = c\sqrt{1 - \frac{81\,n}{f_{kHz}^2}}$
Plasma Frequency, e = electron charge, m = electron mass	$\omega_p^2 = \frac{e^2 n}{m\varepsilon_0}$
Introduction of loss due to collision frequency ν	$\varepsilon = \varepsilon_0\left[1 - \frac{\omega_p^2}{\omega^2\left(1 - j\frac{\nu}{\omega}\right)}\right]$
Attenuation Constant	$\alpha = \frac{\eta_0 n e^2 \nu}{2m\left(\omega^2 + \nu^2\right)}$

As a first example, consider figure 2.3.1 which shows a constant density electron plasma sandwiched between two layers of air. A metal plate is placed against the second air layer. In this example, we are interested in the impulse response at the boundary of the first slab where it is assumed that a packet of plane waves is incident on the system. The electron density of the plasma is $44.5*10^{12}$ e^-/cm^3 corresponding to a critical frequency of 60 GHz.

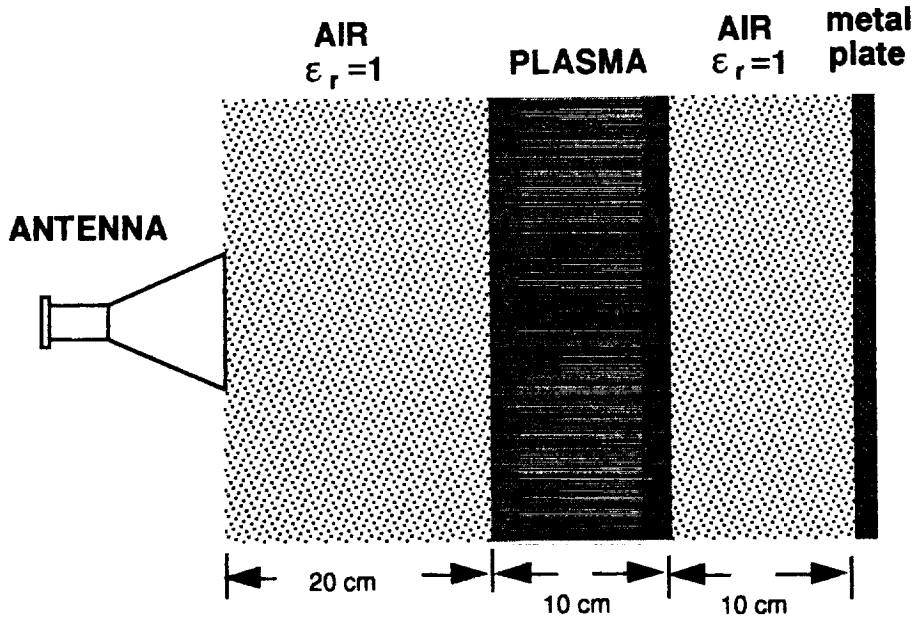

Figure 2.3.1 Channel composed of a constant density $N_e = 44.5 \cdot 10^{12}$ e^-/cm^3 electron plasma sandwiched between two slabs of air and terminated in a metal plate.

Two cases are now presented. In the first case, the impulse response over a bandwidth of 20 GHz at a starting frequency of 40 GHz is considered. For the second case, the same bandwidth is used but the beginning frequency is increased to 100 GHz. In both cases 512 frequency samples were obtained, which provides 1024 points in the resulting impulse response computed from a

512 point IFFT. The impulse response corresponding to the first case is shown in figure 2.3.2. The time domain data has been converted to the distance domain using the free-space velocity of propagation. In addition, consideration of the two-way travel time has been provided in the distance scale. Since the frequency span is 40 to 60 GHz, a strong reflection is observed from the plasma whose critical frequency is 60 GHz. The range to the reflection is 20 cm, precisely as expected from the channel geometry (figure 2.3.1).

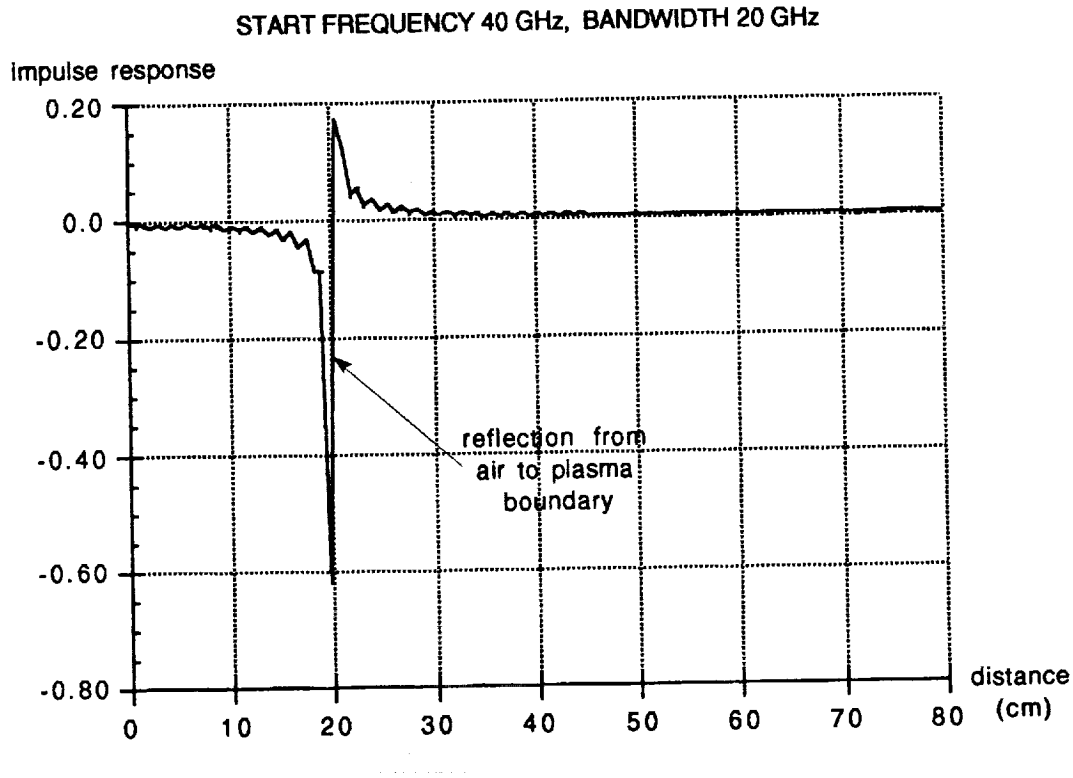

Figure 2.3.2 Impulse response of electron plasma sandwiched between air slabs and terminated in a metal plate. The starting frequency is 40 GHz.

In the second case, the frequency span is from 100 GHz to 120 GHz. The resulting impulse response is shown in figure 2.3.3.

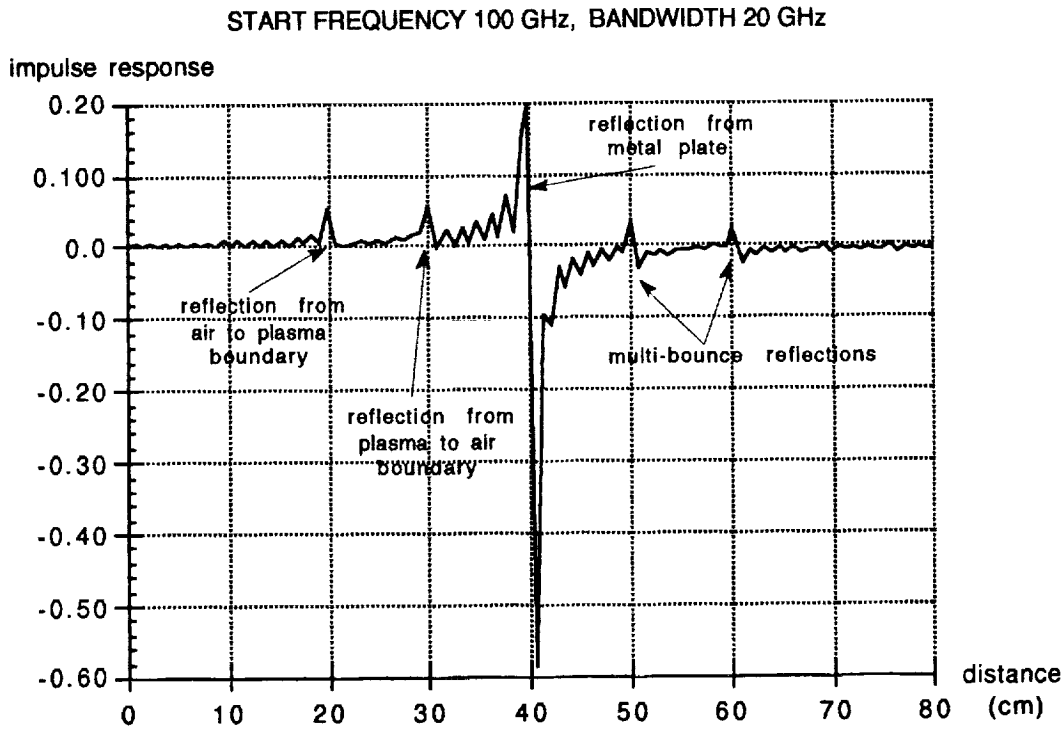

Figure 2.3.3 Impulse response of electron plasma sandwiched between air slabs and terminated in a metal plate. The starting frequency is 100 GHz.

Most of the energy passes through the plasma because its critical frequency is 60 GHz. However, there are minor reflections due to the dielectric discontinuities at the air/plasma interfaces. At 100 GHz, the dielectric constant of the plasma is $\varepsilon_r = 0.64$. The resulting reflections are shown in figure 2.3.3. The distance to the main reflection is shown to be 40 cm which corresponds to

the distance to the metal plate as indicated in figure 2.3.1. The velocity of propagation within the plasma has been taken into account.

In the next example, an analysis of propagation through the CFD electron density profile is presented. Consider the CFD profile shown in figure 2.3.4, which has been scaled so that the critical electron density at 20 GHz is located at a standoff distance of 4 cm. Note that the vertical axis is critical frequency and not electron density. The relationship between these two quantities was given in (1.2.4).

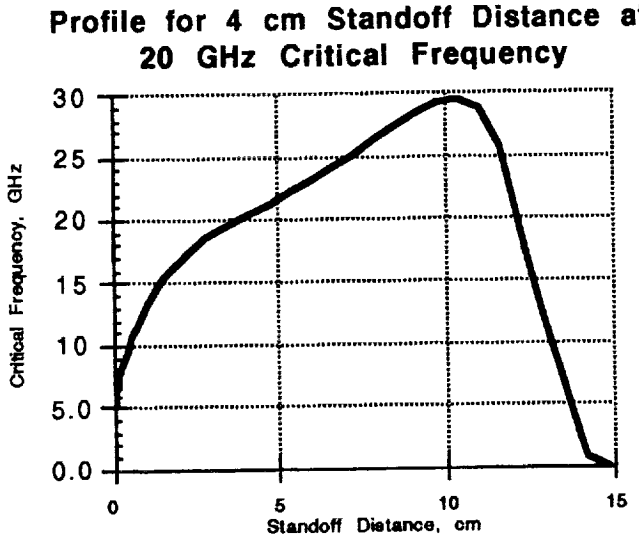

Figure 2.3.4 Scaled CFD electron density profile for 4 cm standoff at 20 GHz critical frequency.

This profile is placed outside the heat tile system of the AFE spacecraft which was shown in figure 1.2.3 so that the standoff distance is zero at the outer surface of the tile. The frequency response of the heat tile system and CFD profile is shown in figure 2.3.5. The reflected energy is added to the transmitted wave and forms an interference pattern. The sudden drop in reflected energy at 30 GHz corresponds to the maximum critical frequency in the CFD profile. The

periodic behavior of the frequency response beyond 30 GHz is due to the presence of the RCG only and its period is inversely proportional to the distance from the antenna aperture plane to this source of reflection.

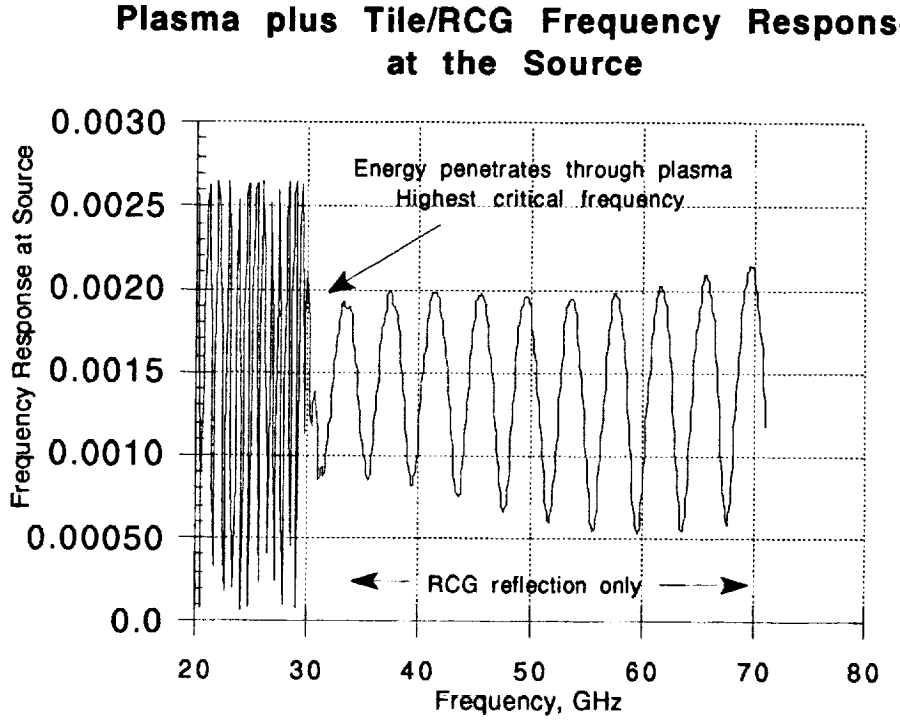

Figure 2.3.5 Tile/RCG and plasma frequency response as seen from the MRIS antenna flange.

Figure 2.3.6 shows a close-up view of the frequency response between 20 and 30 GHz. The distance between the nulls in the frequency response decreases as the frequency increases in an "accordion-like" effect. This is due to the fact that the turning point is getting farther away from the source.

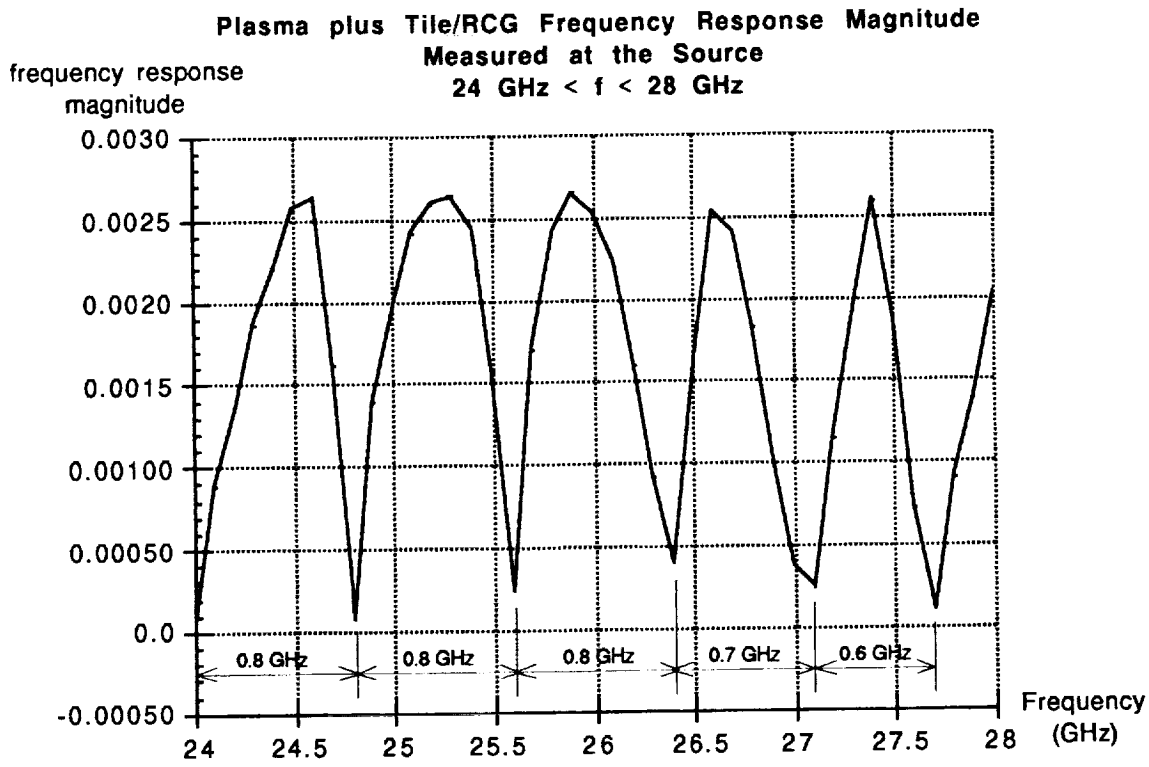

Figure 2.3.6 Close-up of plasma frequency response showing reflections from changing critical densities.

The next set of results provides great insight into the behavior of the plasma. Consider figure 2.3.7 which shows the impulse responses obtained using the cascaded slab model for the Tile/RCG CFD profile system using 64 frequency steps at 64 MHz intervals. This corresponds to the proposed measurement sequence for the MRIS instrument. Each impulse response corresponds to a different starting frequency as indicated. The frequencies are stepped in 64 MHz increments up to 64 steps. Therefore, the bandwidth of each measurement sequence is 4.096 GHz (64 x 64 MHz).

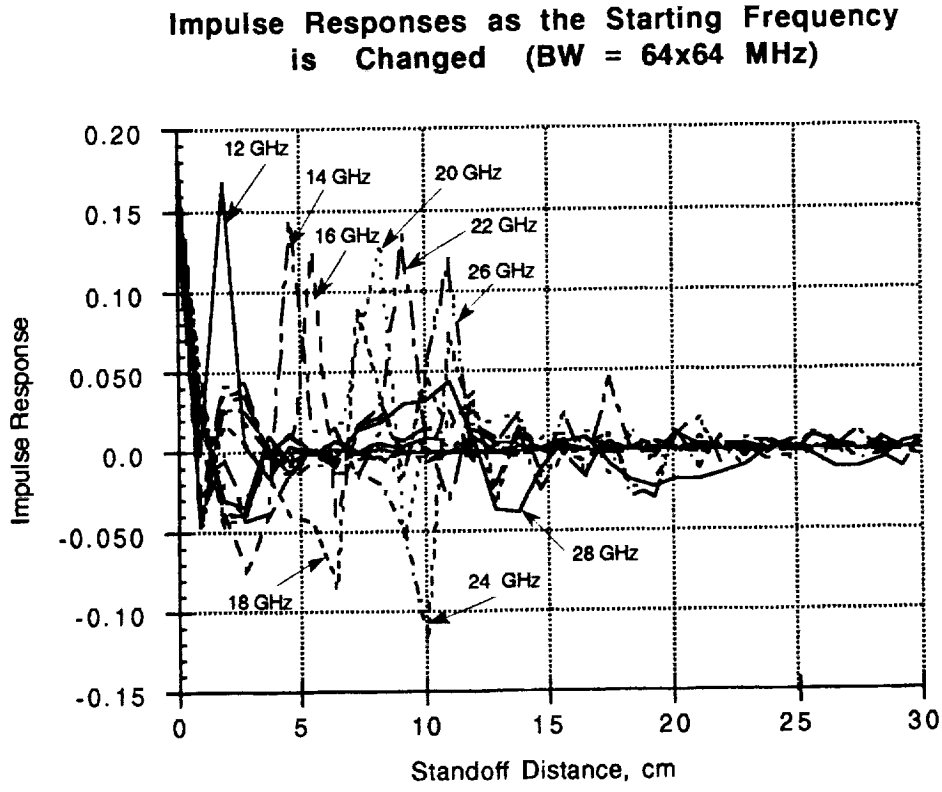

Figure 2.3.7 Impulse responses of the CFD profile as the starting frequency is changed.

The reflection from the plasma turning point moves outward, following the profile, as the starting frequency is increased. The turning point reflection may exhibit 180° phase shifts as in the case for 24 GHz. At 28 GHz, the top of the profile is skimmed (see figure 2.3.4). At 30 GHz and beyond there are no more plasma reflections. The only reflection is from the RCG, and all impulse responses are basically the same. The impulse responses up to 40 GHz in 2 GHz steps were computed and are shown in the graph.

An interesting view of the data from figure 2.3.7 is provided by the three dimensional plot shown in Figure 2.3.8. In this figure, all 15 impulse responses are plotted up to 18 cm standoff as indicated. The reflections below 30 GHz

start out close to the tile outer surface and then move out and eventually disappear. As the frequency increases beyond 30 GHz, the impulse responses all flatten out with no reflections other than those resulting from the tile.

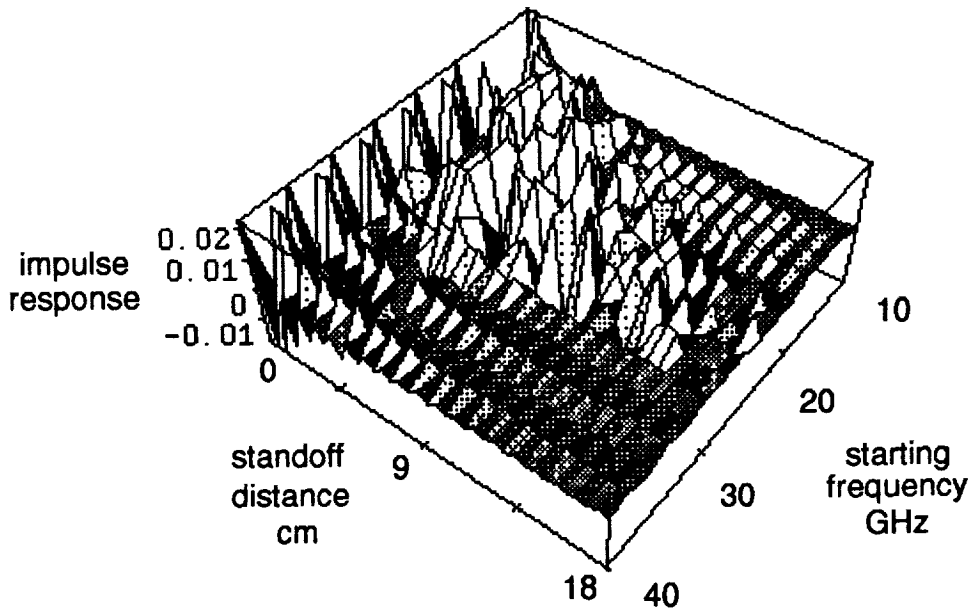

Figure 2.3.8 3 dimensional plot of impulse responses of Tile/RCG and CFD profile system as the starting frequency is changed.

2.4 Summary

A model for electromagnetic planewave propagation in inhomogeneous media was derived in this chapter and its performance illustrated in the context of modelling EM propagation in non-uniform electron plasmas. This model is based on the theory of transmission lines and represents an inhomogeneous medium by thin cascaded slabs, each of which is homogeneous but whose

combined structure is inhomogeneous. It has been shown that as the thickness of each slab is reduced, the response from the model asymptotically approaches the true physical response. The model can be implemented very efficiently using advanced computer programming techniques such as recursive programming which allow the use of hundreds of thousands of slabs while requiring little computation time.

Several simulation results have been presented in the context of measuring non-uniform electron plasma densities that develop near the heat tiles of a space re-entry vehicle. Unfortunately, an appropriate plasma profile cannot be produced for ground testing. Hence, with the exception of performing an actual atmospheric aeropass, their measurement can only be performed by computer simulation. For this reason, the inhomogeneous media model derived in this chapter, which can simulate accurately the propagation of planewaves in electron plasmas, is especially significant.

Chapter 3

The Frequency-Stepped Double Sideband Suppressed Carrier Radar System †

3.1 Introduction to the Frequency-Stepped DSBSC System

The double sideband (DSB) radar system derived and demonstrated in this chapter is a reformulation of the Amplitude Modulated CW radar system developed in 1962 [Nilssen]. Both systems extract target range information by observing the phase delay of the echo signal. The idea of using phase information to extract target range was first introduced in 1947 [Riden] during a time in which much effort was spent by scientists from several fields who joined in an effort to promote the development of practical radar systems. The AM CW radar technique has received little attention since its introduction in 1962, because the system requires the echo from the primary target to be much stronger than any other echo. The presence of an interfering reflection rendered the target range estimate useless. The DSB technique derived in section 3.2 can operate in the presence of an interfering reflection. It is shown that accurate target range may be extracted for virtually any signal-to-interference ratio (SIR). This immunity from weak target echoes is achieved by frequency-stepping the suppressed carrier and obtaining a sequence of phase measurements. The original formulation used only a single carrier frequency and for this reason was unable to mitigate the unwanted affects of interference.

A field closely related to radar is remote sensing of the atmosphere. There exists a region of the atmosphere called the ionosphere which is

† This chapter appeared, with certain modifications, in [Ybarra2].

characterized by a large number of oxygen and nitrogen ions resulting from solar radiation. The density of these ions is great enough to affect the propagation of radiowaves. The ionosphere begins at an approximate altitude of 50 km and reaches a maximum ion density at approximately 80 km. It has several unusual EM wave propagation properties. One of these properties is that it reflects radiowaves with certain frequencies somewhat similarly to a conductor. This reflection property allows certain radio frequencies to "skip" off the ionosphere and travel literally around the globe. Because the ionosphere plays such an important role in radiowave communication, remote sensing of the atmosphere has remained a highly active area of research for more than 30 years [Davies1,2,3]. The primary process currently in use for measuring the ion density of the ionosphere is the *ionosonde*. Ionosondes are performed from both terrestrial sites as well as from satellites. There are two primary methods of measurement: (i) measurement of the time delay of a pulse and (ii) determination of the stationary phase. The direct measurement of pulse delay is done by starting a timing device (e.g. cathode ray oscilloscope time base or a digital clock) when the transmitter is triggered and noting the time of the leading edge of the echo pulse(s) [Davies3]. Uncertainties arise in identifying which feature on the pulse envelope to use as reference. Even with a relatively square emitted pulse, ionospheric dispersion tends to produce a triangular or trapezoidal shaped echo. In some cases increased accuracy is obtained by using Gaussian-shaped pulses [Devlin]. However, time accuracy is limited to 1 μs which corresponds to 0.3 km of virtual height. Because of this inherent accuracy limitation, the time delay method is impractical for short range radar systems.

The phase approach is based on the relationship between phase and time delay which is also the basis for the derivation of the stepped DSB technique presented in the next section. In this ionosonde method, a single frequency sinusoidal signal is transmitted into the atmosphere and the phase of the echo is compared to the phase of the sinusoid produced by the generator. From knowledge of the frequency and velocity of propagation, the distance to the reflection point can be estimated. Although this technique is impractical for target ranging in general radar applications for the very same reasons the AM CW radar failed, it provides another example of using phase measurements to obtain the range to a reflective target.

There are two currently existing short range radar systems which are somewhat similar to the DSBSC technique and are used for automotive radar [Boyer, Grimes]: the Diplex Doppler method and the Sinusoidal FM method. In the Diplex Doppler method, the transmitter is time-shared between two closely spaced frequencies. The phase difference between the two slightly displaced Dopplers at the receiver depends on the range to the target. However, since the range is extracted from the phase difference in the Doppler signal, no information is obtained without significant target velocity.

The Sinusoidal FM technique extracts the target range from the relative phase of the received signal which does not depend on target speed. Unfortunately, the Sinusoidal FM system is relatively complex to implement [Grimes]. The advantage of the DSBSC technique is that it is simple to implement, requiring minimal hardware and space, while providing accurate target distance estimates. An important additional advantage of the frequency-stepped DSBSC system over other techniques such as a stepped-carrier

technique that generates an impulse response and uses range-gating to separate the target from an interferer is its immunity to Doppler shift due to target motion. The relative Doppler immunity of the frequency-stepped DSBSC technique is due to the fact that the effective Doppler shift is at twice the modulation frequency which is much smaller than the microwave carrier.

3.2 Derivation of the Frequency-Stepped DSBSC Technique

The DSBSC distance measurement technique is based on the relationship between the phase response and time delay of a linear system. For a linear system, the time delay is the negative slope of the system phase response and is therefore, in general, a function of frequency.

$$t_d = - \frac{d\theta(\omega)}{d\omega} \tag{3.2.1}$$

In the time domain, the simplest realistic model for the impulse response of a propagation channel known to contain an interfering reflector and a highly reflective target is given by

$$h(t) = A_p\delta(t-t_{dp}) + A_i\delta(t-t_{di}) \tag{3.2.2}$$

where $\delta(t)$ is the Dirac Delta function, and t_{dp} and t_{di} are the round trip time delays to the primary target and interfering reflector respectively. The constants A_p and A_i represent the combination of path loss and reflection coefficient associated with each reflector. This model assumes that a transmitted microwave energy burst will return primarily as two temporally concentrated

pulses. Simulation results presented later show that the result of using this assumption is accurate for the plasma measurement application.

The frequency response associated with a channel whose impulse response is given by (3.2.2) is

$$H(f) = A_p e^{-j\omega t_{dp}} + A_i e^{-j\omega t_{di}} \tag{3.2.3}$$

where $\omega = 2\pi f$. Separating H(f) into its real and imaginary parts yields

$$H(f) = A_p\cos(\omega t_{dp}) + A_i\cos(\omega t_{di}) - j\left[A_p\sin(\omega t_{dp}) + A_i\sin(\omega t_{di})\right] \tag{3.2.4}$$

The phase of this frequency response function is

$$\theta(f) = \mathrm{Tan}^{-1}\left(\frac{-\left(A_p\sin(\omega t_{dp}) + A_i\sin(\omega t_{di})\right)}{A_p\cos(\omega t_{dp}) + A_i\cos(\omega t_{di})}\right) \tag{3.2.5a}$$

The phase response may be expressed in the alternate form

$$\theta(f) = -2\pi f t_{dp} + \tan^{-1}\left(\frac{A_i\sin(2\pi f(t_{dp} - t_{di}))}{A_p + A_i\cos(2\pi f(t_{dp} - t_{di}))}\right) \tag{3.2.5b}$$

The negative derivative of the phase response (3.2.5a) with respect to angular frequency ω is the channel time delay and is given by

$$t_d = \frac{\beta}{1 + \left(\frac{A_p\sin(\omega t_{dp}) + A_i\sin(\omega t_{di})}{A_p\cos(\omega t_{dp}) + A_i\cos(\omega t_{di})}\right)^2} \tag{3.2.6}$$

where

$$\beta = \frac{C + D}{\left[A_p \cos(\omega t_{dp}) + A_i \cos(\omega t_{di})\right]^2} \tag{3.2.7}$$

$$C = \left[A_p \cos(\omega t_{dp}) + A_i \cos(\omega t_{di})\right]\left[A_p t_{dp} \cos(\omega t_{dp}) + A_i t_{di} \cos(\omega t_{di})\right] \tag{3.2.8}$$

$$D = \left[A_p \sin(\omega t_{dp}) + A_i \sin(\omega t_{di})\right]\left[A_p t_{dp} \sin(\omega t_{dp}) + A_i t_{di} \sin(\omega t_{di})\right] \tag{3.2.9}$$

Using the definition

$$\alpha = \frac{A_p}{A_i} \tag{3.2.10}$$

which is the signal-to-interference ratio (SIR), and elementary trigonometric identities, the expression for the channel time delay (3.2.6) may be simplified to

$$t_d = \frac{\alpha^2 t_{dp} + t_{di} + \alpha(t_{dp} + t_{di})\cos(2\pi f(t_{dp} - t_{di}))}{1 + \alpha^2 + 2\alpha\cos(2\pi f(t_{dp} - t_{di}))} \tag{3.2.11}$$

This function is periodic in frequency with period

$$T_f = \frac{1}{t_{dp} - t_{di}} \tag{3.2.12}$$

Thus, one mechanism for determining the distance to the primary target is to estimate the period of the group delay measurement. Since the time delay to the interfering RCG coating t_{di} is known *a priori,* the period (3.2.12) of the measured group delay yields the delay time to the plasma turning point t_{dp}. Using an estimate of the average energy propagation velocity for the plasma enables t_{dp} to be converted into a distance measurement. It will be shown

through simulation that this method of extracting the turning point location may lead to accurate range estimates.

A previously reported method of extracting the turning point standoff distance using the frequency-stepped DSBSC approach [Hearn] is to average the phase measurements, or equivalently the time delay measurements. The average time delay may be derived analytically by integrating the time delay expression (3.2.6) over one period and dividing the result by the period. The expression for the time delay (3.2.6) has the form

$$f(x) = \frac{a+b\cos(x)}{c+d\cos(x)} \tag{3.2.13}$$

where the following substitutions have been made:

$$a = \alpha^2 t_{dp} + t_{di}, \quad b = \alpha(t_{dp} + t_{di}), \quad c = 1 + \alpha^2, \quad d = 2\alpha, \quad x = 2\pi f(t_{dp} - t_{di}).$$

Given the fact that $c^2 \geq d^2$ for all α, the integral of f(x) over one period is

$$\int_{-\pi}^{\pi} \frac{a+b\cos(x)}{c+d\cos(x)}\,dx = \left[\frac{bx}{d} + \frac{2\left(a - \frac{bc}{d}\right)}{\sqrt{c^2 - d^2}} \mathrm{Tan}^{-1}\left(\frac{\sqrt{c^2 - d^2}\,\tan\left(\frac{x}{2}\right)}{c + d} \right) \right]_{-\pi}^{\pi} \tag{3.2.14}$$

The proof of this antiderivative is presented in the appendix. Evaluation of (3.2.14) and dividing by the period 2π yields the average value f_{av} given by

$$f_{av} = \frac{1}{2\pi} \int_{-\pi}^{\pi} f(x)\,dx = \frac{b}{d} + \frac{a - \frac{bc}{d}}{\sqrt{c^2 - d^2}} \tag{3.2.15}$$

Now resubstituting the coefficients a, b, c, and d yields the average time delay t_{dav} given by

$$t_{dav} = \frac{t_{dp} + t_{di}}{2} + \frac{\alpha^2 t_{dp} + t_{di} - \frac{(t_{dp} + t_{di})(1 + \alpha^2)}{2}}{|\alpha^2 - 1|} \qquad (3.2.16)$$

This expression may now be simplified to yield the result

$$t_{dav} = \frac{1}{2}\left(t_{dp} + t_{di} + \frac{\alpha^2 - 1}{|\alpha^2 - 1|}(t_{dp} - t_{di})\right) \qquad (3.2.17)$$

which may be further simplified to obtain the following final result

$$t_{dav} = t_{dp} \quad \alpha > 1, \quad t_{dav} = t_{di} \quad \alpha < 1 \qquad (3.2.18a)$$

The result for the special case of α=1 may be obtained by substituting this value directly into (3.2.11). After simplification, the average time delay for this case is

$$t_{dav} = \frac{t_{dp} + t_{di}}{2} \qquad (3.2.18b)$$

The analytical results derived here for the time delay obtained using the DSBSC technique may be interpreted as follows. If the plasma reflection is stronger than the reflection from the interfering RCG ($\alpha > 1$), and if an accurate technique for extracting the average phase is employed, then the turning point may be established. If the SIR is less than one ($\alpha < 1$), and phase averaging is employed, an erroneous estimate of the turning point will result. It has been analytically shown, however, that an accurate estimation of the turning point may be extracted from the phase measurements using the relation between the

group delay period (3.2.12) and the time delay difference t_{dp} - t_{di}, regardless of the signal-to-interference ratio. This result shows the potential immunity of the DSBSC technique to a weak primary target reflection.

The theoretical phase measurement, assuming two scatterers, has been shown to be

$$\theta(f) = \mathrm{Tan}^{-1}\left(\frac{-(A_p\sin(\omega t_{dp}) + A_i\sin(\omega t_{di}))}{A_p\cos(\omega t_{dp}) + A_i\cos(\omega t_{di})}\right) \qquad (3.2.5a)$$

Plots of the theoretical phase (3.2.5a) over a 4 GHz bandwidth, beginning at 18 GHz, for various SIR's are shown in figures 3.2.1a-d for the two scatterer idealization of the propagation path of figure 1.2.2 with the plasma critical density at 9 cm for 20 GHz (an average group velocity of c/2 has been assumed for the plasma).

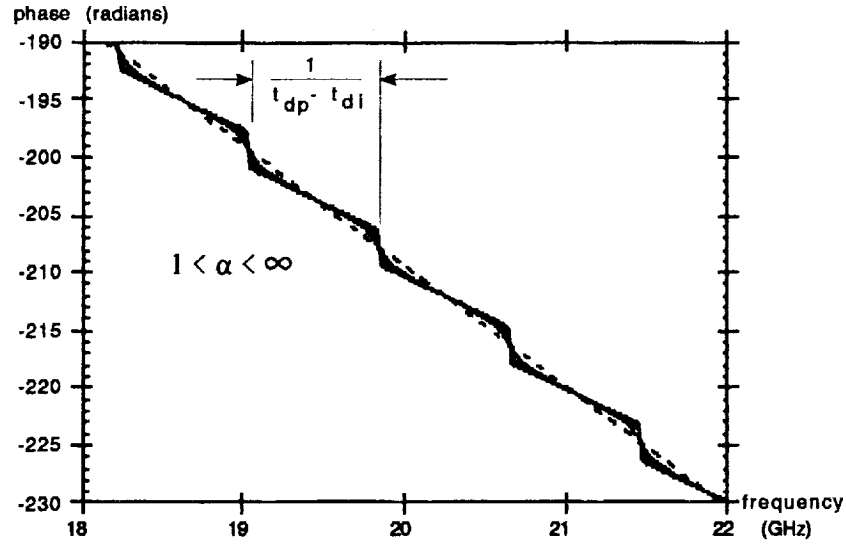

(a)

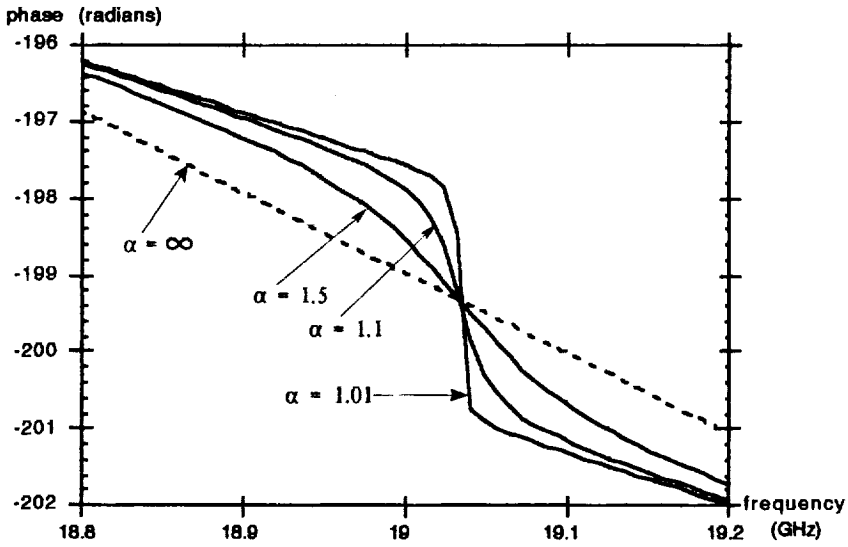

(b)

Figure 3.2.1 Theoretical frequency-stepped DSBSC phase measurement assuming two scatterers and SIR > 1. (a) 4 GHz bandwidth (b) 600 MHz bandwidth.

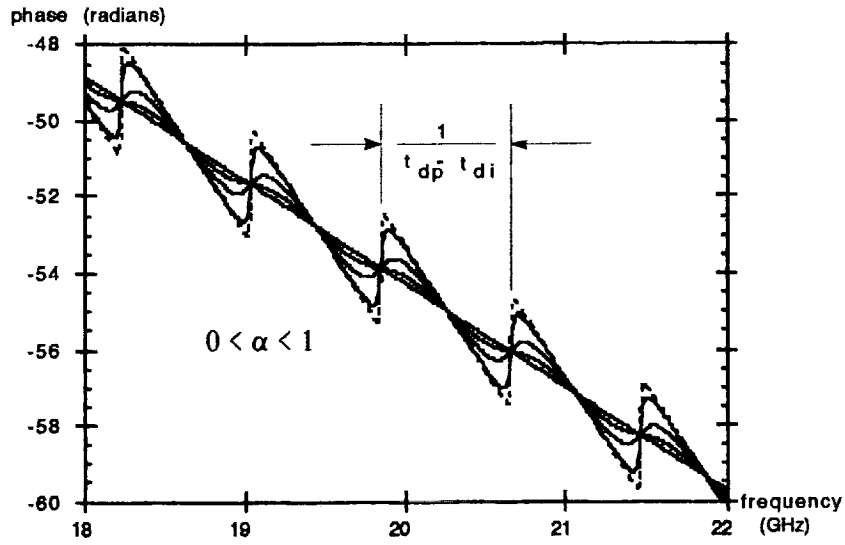

(c)

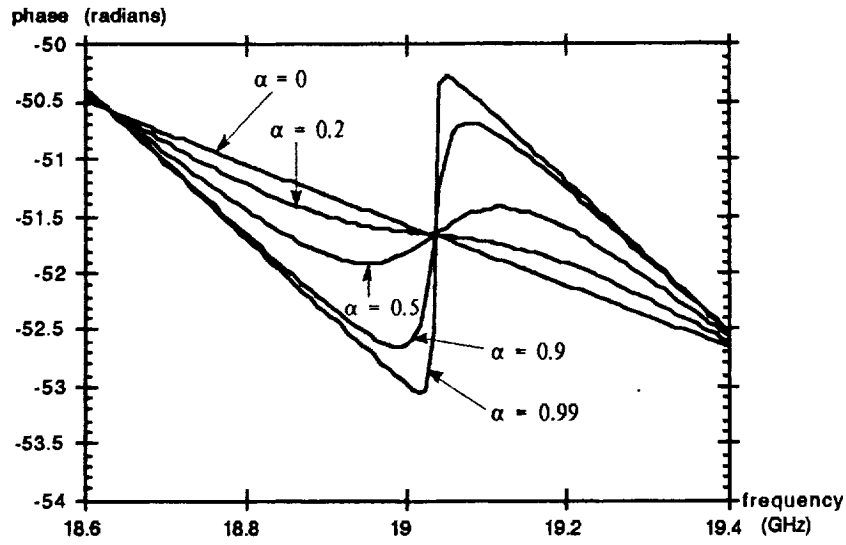

(d)

Figure 3.2.1 Theoretical frequency-stepped DSBSC phase measurement assuming two scatterers and SIR < 1. (c) 4 GHz bandwidth (d) 800 MHz bandwidth.

Several important observations can be made from these graphs. First of all, figures 3.2.1a-b show that if the interferer is absent, the SIR $\alpha=\infty$, and the phase is linear due purely to the primary target reflection. As the SIR deteriorates approaching unity from above, an oscillation about this linear phase occurs with increasing amplitude and may be seen most clearly in figure 3.2.1b which is an enlarged view of figure 3.2.1a. However, the periodicity of this oscillation does not change with SIR except in the extreme case $\alpha=\infty$. Figures 3.2.1c-d illustrate a similar phenomenon for cases of SIR's between 0 and 1. When $\alpha=0$, the phase becomes linear once again, and this is due purely to the interfering RCG. Note that the periodicity of the oscillations, once again, does not vary with SIR. When the SIR is identically equal to 1, the phase function will converge to a linear phase with an intermediate slope exactly half way between the extreme cases of $\alpha=0$ and $\alpha=1$, exactly as predicted by the theory developed earlier. It has been shown analytically that the periodicity of the oscillation about the linear case has a period which is the inverse of the difference in time delays to each scatterer. This relation is indicated in figures 3.2.1a and 3.2.1c, and special note should be made that this period is constant, independent of SIR.

The time delay may be calculated from the phase response by differentiating with respect to ω and then may be converted into a distance measurement as a function of frequency using an average plasma velocity. Using an average plasma velocity of c/2, several theoretical distance measurements using the same 4 GHz bandwidth as was used in figure 3.2.1 are shown in figure 3.2.2 for various SIR's.

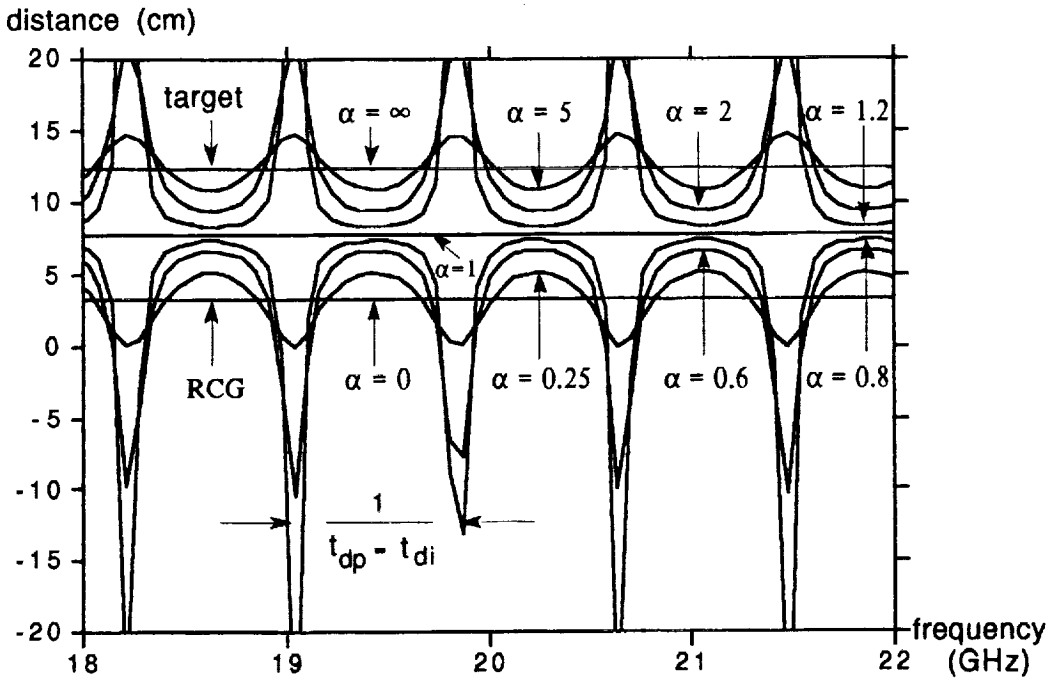

Figure 3.2.2 Theoretical distance measurements as a function of frequency for the frequency-stepped DSBSC system.

It has been proven that if the SIR is greater than one, then the average value of the distance function for any SIR is the primary target distance. Furthermore, it has been proven that if the SIR is less than one, then the distance function has an average value equal to the distance to the interfering RCG. Averages were taken for each of the distance functions shown in figure (3.2.2). When the SIR is such that the deviation from the mean value is small (α near ∞ or α near 0), then only a few points need to be averaged in order to obtain an accurate estimate of the average. However, when the SIR approaches unity from above

or below, many points are required for an accurate estimate of the average. This is due to the near cusps that develop at the function extrema. The periodicity is shown to contain the standoff distance information as expected from the theoretical derivation. An important point must be made regarding the process of averaging the distance measurements. Accurate estimates require that an integer number of half periods are averaged or that a large number of half periods be averaged. When the target and interferer are far apart, several periods are present. When the target is near the interferer, the period approaches zero which may cause an inaccurate distance measurement using the distance averaging approach especially if the SIR is near unity and only a relatively small number of measurements are averaged. In this case, it is fortunate that the distance information may still be extracted from the periodicity of the phase measurements, even when the oscillation is weak.

3.3 The Frequency-Stepped DSBSC Radar System Block Diagram and Principles of Operation

The Frequency-Stepped DSBSC system simultaneously transmits two sinusoids centered around the suppressed carrier. The differential phase shift between these two sidebands induced by the propagation channel is then measured at the receiver producing an incremental estimate of the slope of the phase response. This estimate of the phase response slope is the estimated group delay. A measurement is made at N discrete frequencies, spanning a total bandwidth of $N\Delta f$, where Δf is the frequency step size. An implementation of the DSBSC system is shown in figure 3.3.1.

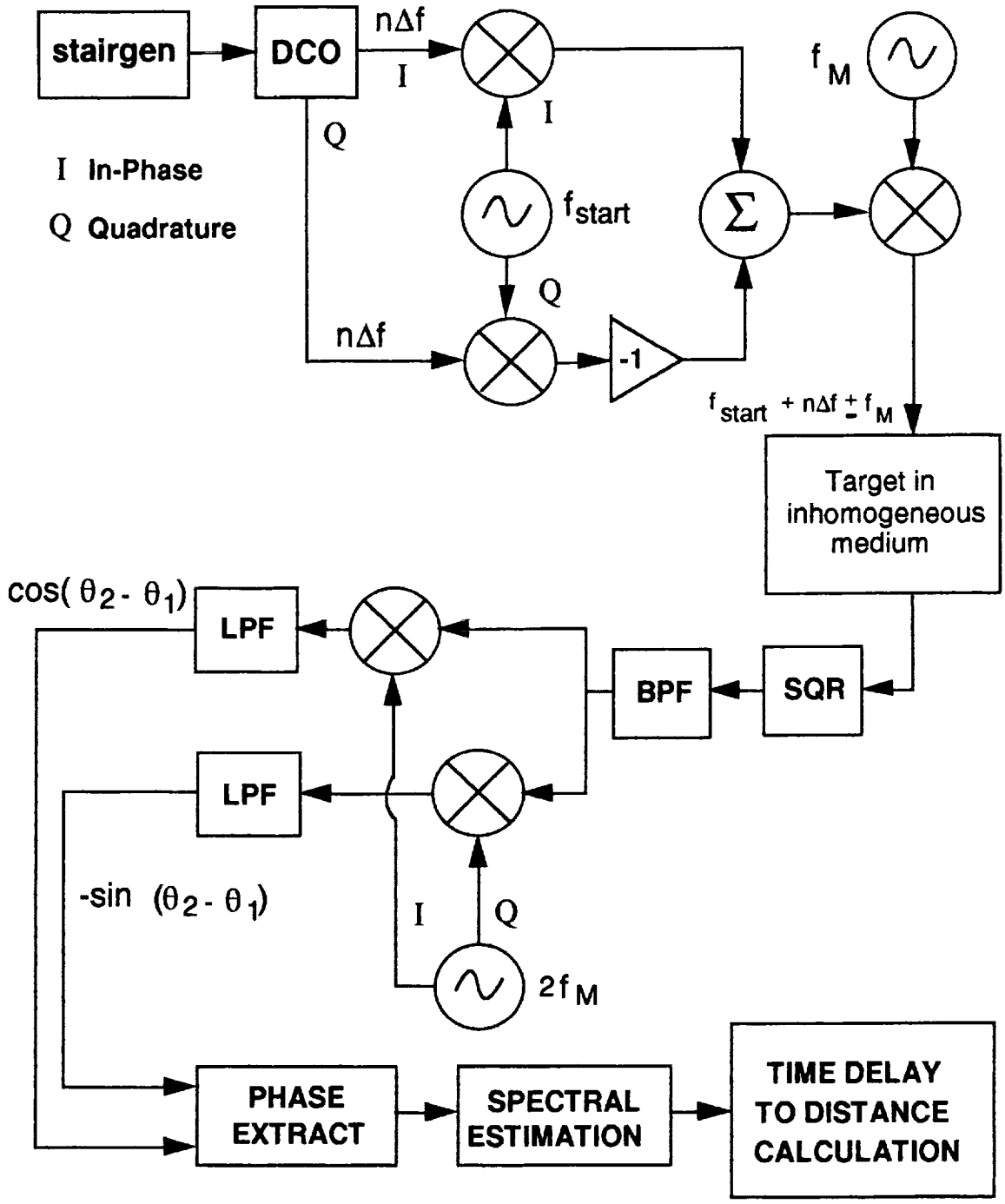

Figure 3.3.1 Block diagram of the frequency-stepped DSBSC radar system.

The transmitter consists of an upper single sideband frequency-stepped carrier generator whose output is modulated by another sinusoid of frequency f_M. The received echo is passed through a square-law device and bandpass filtered to extract the component at frequency $2f_M$ produced by the square-law device since it is this tone that contains the phase differential θ_2-θ_1 where θ_2 and θ_1 are the channel induced phase shifts of the upper and lower sidebands respectively. This signal is then simultaneously mixed with an in-phase and quadrature sinusoid at frequency $2f_M$, phase coherent with the modulator in the transmitter. After low-pass filtering, the result is a pair of quadrature signals from which the phase differential θ_2-θ_1 may be extracted via a four quadrant arctangent operation. The round-trip group delay estimate t_d is obtained from the phase difference by

$$t_d = -\frac{d\theta(\omega)}{d\omega} \approx -\frac{\theta_2-\theta_1}{\omega_2-\omega_1} = -\frac{\theta_2-\theta_1}{4\pi f_M} \tag{3.3.1}$$

The maximum unambiguous range corresponds to a 2π variation in θ_2-θ_1 and is given by

$$R_{max} = \frac{1}{2} v_g t_d = \frac{c}{8f_M} \tag{3.3.2}$$

using an average plasma velocity of c/2. Since it is desired to measure electron densities with standoff distances from 0-15 cm, we chose to use f_M = 125 MHz in our simulations which provides a maximum unambiguous range of approximately 30 cm from the antenna aperture. The range equation (3.3.2) dictates an upper bound on f_M. The smaller the value of f_M, the better the

differential phase approximates the true slope. However, as the value of f_M is reduced, the phase differential corresponding to a particular standoff distance decreases. Therefore it becomes increasingly difficult to resolve small standoff distances as f_M is decreased.

The block diagram of the DSBSC system presented in figure 3.3.1 shows the system exactly as implemented using CAPSIM, a hierarchical block diagram communication and signal processing simulation environment. The block *stairgen* creates a sequence of samples with a staircase amplitude which drives the digitally-controlled oscillator *DCO* to produce the discrete frequency sweep of N steps over a bandwidth of $N\Delta f$. The block in figure 3.3.1 labelled *Target in inhomogeneous medium* utilizes the inhomogeneous media model derived in Chapter 2.

It still remains to be shown whether the two scatterer theory developed in section 3.1 is applicable to the much more complex vacuum/tile/RCG/plasma propagation path which was shown in figure 1.2.2 (pg. 8). Simulation results will now be presented which show that the theory is indeed applicable.

3.4 Simulation Results for the Frequency-Stepped DSBSC System

In order to illustrate the performance of the frequency-stepped DSBSC system, consider the CFD electron density profile shown in figure 1.2.1 (pg. 5) scaled so that the critical density at 140 GHz is located at a standoff distance of 9 cm. Using N=64 measurements with a frequency step-size of Δf=64 MHz, the DSBSC system produced the distance measurements shown in figure 3.4.1.

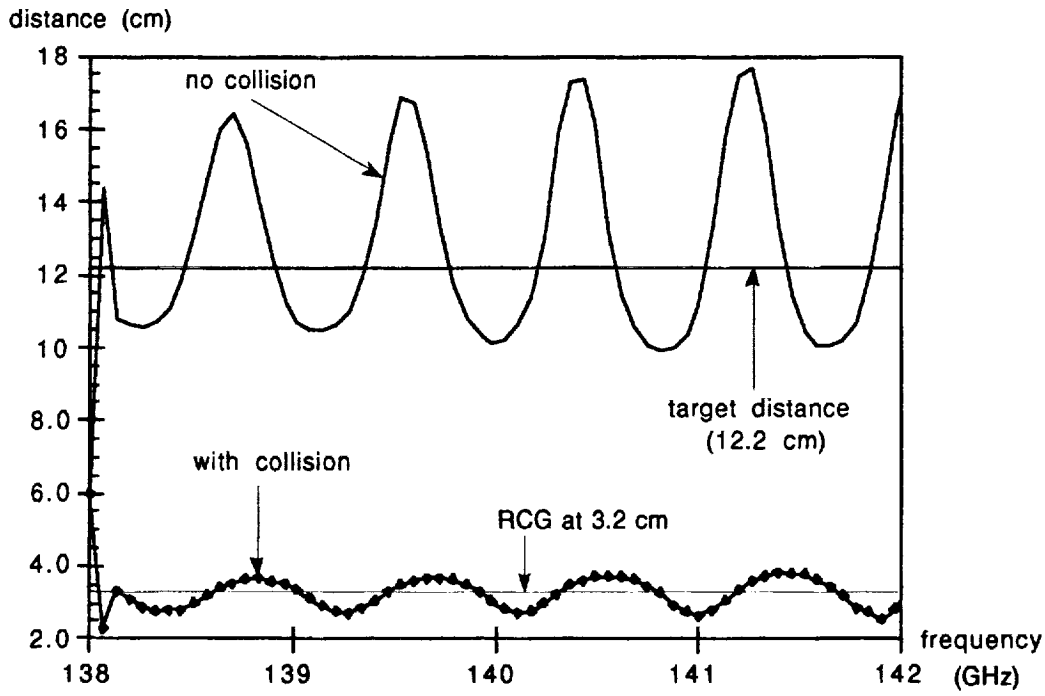

Figure 3.4.1 Distance measurements using the frequency-stepped DSBSC radar system with and without loss caused by plasma collisions.

When no loss due to collision is included, the group delay is captured by the primary target because the reflection from the plasma is stronger than the reflection from the RCG interferer. However, when loss is included in the simulation, the reflection from the RCG is much stronger than the plasma reflection and the group delay measurement is captured by the interfering RCG. The SIR in this case is approximately 0.1 (-20 dB). This SIR value was obtained by using a stepped CW technique and comparing the relative strengths of the plasma and interfering RCG reflections in the time domain. The averaging technique described in [Hearn] would work if no collision were present,

although producing an error of 0.5 cm (i.e. the average value of the no-collision curve is 12.70 cm). However, the averaging technique will fail in the more realistic case which includes path loss due to collision. Fortunately, the information containing the location of the plasma target is present in the data periodicity whether or not loss is present. It was shown in (3.2.12) that the fundamental frequency of the measurements shown in figure 3.4.1 is the difference in the time delays to the primary target and interferer assuming the simple two scatterer model. There exist several ways to extract the fundamental frequency from the N data points available from a given measurement sweep. The next section examines the use of autoregressive analysis on the group delay measurements to obtain the target range.

3.5 Autoregressive Signal Processing of the Frequency-Stepped DSBSC Data

One approach to extracting the fundamental frequency from the N data points available from a given measurement sweep would be to take an N-point Discrete Fourier Transform (DFT) of the data. The time resolution resulting from an N point DFT of the frequency-stepped DSBSC distance data is

$$\Delta t = \frac{1}{2N\Delta f} \tag{3.5.1}$$

Using an approximate average plasma group velocity of c/2, the one-way distance resolution is

$$\Delta d = \frac{1}{2}\frac{c}{2}\Delta t = \frac{c}{8N\Delta f} \tag{3.5.2}$$

Using N = 64 and Δf = 64 MHz, a distance resolution of Δd = 0.9155 cm results.

An alternative analysis technique is now presented for estimating the standoff distance from the periodicity of the distance measurements. It is based on autoregressive time series analysis [Kay81,88] which has been applied to high resolution spectral estimation. As will be shown, time series analysis may provide a significant resolution improvement in standoff distance estimates over that obtainable using the Fourier approach.

Consider the near periodic sequence of distance measurements shown in figure 3.4.1 to be approximated by the difference equation

$$d(n) = \sum_{k=1}^{3} a_k d(n-k) + u(n) \qquad n = m\Delta f \quad 0 \le m \le 63 \tag{3.5.3}$$

where d(n) is the sequence of distance measurements, a_k are the autoregressive coefficients, and u(n) is the innovation or input driving function. Thus, d(n) is being modeled as the response of a linear system whose output is the innovation plus a linear combination of the past 3 outputs. Such a model is called an autoregressive (AR) model of order 3. A third order autoregressive model was chosen because a single peak in the time response is expected which requires two complex poles in the model. The other parameter is used to model deviation in the phase measurements from a pure sinusoid. In conventional time series analysis d(n) would be, typically, discrete samples of a continuous-time function d(t). Here, the d(n) are discrete samples of a continuous-frequency function d(f). If the discrete-time Fourier Transform of (3.5.3) is taken, a continuous complex function of time results.

$$D(e^{j\Delta\omega t_{diff}}) = \sum_{k=1}^{3} a_k D(e^{j\Delta\omega t_{diff}})e^{-jk\Delta\omega t_{diff}} + U(e^{j\Delta\omega t_{diff}}) \qquad \Delta\omega = 2\pi\Delta f \tag{3.5.4}$$

where $t_{diff} = t_{dp} - t_{di}$. The system time response (output **D** over input **U**) may be obtained from (3.5.4) resulting in

$$R(t_{diff}) = \frac{1}{1 - \sum_{k=1}^{3} a_k e^{-jk\Delta\omega t_{diff}}} \tag{3.5.5}$$

which is once again a complex function of time. In order to illustrate the value of this approach, the time series model (3.5.3) was applied to the collision distance data of figure 3.4.1. The autoregressive coefficients a_k were extracted using a conventional least-squares approach [Kay81,88]. These coefficients were then substituted into (3.5.5) and the resulting squared magnitude is shown in figure 3.5.1. The delay estimate is 1.203 ns as shown in the figure and translates into a standoff estimate of 9.0225 cm, producing an error of only 225 μm. It should be noted that (3.5.5) is a continuous function of time and does not suffer from the resolution problem which plagues the FFT approach when only a short data record is available. It is recognized that the example presented is somewhat optimistic since neither noise nor the effects of some component error contributions were included in the simulation. The simulation does include non-ideal filter responses but does not incorporate the effects due to mixer imbalances. The plasma model accounts for reflections that occur at the vacuum-tile interface in addition to the reflections at the RCG boundaries.

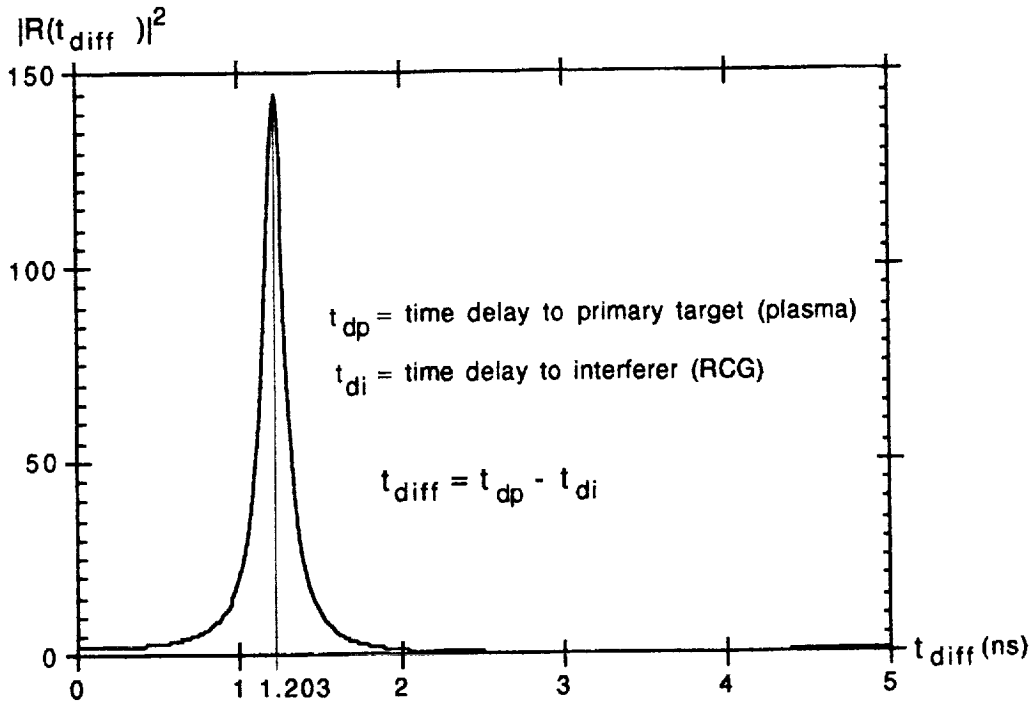

Figure 3.5.1 Spectrum obtained from an autoregressive time series analysis of the group delay measurements made by the frequency-stepped DSBSC radar system.

The intention of the example is to illuminate the fact that the technique of applying AR time series analysis to the frequency-stepped DSBSC measurements can be used to extract an accurate target distance estimate even when the SIR is significantly less than 0 dB. In our application of measuring electron plasma densities, a worst case Signal-to-Noise ratio (S/N) of 30 dB is expected at the inputs to the in-phase and quadrature detectors, and S/N ratios of 50-70 dB are expected for most measurements. Hence, it is not expected that noise levels will be large enough to significantly degrade performance in the

MRIS measurements. In other short-range radar problems, noise may be a significant problem and a more sophisticated spectral estimation approach such as an autoregressive moving average approach (ARMA) [Kay81,88] may be required.

It has been shown that autoregressive time series analysis can be used to measure accurately the period of the distance measurements made by the DSBSC system. The example presented shows that even when the SIR is significantly less than 0 dB, and the averaging technique fails as expected, the high resolution autoregressive estimator can provide an accurate distance estimate based on the simple two scatterer theory.

3.6 Summary

A new formulation of the frequency-stepped double sideband suppressed carrier radar system has been presented. With certain modifications, this chapter appeared in [Ybarra2]. The newly derived system is an extension of the amplitude modulated (AM) CW technique [Nilssen] that was introduced initially in 1947 in [Riden]. The AM CW technique was abandoned because severely erroneous target range estimates were obtained when an interfering reflection was present. The main contribution of this chapter is the inclusion of the effect of an interfering reflection in the derivation of the DSBSC system. It is shown that the interference can actually be used as a reference allowing accurate target range estimates to be extracted from the radar data, independent of signal to interference ratio.

Simulation results were then presented in the context of measuring electron plasma densities that develop near the heat tiles of a space re-entry vehicle. The inhomogeneous media model derived in Chapter 2 was used to model EM propagation in the heat tile as well as the continuously tapered CFD predicted profile. The results illustrate that the DSBSC radar system is capable of accurate target range estimation even when the echo from the target is much weaker than the echo from the interferer.

Chapter 4

The Frequency-Stepped Continuous Wave Radar System

One of the most prevalent techniques for characterizing a network is to measure its response to several, different frequency sinusoidal signals. A few broad-class examples of the many applications which utilize this technique are measurement of transmission line discontinuities [Dworsky], bandwidth measurements [HP], and s-parameter determination of two-port networks [Collin]. There are two main reasons for the widespread use of this approach. First, frequency response measurements are easy to perform. All that is required is a source which generates sinusoidal signals (an oscillator) and a detector which measures the amplitude and phase of the response. Second, the frequency response of a linear, time-invariant network uniquely characterizes the system [Glisson]. Knowledge of a system's frequency response allows the computation of its response to any stimulus. These two factors combined have led to the production and use of literally thousands of network analyzers [HP].

One of the primary objectives of a radar system is to determine the distance, or range, to one or several targets. Target range may be extracted from samples of the radar channel frequency response. This chapter presents an implementation of a radar system currently in use [Artech87] which employs a frequency-stepped CW approach to obtain measurements of the radar channel frequency response. There are two main objectives of this chapter. The first objective is to describe the mechanism by which frequency response samples are measured using the frequency-stepped CW approach. The

underlying principles of the stepped CW system are presented as the basis for the optimal signal processing algorithm derived and illustrated in Chapter 5. The second objective of this chapter is to illustrate the use of the inhomogeneous media model derived in Chapter 2 to simulate the measurement of non-uniform plasma densities using the frequency-stepped CW system.

4.1. Introduction to the Frequency-Stepped CW System

The physical data measured by the frequency-stepped CW radar system is a sequence of complex reflection coefficients as seen from the terminal plane to which the system is calibrated. The electric field reflection coefficient is defined by [Collin]

$$\Gamma = \frac{E_r}{E_i} \tag{4.1.1}$$

The reflection coefficient is, in general, a function of frequency and may be interpreted as samples of the channel frequency response $H(j\omega)$. Frequency response for electric circuits is defined in general to be the ratio of the phasor output (voltage or current) to the phasor input (voltage or current). The analogous definition for EM waves is the ratio of the phasor output (electric field or magnetic field) to the phasor input (electric field or magnetic field). In the case of the reflection coefficient as frequency response, the output phasor quantity is the reflected electric field intensity E_r and the input phasor quantity is the incident electric field E_i.

In the frequency-stepped CW system, a sinusoidal microwave or millimeterwave source (e.g. Gunn diode [Collins]) is used to generate the starting frequency f_{start} of the measurement sequence. This carrier frequency is then mixed with another, lower frequency sinusoidal signal whose frequency is stepped in equally spaced increments Δf. The frequency mixing performed in the transmitter is done in such a way as to produce an upper single sideband, frequency-stepped carrier whose frequency sequence is $f_{start} + i\Delta f$ $(i = 1\text{-}n)$. The radar system is calibrated at a convenient terminal plane so that no reflection is measured at any measurement frequency when the system is terminated in a matched load. When a physical radar measurement is made, an interference pattern in the fields is created at the terminal plane to which the system is calibrated. This interference pattern is the resulting sum of the transmitted and reflected waves and is physically observed as the reflection coefficient at the terminal plane. The reflection coefficient is measured at each of the n discrete frequencies. Once the sweep is complete, a set of n measurements of the reflection coefficient, or frequency response, has been extracted. The remainder of this chapter examines this frequency response extraction process for a particular CW system implementation, and its performance is illustrated through simulations which employ the inhomogeneous media model derived in Chapter 2. The simulations utilize the standard IFFT approach to transforming the frequency domain data to the time domain, from which the target range is estimated. It is shown that the IFFT produces target range estimates which may contain a high degree of uncertainty. This range uncertainty produced by the standard IFFT approach is part of the motivation for the development of the new optimal signal processing

approach presented in Chapter 5. The main motivation for using the optimization approach is the poor resolution achievable using the IFFT. This is clearly demonstrated in Chapter 5 where experimental measurements made using a physical frequency-stepped CW radar system are analyzed using both the standard IFFT approach and the new optimal signal processing algorithm.

4.2. The Frequency-Stepped CW Radar System Block Diagram and Principles of Operation

The block diagram of the frequency-stepped CW system is shown in Figure 4.2.1, and is the configuration, except for the channel model, proposed by Electromagnetic Sciences [EMS]. The system operates as follows. *Stairgen* generates a staircase signal which drives the digitally controlled oscillator *dco* producing both an in-phase and quadrature sequence of sinusoids whose frequency is stepped from Δf to $2\Delta f$ to $3\Delta f$, ..., through $n\Delta f$. This frequency-stepped signal then modulates the in-phase and quadrature carrier. The mixed quadrature components are multiplied by -1 and summed with the mixed in-phase components producing an upper single sideband stepped carrier signal which is launched into the channel. The generation of the upper single sideband carrier is based on the trigonometric relation

$$\cos(2\pi f_c t)\cos(2\pi\Delta f_m t) - \sin(2\pi f_c t)\sin(2\pi\Delta f_m t) = \cos[2\pi(f_c + \Delta f_m)t] \quad (4.2.1)$$

The received signal is then beat against the carrier and filtered to retrieve the baseband frequency-stepped signal.

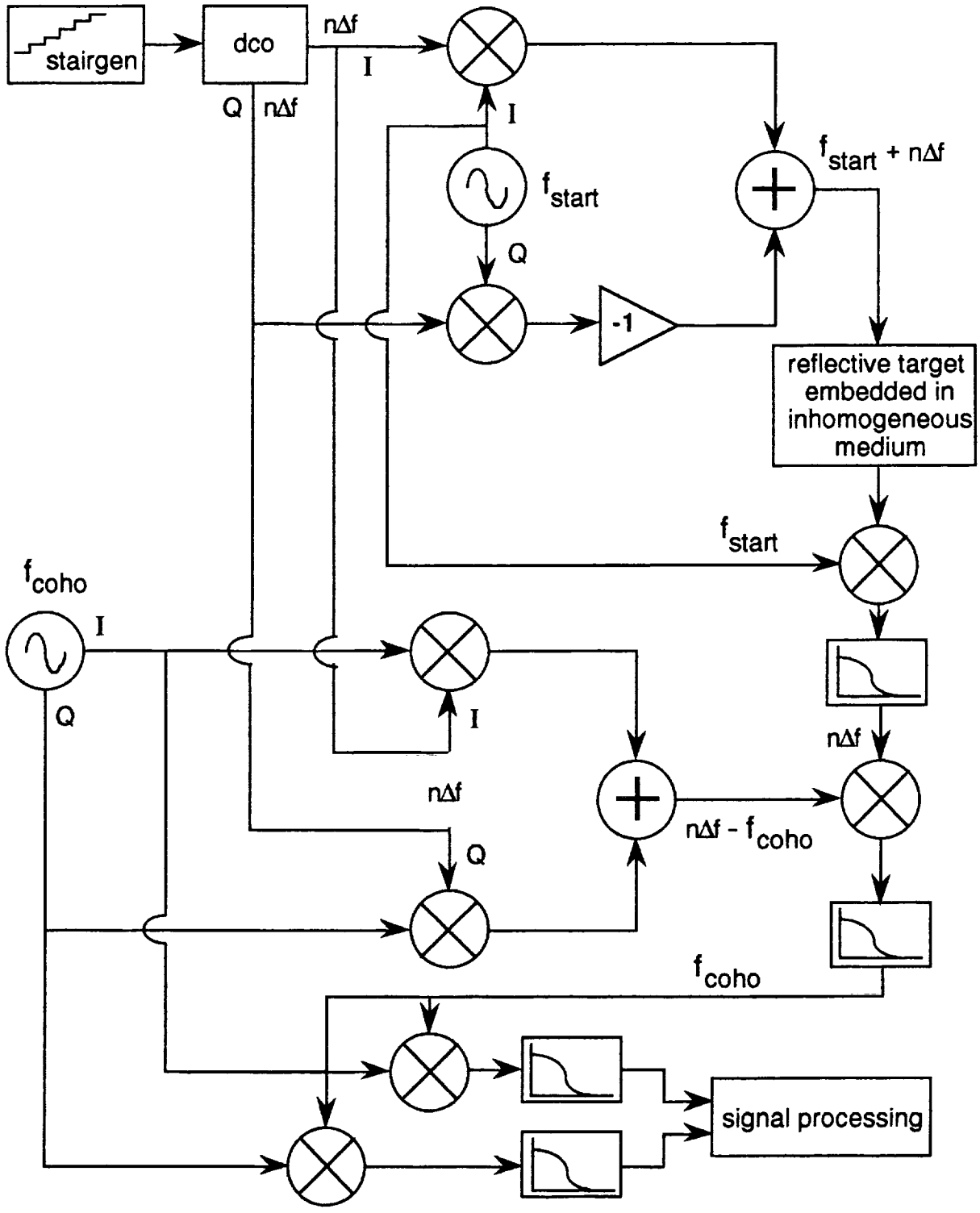

Figure 4.2.1 Block Diagram of the frequency-stepped CW radar system.

The coherent detector, which includes a lower single sideband generator, is then used to extract the in-phase and quadrature components of the frequency response data. Thus, the frequency-stepped CW system launches a sequence of n distinct unmodulated carriers into the channel, and the resulting induced gain and phase shift of the echo is measured by the receiver at each of the n frequencies. The system actually measures the in-phase and quadrature components of the echo which provide equivalent information.

The amount of time spent on a single frequency step is called the step *dwell time* and its inverse is called the *Step Repetition Frequency* (SRF). The dwell time must be long enough so that the transients in the receiver filters have decayed sufficiently for steady-state measurement, and short enough so that the target does not move significantly during the n measurements.

At the end of the n measurements, a set of n pairs of discrete frequency response data has been acquired. If the frequency change between steps is Δf, then the total bandwidth over which the measurement is made is $n\Delta f$. Using the standard approach, this finite bandwidth frequency response data is then converted into the time domain via an inverse Discrete Fast Fourier Transform (IFFT) to obtain an estimate of the channel impulse response. Through knowledge of the media dimensions and dielectric values through which the energy must propagate, the time domain impulse response may be converted into a *distance* domain impulse response. This distance domain impulse response usually possesses a peak value at the location of target. It will be shown in Chapter 5, however, that the IFFT is unreliable when the bandwidth is small and/or the target must be distinguished from an interfering reflection at approximately the same range as the target.

The next section presents the results of a computer simulation of the frequency-stepped CW system measuring the range to a specific electron plasma density using the cascaded slab model for the CFD plasma density profile.

4.3 Simulation Results for the Frequency-Stepped CW System

This section presents the results for a single simulation of the frequency-stepped CW system. It is intended to illustrate the use of the cascaded slab model for inhomogeneous media derived in Chapter 2, as well as some of the basic principles of using the IFFT to process the frequency domain data. The particular simulation presented employs the same channel and measurement bandwidth as was used to demonstrate the performance of the frequency-stepped DSBSC system derived in Chapter 3. Thus, a direct performance comparison of the two radar systems is possible by comparing the two target range measurements. Further results are presented for the stepped CW system in Chapter 5.

Consider the CFD profile of figure 1.2.1 scaled so that the critical electron density for 140 GHz is located at a standoff distance of 9 cm. In addition, let this plasma profile exist in the MRIS propagation path illustrated in figure 1.2.3. The time domain impulse response obtained using the IFFT on 64 measurements made by the frequency-stepped CW system over a bandwidth of 4 GHz, centered at 140 GHz is shown in figure 4.3.1. In this figure, there are actually two data sets plotted. The bar graph is the result of a 64 point IFFT of the 64 complex frequency domain samples using a rectangular window. The continuous plot is the result of a 16, 384 point IFFT of the 64 frequency samples

padded with 32,704 zeroes (total IFFT length is 32,768 points). The zero-padding serves to interpolate between the time samples of the 64 point IFFT [Kay88] as illustrated in the figure. Using the dimensions of the vacuum, heat tile, and RCG coating, as well as their permittivities, the two-way travel time to the outside surface of the RCG coating is calculated to be 0.25 ns. Using c/2 as an approximation for the average group velocity in the plasma, a 9 cm standoff distance corresponds to a two-way travel time of 1.203 ns. Hence, the time delay for the reflection from the plasma turning point is 1.453 ns. Examining the IFFT impulse response of figure 4.3.1 for this reflection it is evident that the exact reflection point is uncertain. The pulse resulting from the plasma has a peak value at a time delay of 1.38 ns. Using this value as the time delay to the turning point, its range is calculated to be 8.475 cm standoff. The corresponding range error is only 5.25 mm. However, it is not clear that the peak in the impulse response should be at the turning point time delay because the pulse is not distinct. It is smeared in time due to the finite, 4 GHz bandwidth measurement window. The time domain impulse response is the result of the convolution of an impulse due to the reflection and a sinc* pulse due to the rectangular window. The sinc pulse is the IFFT of the rectangular window whose width is the measurement bandwidth of 4 GHz [Kay88] and is given analytically by

$$F_w(j\omega) = K\frac{\sin(2\pi\cdot 10^9 t)}{2\pi\cdot 10^9 t} = K\,\mathrm{sinc}(2\pi\cdot 10^9 t) \qquad (4.3.1)$$

where K is a constant. The time width of the main lobe of this sinc function is

* sinc(x) is the sine-cardinal function and is defined here to be $\mathrm{sinc}(x) = \frac{\sin x}{x}$.

$$\Delta t_{lobe} = \frac{2}{2\pi \cdot 10^9} = 0.318 \text{ ns} \tag{4.3.2}$$

This sinc pulse is convolved with every impulse due to each reflection. If the simplifying assumption is made that there are only two reflections, one from the RCG and the other from the plasma, then the impulse response should consist of the sum of two sinc functions each with a main lobe width of 0.318 ns. These sinc pulses should be centered at 0.25 ns (RCG) and 1.453 ns (plasma). The sinc pulses are clearly present in the impulse response of figure 4.3.1. However, these sinc pulses interact. That is, the energy from the sidelobes of one sinc function interferes with the other sinc function. Consequently, the peak values of the two sinc pulses are biased away from their values that would be obtained with no interference present. This is the analytical explanation for the resolution and accuracy deterioration in the ability of the IFFT to extract target range as the bandwidth of the measurement is decreased. As the bandwidth of the measurement is decreased, the sinc functions spread out in time inversely proportional to the bandwidth. As the energy of the sinc pulses spread out in time, the pulses interfere with one another, causing the locations of the peaks to change. Furthermore, if the bandwidth is reduced to a small enough value, the two sinc pulses will merge into a single pulse and the distinction between two targets is lost. This phenomenon is carefully examined in the next chapter.

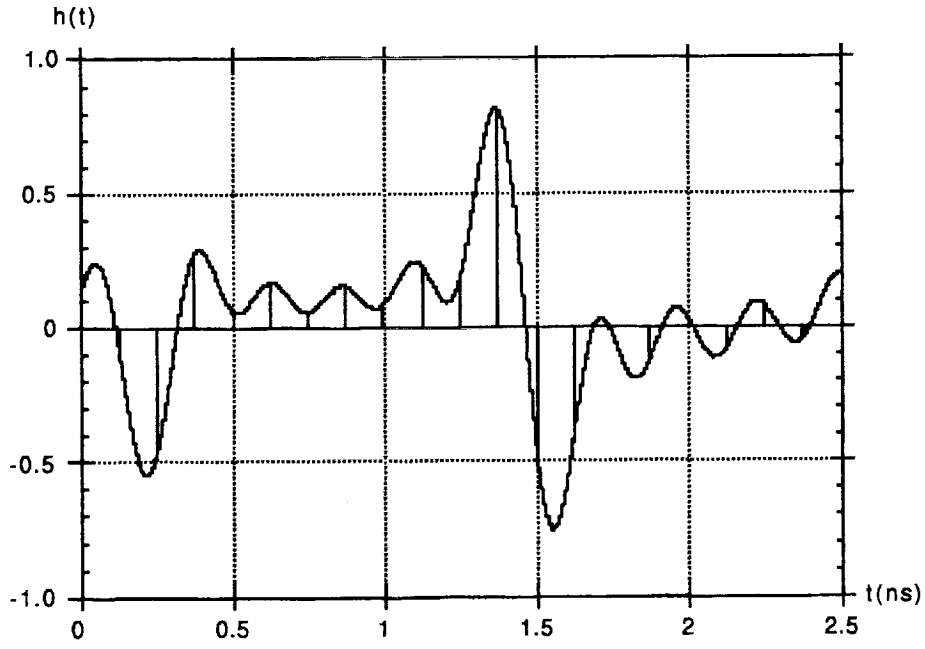

Figure 4.3.1 Impulse response obtained from 64 measurements of the MRIS plasma channel frequency response generated by the frequency-stepped CW radar system. The 64 point IFFT is shown along with a zero-padded 16,384 point IFFT.

4.1. Summary

This chapter has presented an implementation of a radar system currently in use [Artech87] which employs a frequency-stepped CW approach to obtain measurements of the radar channel frequency response. The implementation is a generalized system for producing CW measurements such as those measured by an HP 8510 network analyzer. The exact mechanism by which frequency response samples are measured using the frequency-stepped CW approach was described. The underlying principles of the stepped CW

system were presented as the basis for the optimal signal processing algorithm derived and illustrated in Chapter 5. Use is made of the inhomogeneous media model derived in Chapter 2 to simulate the measurement of non-uniform plasma densities using the frequency-stepped CW system. Target range uncertainty, inherent in IFFT processing due to the finite bandwidth of the measurement sweep, was clearly demonstrated in the results of the simulation.

Chapter 5

Globally Optimal Signal Processing of the Frequency-Stepped CW Data

The physical data measured by the stepped CW radar system is a sequence of complex reflection coefficients as seen from the aperture plane to which the system is calibrated. As was shown in Chapter 4, this sequence of measured reflection coefficients may be interpreted as samples of the channel frequency response $H(j\omega)$. Given these measurements the objective is to determine the target range. The standard approach [HP] is to perform an IFFT which produces an estimate of the channel time domain impulse response. Peaks in the impulse response correspond to reflections and their time delay corresponds to the range to the reflection. The resolution of this approach is limited by the measurement bandwidth. Since the measurement bandwidth must be kept relatively narrow when the target is embedded in a frequency dependent inhomogeneous medium to avoid significant dispersion, the resolution offered by the IFFT approach may be unsatisfactory.

In this chapter a new optimal signal processing algorithm is derived which maximizes the range resolution obtainable from any set of frequency-stepped CW measurements. The resolution limitations of the IFFT approach are demonstrated along with the enhancement offered by the new optimal processing algorithm using physical measurements made with an HP 8510 network analyzer. Two different sets of measured data are analyzed. The first set is a sequence of reflection coefficients measured at the input port of the 7mm Beatty Standard [Beatty]. The second set is a sequence of reflection

coefficients measured at the input port of a test apparatus for the MRIS instrument described in Chapter 1. In order to illustrate the resolution enhancement achievable by optimal processing over the IFFT, the measurement bandwidth is reduced to the point that the IFFT approach clearly fails to resolve two distinct reflections that are known to exist. The optimal processing algorithm is then applied to the reduced bandwidth data and the results reveal the potential resolution achievable.

5.1 The General Least Squares Optimization Problem

Given a set of frequency response measurements generated by the frequency-stepped CW radar system, the objective is to determine the target range. This may be accomplished by assuming an underlying physical model for the channel, computing the frequency response of the model at the frequencies at which the measurements were taken, and finally minimizing the norm of the difference between the physical measurements and the values produced by the model. The analytical expression for the objective function to be minimized, denoted by J, is given by

$$J = \|H(j(\omega_0+i\Delta\omega)) - H_m(j(\omega_0+i\Delta\omega))\| \qquad (5.1.1)$$

where the $H_m(j(\omega_0+i\Delta\omega))$ are the measured complex reflection coefficient pairs, the $H(j(\omega_0+i\Delta\omega))$ are the values of a theoretical model, $\|\cdot\|$ denotes vector norm [Golub], and *i* is the index number of each measurement and spans the integer

range from 1-n. J is a function of the parameters of the physical model yet to be specified.

The physical propagation path which will be assumed contains a reflective target embedded in an inhomogeneous medium. The inhomogeneity may be either continuously tapered, as in the case of the non-uniform CFD plasma profile, or composed of distinct media layers each having a different permittivity, as in the case of the thermal protection heat tiles of the AFE spacecraft, or any combination of the two. The simplest realistic model for the system impulse response has the form

$$h(t) = A_1\delta(t-t_1) + A_2\delta(t-t_2) + A_3\delta(t-t_3) + \ldots \qquad (5.1.2)$$

where the A_i are the reflection amplitudes and the t_i are the time delays to the reflections. The corresponding frequency response of the system is obtained by taking the Fourier Transform of (5.1.2) which produces

$$H(j\omega) = A_1e^{-j\omega t_1} + A_2e^{-j\omega t_2} + A_3e^{-j\omega t_3} + \ldots \qquad (5.1.3)$$

Samples of this frequency frequency response form the model values comprising $H(j(\omega_0+i\Delta\omega))$ in (5.1.1).

$$H(j(\omega_0+i\Delta\omega)) = A_1e^{-j(\omega_0+i\Delta\omega)t_1} + A_2e^{-j(\omega_0+i\Delta\omega)t_2} + A_3e^{-j(\omega_0+i\Delta\omega)t_3} + \ldots \qquad (5.1.4)$$

Therefore, using the assumed model for the system impulse response (5.1.2), the objective function J (5.1.1) is a function of the reflection amplitudes and delays.

The type of vector norm implemented in (5.1.1) must be judisciously chosen. A proper choice of norm will incorporate all the measured data and

present a tractable mathematical problem for extracting the optimal values for the amplitudes and delays of the model. A reasonable choice is the 2-norm since the objective function J will be quadratic in the amplitude parameters and a standard least squares approach [Golub, Lawson] can be used to extract those parameters. Using the 2-norm as the metric in (5.1.1), the general least squares optimization problem becomes finding the set of amplitudes and delays in the model which minimize

$$J = \sum_{i=1}^{n} |H(j(\omega_0+i\Delta\omega)) - H_m(j(\omega_0+i\Delta\omega))|^2 \qquad (5.1.5)$$

The summation index *i* in (5.1.5) ranges over the *n* measured data pairs. In the next section a derivation is presented for determining the optimal reflection amplitudes and delays.

5.2 Derivation of the Optimal Reflection Amplitudes

The objective is to find the global minimum of the performance metric (5.1.5) with respect to the amplitude-delay pairs A_i, t_i in the model (5.1.2-3). This objective is achieved by decomposing the performance metric (5.1.5) into a sum of linear and non-linear components. The linear portion of the objective is a set of simultaneous linear equations whose solution yields the optimal amplitudes. The metric (5.1.5) is quadratic in the amplitude parameters A_i. This allows the A_i to be calculated in closed form by solving the least squares problem

$$\mathbf{Fa} \cong \mathbf{f} \qquad (5.2.1)$$

The complex (n x N) matrix **F** is composed of frequency response estimates based on the model (5.1.4) and is given by

$$\mathbf{F} = \begin{bmatrix} \cos(\omega_1 t_1) - j\sin(\omega_1 t_1) & \cos(\omega_1 t_2) - j\sin(\omega_1 t_2) & \cdots & \cos(\omega_1 t_N) - j\sin(\omega_1 t_N) \\ \cos(\omega_2 t_1) - j\sin(\omega_2 t_1) & \cos(\omega_2 t_2) - j\sin(\omega_2 t_2) & \cdots & \cos(\omega_2 t_N) - j\sin(\omega_2 t_N) \\ \vdots & \vdots & \ddots & \vdots \\ \cos(\omega_n t_1) - j\sin(\omega_n t_1) & \cos(\omega_n t_2) - j\sin(\omega_n t_2) & \cdots & \cos(\omega_n t_N) - j\sin(\omega_n t_N) \end{bmatrix} \tag{5.2.2}$$

where n is the number of frequency measurements and N is the number of A_i, t_i pairs to be extracted. The complex vector **f** is composed of the physical frequency response measurements and is given by

$$\mathbf{f} = [H_M(\omega_1)\ H_M(\omega_2)\ H_M(\omega_3)\ \cdots\ H_M(\omega_n)]^T \tag{5.2.3}$$

The vector **a** in (5.2.1) contains the set of amplitudes A_i to be determined

$$\mathbf{a} = [A_1\ A_2\ A_3\ \cdots\ A_N]^T \tag{5.2.4}$$

Solution of the least squares problem requires assuming a set of delays t_i. It is shown later that by "scanning" a sequence of amplitude optimized objective function values for certain delay combinations, it is possible to find the global minimum of (5.1.5). Finding the global, or absolute minimum of (5.1.5) determines the optimal set of reflection amplitude-delay pairs. If there exists any a priori knowledge about the target range such as upper and/or lower bounds, the range of the time delays over which the objective function is scanned can be limited and the amount of computation necessary to find the global minimum reduced.

The solution to (5.2.1) will yield a set of complex amplitudes because the model (5.1.2-4) will not fit the physical data exactly. However, in the derivation which follows, the amplitude vector **a** is constrained to be real. The same approach that is used to solve the standard real LS problem using the normal equation approach [Golub, Lawson] can be extended to solve this problem. The solution to (5.2.1) is found by minimizing the real scalar that results from the following squared inner product.

$$y = \| (\mathbf{F}_r + j\,\mathbf{F}_i)\mathbf{a} - (\mathbf{f}_r + j\,\mathbf{f}_i) \|_2^2 \tag{5.2.5}$$

$$y = (\mathbf{F}_r\mathbf{a} - \mathbf{f}_r)^T(\mathbf{F}_r\mathbf{a} - \mathbf{f}_r) + (\mathbf{F}_i\mathbf{a} - \mathbf{f}_i)^T(\mathbf{F}_i\mathbf{a} - \mathbf{f}_i) \tag{5.2.6}$$

$$y = \mathbf{a}^T[\mathbf{F}_r^T\mathbf{F}_r + \mathbf{F}_i^T\mathbf{F}_i]\mathbf{a} - \mathbf{a}^T[\mathbf{F}_r^T\mathbf{f}_r + \mathbf{F}_i^T\mathbf{f}_i] - [\mathbf{f}_r^T\mathbf{F}_r + \mathbf{f}_i^T\mathbf{F}_i]\mathbf{a} + \mathbf{f}_r^T\mathbf{f}_r + \mathbf{f}_i^T\mathbf{f}_i \tag{5.2.7}$$

In order to minimize *y*, the gradient of (5.2.7) is taken with respect to the amplitude vector **a** and set equal to the zero vector.

$$\frac{\partial y}{\partial \mathbf{a}} = 0 = 2[\mathbf{F}_r^T\mathbf{F}_r + \mathbf{F}_i^T\mathbf{F}_i]\mathbf{a} - 2[\mathbf{F}_r^T\mathbf{f}_r + \mathbf{F}_i^T\mathbf{f}_i] \tag{5.2.8}$$

The result of the minimization of (5.2.5) is a real, square set of linear equations which can be solved by using any linear equation solving technique.

$$[\mathbf{F}_r^T\mathbf{F}_r + \mathbf{F}_i^T\mathbf{F}_i]\mathbf{a} = \mathbf{F}_r^T\mathbf{f}_r + \mathbf{F}_i^T\mathbf{f}_i \tag{5.2.9}$$

However, in certain cases, the symmetric matrix premultiplying **a** is extremely ill-conditioned [Golub, Lawson]. In order to see when such cases arise let

$$\mathbf{H} = \mathbf{F}_r^T \mathbf{F}_r + \mathbf{F}_i^T \mathbf{F}_i \tag{5.2.10}$$

and examine the case of a two reflection problem for simplicity.

$$\mathbf{H}^{2x2} = \begin{bmatrix} \sum_{i=1}^{n} \cos^2(\omega_i t_2) + \sin^2(\omega_i t_2) = n & \sum_{i=1}^{n} \cos(\omega_i t_1)\cos(\omega_i t_2) + \sin(\omega_i t_1)\sin(\omega_i t_2) \\ \sum_{i=1}^{n} \cos(\omega_i t_1)\cos(\omega_i t_2) + \sin(\omega_i t_1)\sin(\omega_i t_2) & \sum_{i=1}^{n} \cos^2(\omega_i t_2) + \sin^2(\omega_i t_2) = n \end{bmatrix} \tag{5.2.11}$$

One obvious case that will cause **H** to be ill-conditioned occurs when the values of t_1 and t_2 are nearly equal. When the values of t_1 and t_2 are exactly equal, **H** becomes singular. In order to deal with this problem, the singular value decomposition technique [Golub, Press] is used to solve (5.2.9). When any singular value is found to be less than 0.01, its value is set equal to zero before the final computation of **a** is performed. This extracts the minimum norm solution to (5.2.9), which is precisely what is sought.

The original LS optimization problem (5.1.5) has been decomposed into a linear problem whose solution yields the amplitudes A_i, and a highly non-linear problem whose solution, it will be shown, yields the delays t_i. It is important to recognize that the solution of (5.2.9) for the amplitudes A_i requires that a set of delays t_i be utilized in forming the entries of the matrix **H**.

The following optimization procedure may be followed for extracting the A_i, t_i pairs:

1) Choose the number N of A_i, t_i pairs to be determined.
2) Assume a sequence of t_i values and solve (5.2.9) for the optimal A_i .
3) Search for the global minimum of (5.1.5) using the amplitudes found from the solution of (5.2.9).

It will be shown in Section 5.4 that the geometric interpretation of the LS objective function J, subject to the solution of (5.2.9), is a multiple minima surface with grooves aligned with the delay axes. The grooves in this surface can be searched sequentially and the global minimum found with little computation. The global minimum corresponds to the optimum reflection amplitudes and delays and hence to target range. The next section presents frequency-stepped CW measurements made using an HP 8510 network analyzer which will then be analyzed using the global optimization technique in section 5.4.

5.3 Experimental Measurements

This section presents frequency-stepped CW measurements made using an HP 8510 network analyzer in two different experimental set-ups. First, measurements of the reflections in an air-line coaxial cable section, the Beatty Standard, are presented. Then, measured data from an MRIS test apparatus including a simulated heat tile is examined. The process of extracting the reflection time delays using the standard IFFT approach, as used by the HP 8510 network analyzer internal computer, is illustrated for both sets of experimental data.

Consider the 7 mm Beatty Standard [Beatty, HP] of the HP-8510 network analyzer terminated in a matched load and its theoretical bounce diagram as shown in figure 5.3.1. The Beatty Standard presents two step-discontinuities in the characteristic impedance of the line. These discontinuities are produced by

an abrupt change in the outer diameter of the inner conductor. The bounce diagram shows the theoretical amplitude and delay of each reflection for measurement calibrated to the input port of the Beatty Standard. Measurements of the reflection coefficient s_{11} were taken over two different bandwidths using an HP8510 network analyzer.

The first set of measurements were taken over the band 45 MHz - 18 GHz using 801 evenly spaced frequencies. The resulting IFFT is shown in figure 5.3.2. A rectangular window [Harris] was utilized to maximize the resolution between the reflections. The 18 GHz bandwidth is large enough to clearly distinguish the reflections. In addition, the amplitude and delay of the first three reflections is very accurate. The second set of measurements were taken over the band 4 GHz - 6 GHz using 801 evenly spaced frequencies, and the resulting IFFT is shown in figure 5.3.3.

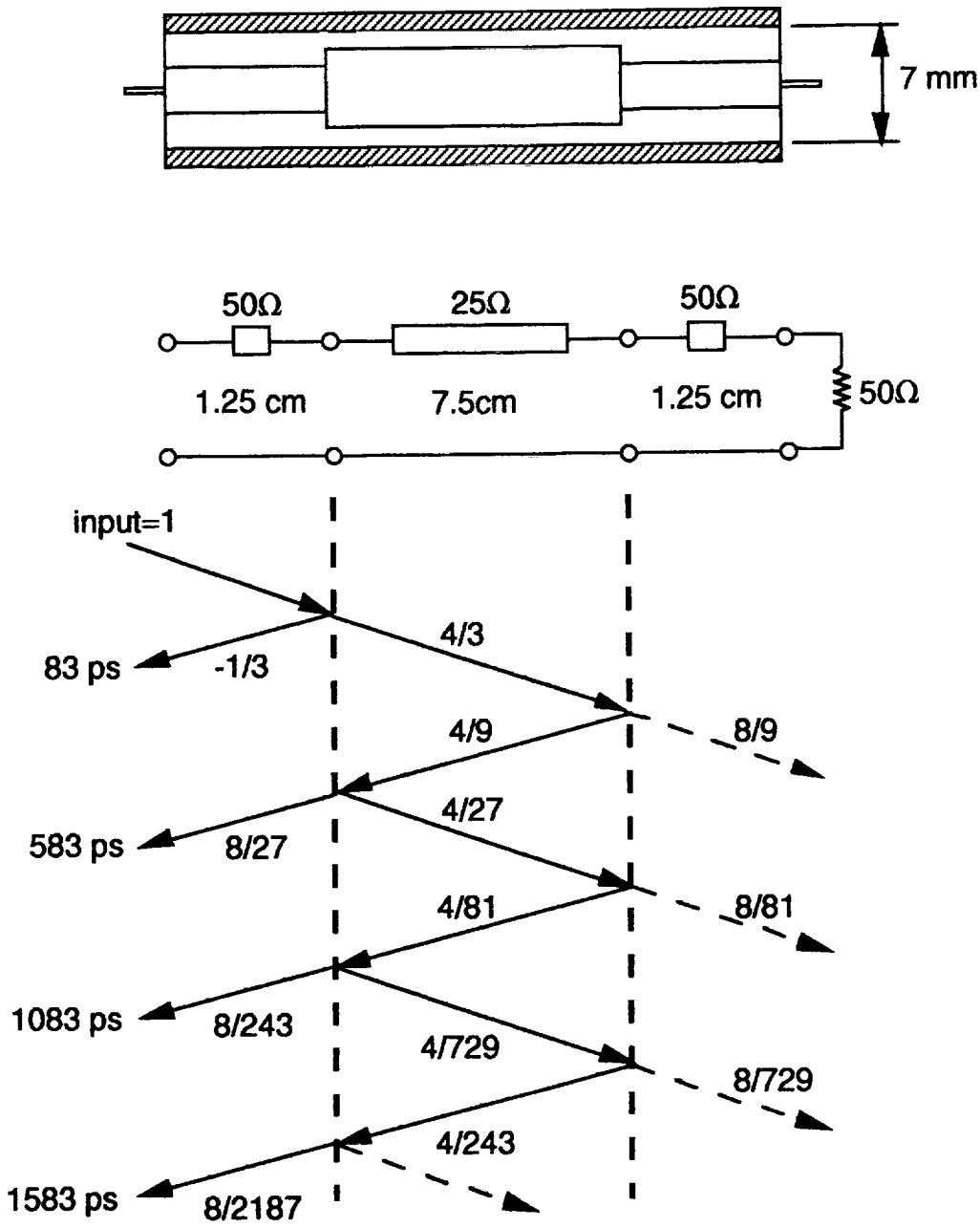

Figure 5.3.1 7 mm coaxial Beatty Standard terminated in a matched load and the resulting bounce diagram for a unit impulse stimulus.

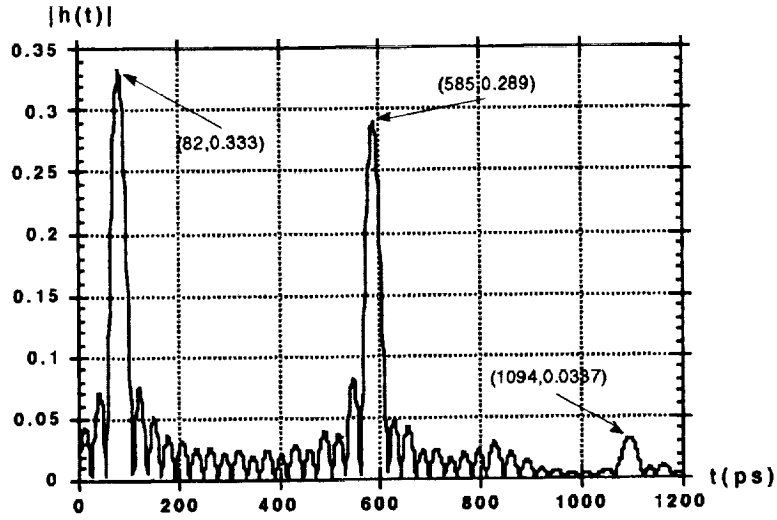

Figure 5.3.2 Inverse FFT of 801 measurements of the reflection coefficient at the input port of the 7 mm Beatty Standard shown in figure 5.3.1. The bandwidth used in this measurement is 18 GHz.

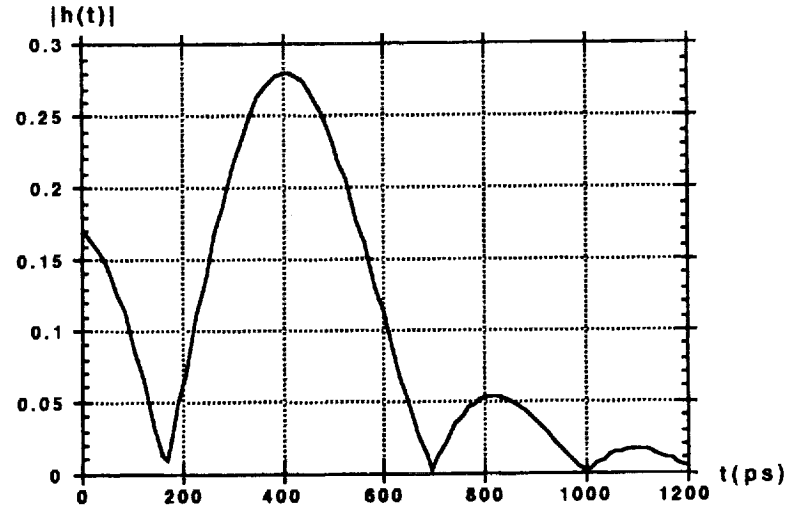

Figure 5.3.3 Inverse FFT of 801 measurements of the reflection coefficient at the input port of the 7 mm Beatty Standard shown in figure 5.3.1. The bandwidth used in this measurement is 2 GHz.

The 2 GHz bandwidth is so small that the two reflections (83 ps, 583 ps) have merged into a single pulse. In this case the IFFT cannot resolve the two reflections. In addition, the location of the peak in the impulse response is biased [Kay88] away from the correct location of either of the two reflections. Hence, when two reflections are so close in time that the IFFT cannot resolve them, accuracy is lost as well.

In order to test the applicability of the optimization approach to detecting the turning point range for the MRIS instrument, a test fixture was constructed at NASA LaRC. This fixture is shown in figure 5.3.4 along with its physical connection to the network analyzer via a rectangular to circular waveguide transition. The network analyzer is calibrated to the input port of the waveguide as shown in the diagram. The simulated heat tile is composed of a 0.25" thick layer of silicon dioxide, or quartz glass (ε_r = 3.78), and a 0.5" thick layer of polyurethane foam (ε_r = 1.4). A 0.5" thick aluminum plate is used for the aperture ground plane. The target is formed by the presence of another 0.5" thick aluminum plate parallel to the aperture plane of the circular horn antenna. Target range is set by moving mobile target.

In the first set of measurements, the target was set at a distance of 12" from the outer surface of the quartz glass. The two primary reflections will be due to the high dielectric constant quartz glass and the metal plate target. 801 measurements of the reflection coefficient were made from 14-18 GHz, spanning a total bandwidth of 4 GHz. The IFFT of the measured radar data is shown in figure 5.3.5. The first three reflections are clearly resolved. The time delay corresponding to the first reflection, due to the quartz glass interferer, is difficult to calculate accurately because the velocity of propagation throughout

the waveguide and antenna is not known. The velocity of energy propagation, or group velocity, within a waveguide is frequency dependent and is given by [Collin]

$$v_g = c\sqrt{1-\left(\frac{f_c}{f}\right)^2} \tag{5.3.1}$$

where c is the free space velocity of light, f_c is the cut-off frequency of the waveguide, and f is the frequency of propagation. The rectangular waveguide in figure 5.3.4 has the dimensions 1.58 cm by 7.9 mm. This geometry produces a cut-off frequency of 9.49 GHz [Collin]. In order to determine the average group velocity, v_g must be integrated over the measurement bandwidth.

$$v_{av} = \frac{c}{f_2 - f_1}\int_{f_1}^{f_2}\sqrt{1-\left(\frac{f_c}{f}\right)^2}\,df \tag{5.3.2}$$

The antiderivative is of standard form and from [CRC] is given by

$$\frac{c}{f_2 - f_1}\int\sqrt{1-\left(\frac{f_c}{f}\right)^2}\,df = \frac{c}{f_2 - f_1}\left[\sqrt{f^2 - f_c^2} - f_c\sec^{-1}\left(\frac{f}{f_c}\right)\right] \tag{5.3.3}$$

Using the frequency span of 14-18 GHz in (5.3.2) and a cut-off frequency of 9.49 GHz, the average velocity of propagation is found to be 0.801c within the rectangular waveguide. If the entire length of waveguide in figure 5.3.2 were rectangular, the two-way travel time to the center of the quartz glass would be 3.71 ns. The time delay to the first major reflection is approximately 3.45 ns as determined from the IFFT shown in figure 5.3.5. The time delay calculation

above, which assumes that the entire waveguide and antenna system is composed of a uniform rectangular waveguide, is intended only as an example of an approach which may be used to determine the average propagation delay through the waveguide system. The calculation of the average group velocity within the waveguide structure is actually more complicated due to the rectangular to circular transition as well as the flare in the circular horn antenna. The rectangular to circular waveguide transition is designed to suppress the creation of multiple modes. A gradual transition from rectangular to circular geometry allows the energy in the dominant mode (TE_{10}) of the rectangular guide to propagate as energy in the dominant mode (TE_{11}) of the circular guide [Collin]. However, the circular horn stimulates the creation of several TE and TM modes making the calculation of average group velocity more complicated than assuming single mode transmission. By carefully examining the geometry of the waveguide and circular horn antenna, the average propagation velocity may be calculated leading to a very accurate prediction of the time delay to the quartz glass.

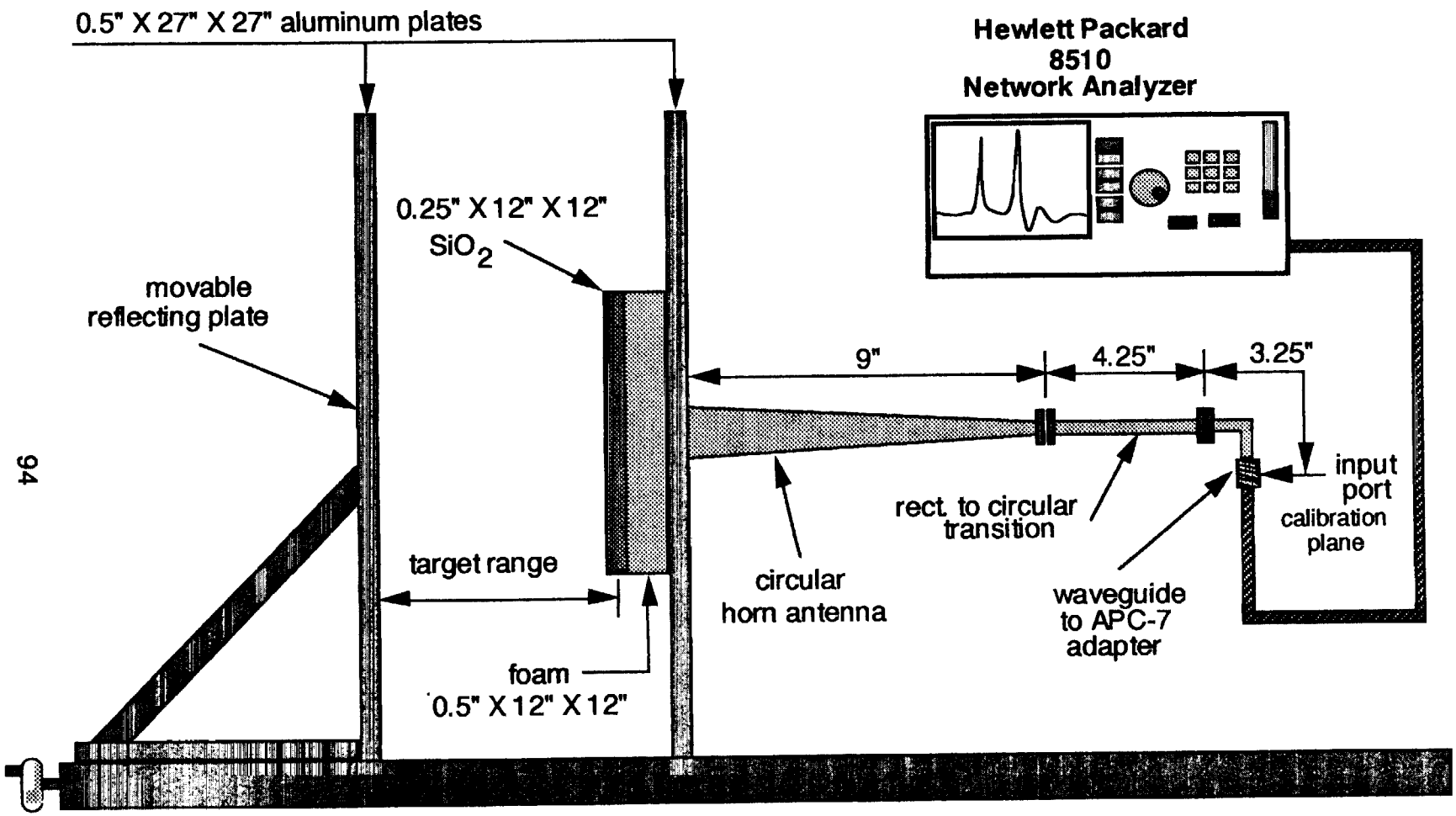

Figure 5.3.4 Microwave Reflectometer Ionization Sensor (MRIS) test apparatus.

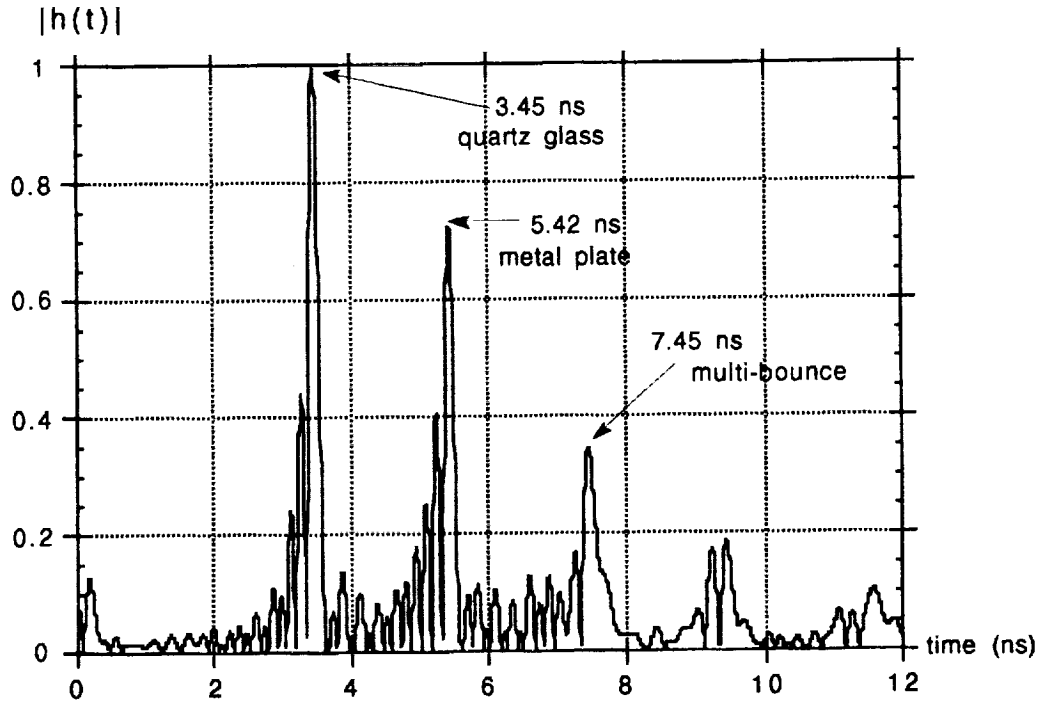

Figure 5.3.5 Normalized Inverse FFT of 801 measurements of the reflection coefficient at the input port of the MRIS test apparatus shown in figure 5.3.4. The bandwidth used in this measurement is 4 GHz, and the target range is 12".

However, the prediction of the time delay to the interfering reflection from the quartz glass is not the primary interest here. The primary concern is target range resolution and accuracy. Detecting accurately the time delay from the reflection due to the quartz glass to the metal plate target is the objective.

The IFFT shown in figure 5.3.5 indicates there is a delay of 1.97 ns from the quartz glass to the metal plate. Using the free space velocity of propagation for the two-way distance of 24" in air requires 2.032 ns. Since each reflection

from from the quartz glass is assumed to be a single impulse, two unresolved impulses resulting from the front and back surfaces, an additional delay of 41 ps is included to account for the 0.25" of travel through the glass. Thus, the target range is defined to be the distance from the center of the glass to the metal plate. The total theoretical two-way travel time is 2.073 ns. A time delay estimate of 1.97 ns is produced by the IFFT. Thus, the error in the time delay estimate produced by the IFFT using 4 GHz of bandwidth is 103 ps and corresponds to a range estimate error of approximately 0.608" (1.545 cm).

In the second set of measurements, the target was set at a distance of 2.25" from the outer surface of the quartz glass. 100 measurements of the reflection coefficient were made from 14-14.5 GHz, spanning a total bandwidth of only 500 MHz. The IFFT of the measured radar data is shown in figure 5.3.6. The narrow bandwidth spanned by the measurement sequence is so small that several reflections have merged into a single lobe of the IFFT. The 2.25" distance from the outer surface of the quartz glass to the metal plate target corresponds to 0.381 ns of two-way travel time. Including 41 ps of delay within the quartz glass results in a total theoretical two-way travel time of 0.422 ns. Since the metal plate target is so close to the tile, there are many reflections between the quartz glass and the aluminum plate. These reflections are separated by 0.422 ns in time. The main lobe in the IFFT spans approximately 2 ns, enough time to "swallow" nearly 3 of these multibounce reflections. The time delay corresponding to the second major peak in the IFFT of figure 5.3.6 is 4.8 ns and has no value in assessing the range to the target. This is the best performance the IFFT has to offer for determining the distance to the target

under the bandwidth constraint of 500 MHz with only 100 frequency measurements.

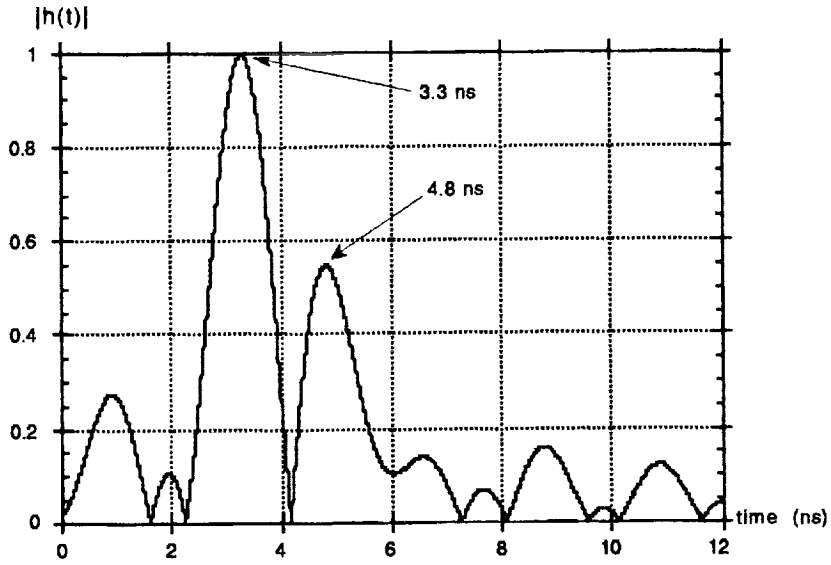

Figure 5.3.6 Normalized Inverse FFT of 100 measurements of the reflection coefficient at the input port of the MRIS test apparatus shown in figure 5.3.4. The bandwidth used in this measurement is 500 MHz, and the target range is 2.25".

5.4 Optimal Signal Processing of the Experimental Measurements

This chapter presents the results of applying the globally optimal signal processing technique derived in section 5.2 on physical measurements. The processing technique is globally optimal in the sense that the minimized objective function (5.1.5) has many local minima and a search procedure is used to find the absolute minimum. This global minimum determines the best

set of reflection amplitudes and delays given the frequency data and assuming that the radar channel has distinctly reflective scatterers.

Consider the objective function (5.1.5) for two assumed delays, one scanned from 0-0.8 ns along one delay dimension and the other from 0.06-0.1 ns using the Beatty Standard data and 18 GHz bandwidth. This function may be interpreted as a surface above the "delay" plane as shown in figure 5.4.1. It is very important to recognize that every value of $J(t_i, t_j)$ is the result of solving (5.2.9) using each delay pair t_i, t_j in the domain shown. The surface shown in figure 5.4.1 has a single global minimum which corresponds the optimum delay pair (t_1 = 83 ps, t_2 = 583 ps). The grooves in the objective function extend along the delay axes. The deeper groove at 0.083 ns is due to the larger amplitude reflection caused by the first discontinuity of the Beatty Standard coaxial line (amplitude = -0.3333). The groove at 0.583 ns is due to the slightly smaller amplitude reflection from the second discontinuity (amplitude = 0.297). The surface has multiple local minima, hence a simple descent algorithm will fail, in general, to locate the global minimum. One approach that will be demonstrated here is to use a grid search algorithm on the objective function. Grid search is a method of finding the global minimum by finding the least value of J along one delay dimension while holding the other delay fixed. Then, once the least value of J is found in that dimension, the corresponding delay is held fixed, and the search is performed along the other dimension. By performing multiple iterations in this fashion, the global minimum is found once the delays are no longer updated. The global minimum for the 18 GHz case (figure 5.4.1) was found in two iterations to be t_1 = 0.082 ns, t_2 = 0.588 ns, very close to both the theoretical delays as well as the estimates produced by the IFFT approach.

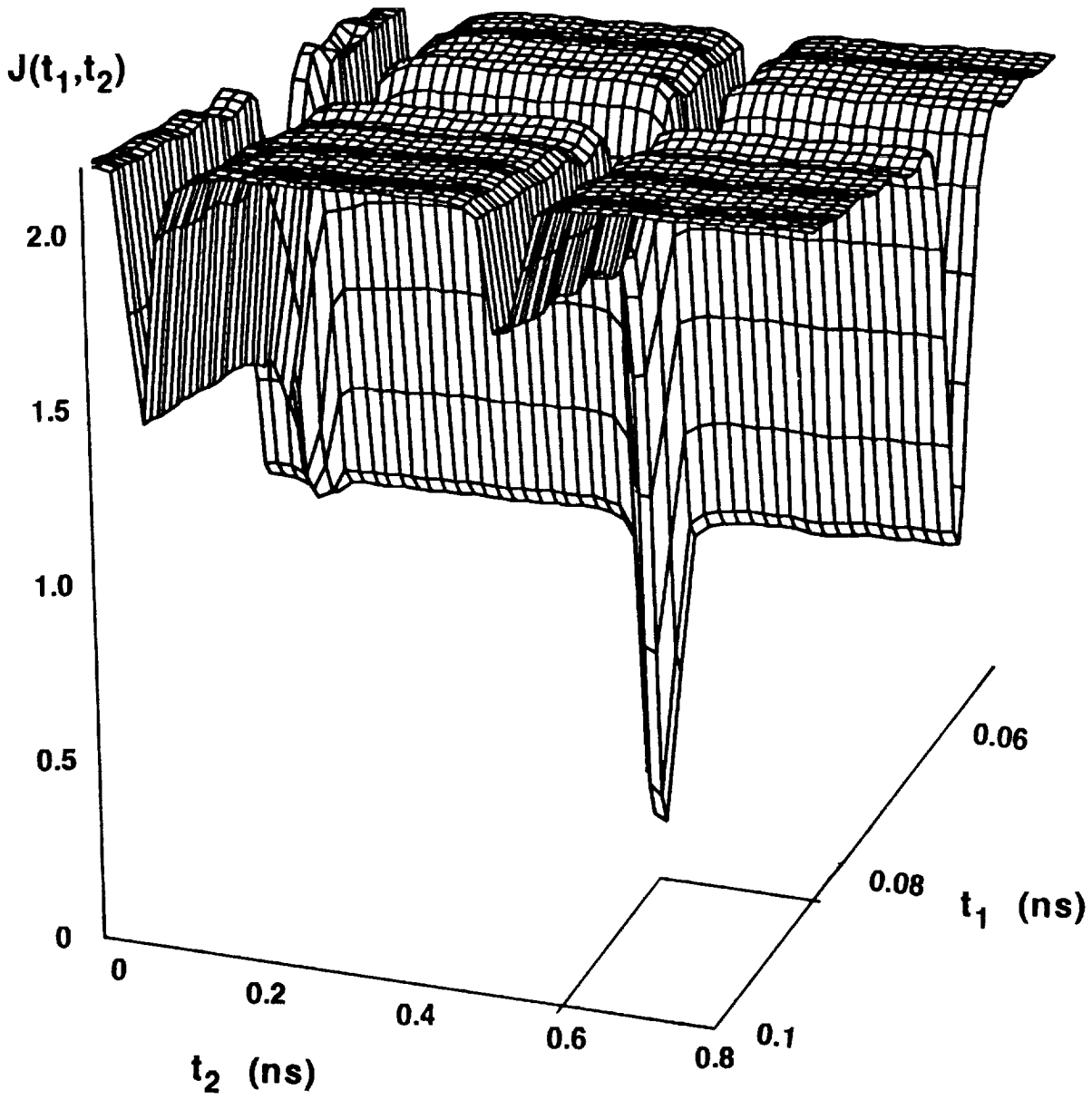

Figure 5.4.1 Amplitude optimized objective function constructed from 801 reflection coefficient measurements of the Beatty Standard (figure 5.3.1) using a bandwidth of 18 GHz.

The more interesting case occurs when the bandwidth is reduced to 2 GHz and the IFFT is useless for determining the range to either of the first two reflections. Applying the optimal signal processing algorithm to the frequency data for this case results in the objective function illustrated in figure 5.4.2. There still exist grooves in the objective function. However there are several grooves whose minima lie between the values 0.083 ns and 0.583 ns. There does exist a single global minimum in this domain and the delay values obtained using grid search to find it are .082 ns and 0.587 ns, which is more accurate than the delay estimates produced by the IFFT for 18 GHz bandwidth. The impulse response generated by the optimization approach is shown in figure 5.4.3. This result alone shows the resolution enhancement offered by the optimization approach over the standard IFFT as used by the HP 8510 network analyzer.

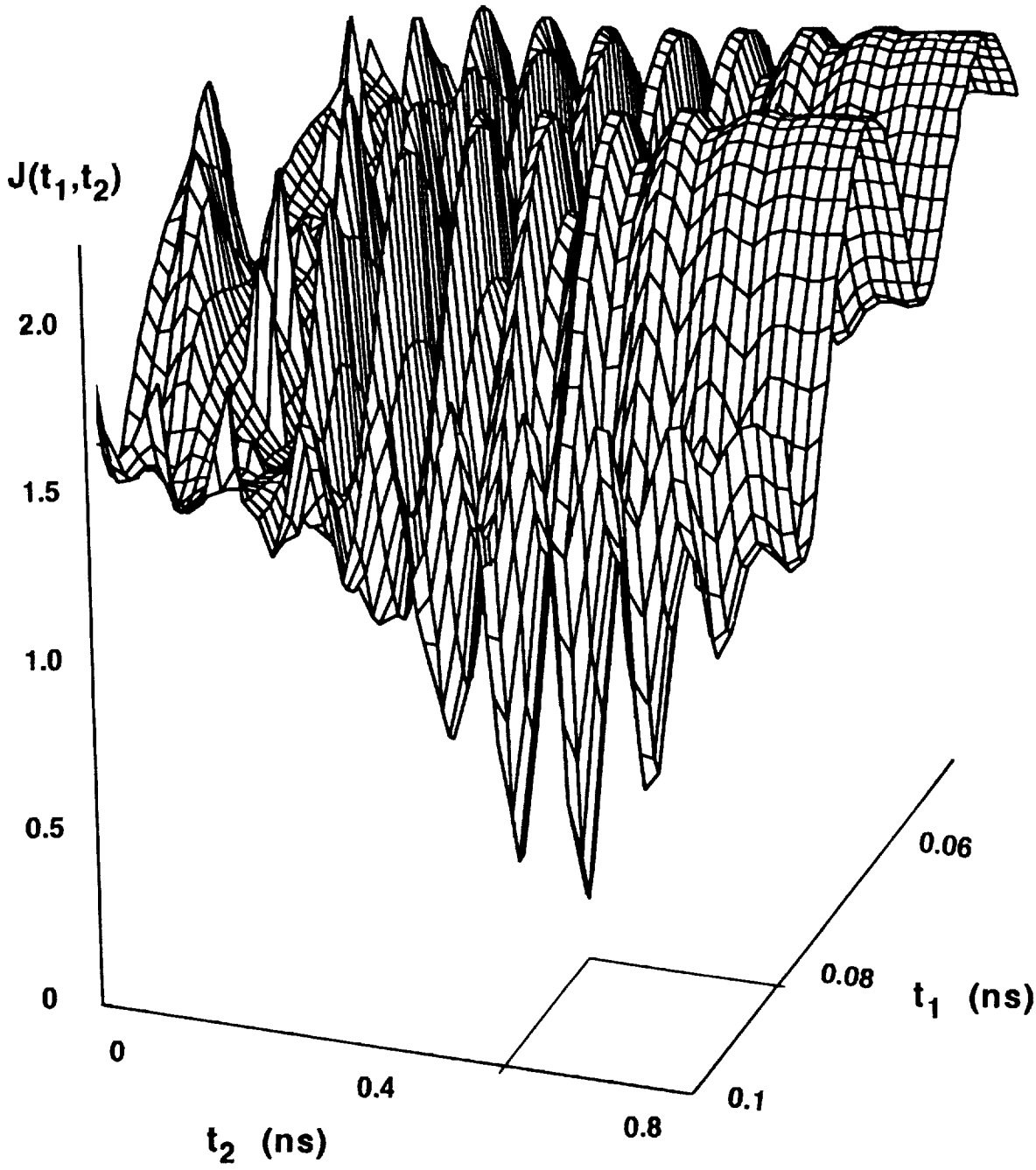

Figure 5.4.2 Amplitude optimized objective function constructed from 801 reflection coefficient measurements of the Beatty Standard (figure 5.3.1) using a bandwidth of 2 GHz.

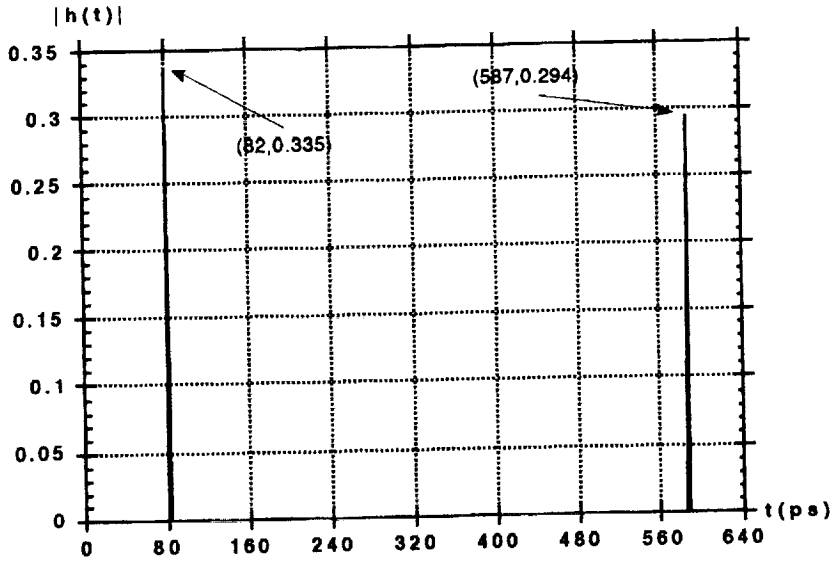

Figure 5.4.3 Impulse response of the Beatty Standard obtained using grid search (3 iterations) on the amplitude-optimized objective function resulting from 2 GHz bandwidth HP8510 measurements.

A more impressive set of results is obtained from the radar measurements of the MRIS test apparatus of figure 5.3.4. The objective function surface for 801 measurements over a 4 GHz bandwidth is shown in figure 5.4.4. This surface clearly shows grooves along the delay axes. The domain of this plot was chosen to display the symmetry of the objective surface. As shown, there are two global minima one with $t_1 = 3.47$ ns, $t_2 = 5.43$ ns and the other with $t_1 = 5.43$ ns, $t_2 = 3.47$ ns, which are exactly the same solution to the problem. Now consider the case of only 100 measurements spanning a bandwidth of only 500 MHz. The IFFT produced the meaningless result shown in figure 5.3.6. The optimization approach produces the objective surface shown in figure 5.4.5.

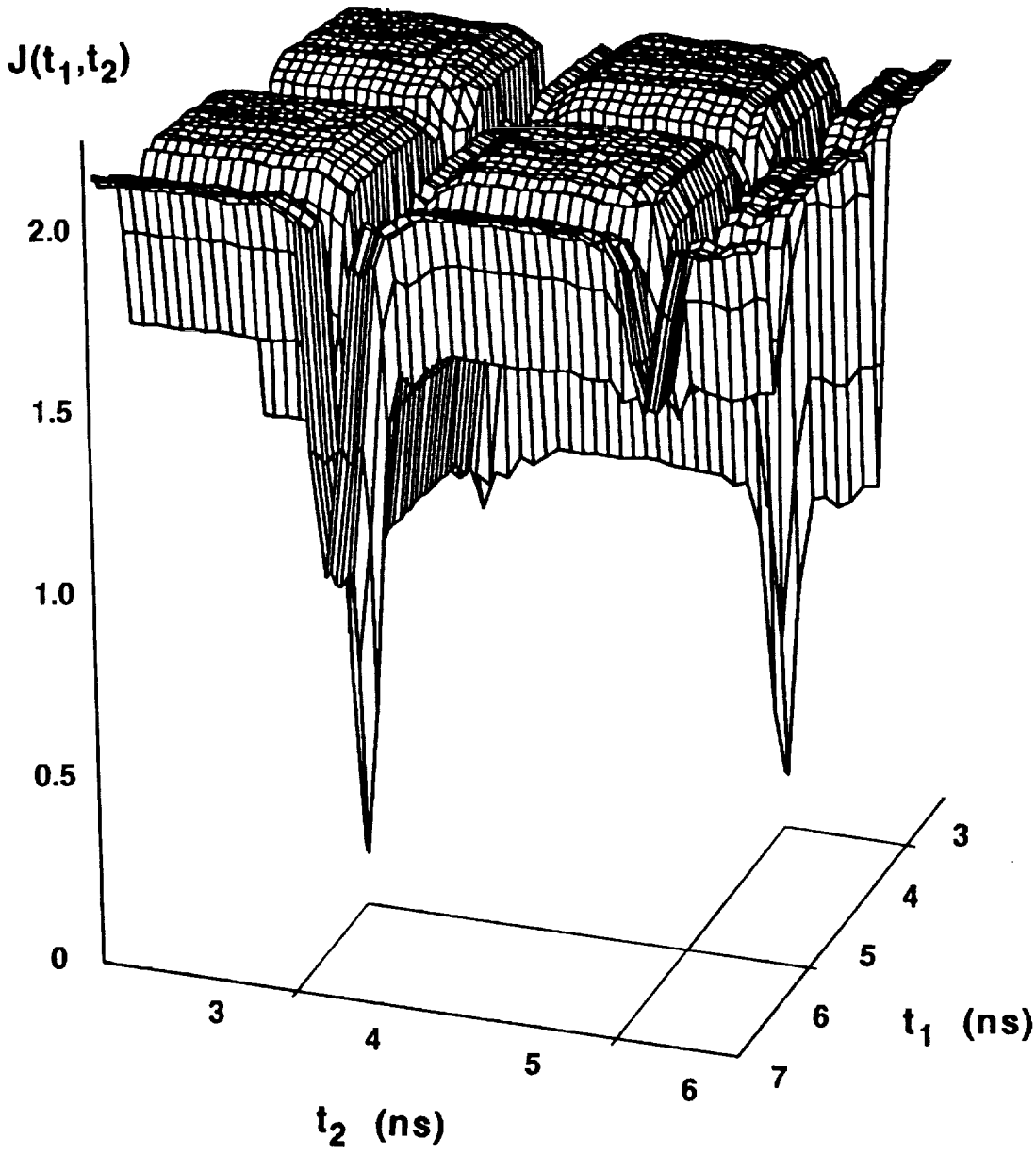

Figure 5.4.4 Amplitude optimized objective function constructed from 801 reflection coefficient measurements of the MRIS test apparatus (figure 5.3.1) using a bandwidth of 4 GHz. Target is at a distance of 12" from the outer surface of the quartz glass.

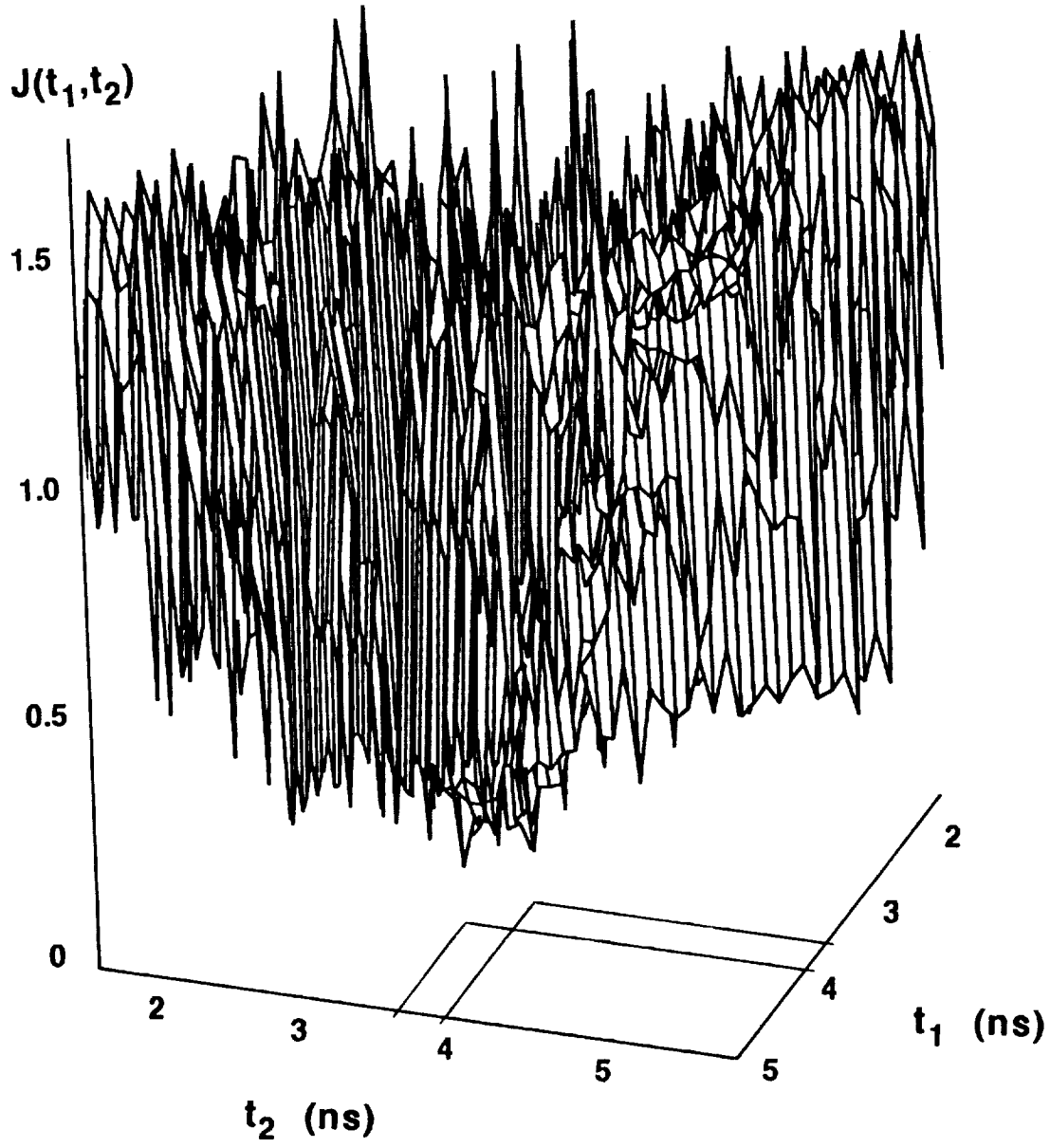

Figure 5.4.5 Amplitude optimized objective function constructed from 801 reflection coefficient measurements of the MRIS test apparatus (figure 5.3.4) using a bandwidth of 500 MHz. Target is at a distance of 2.25" from the outer surface of the quartz glass.

This objective function surface may appear to lack structure. However, the surface has grooves running along the delay axes which can be scanned successfully using the grid search algorithm. Evidence of these grooves may be seen by carefully examining the right half of the surface. The ridges in the surface indicate the presence of the grooves. The surface also possesses a macroscopic bowl shape, albeit very "noisy," in the domain shown. There are two global minima, either of which produces the delay estimates t_1 = 3.53 ns, t_2 = 3.95 ns. These delay values were found by polishing the result of a first-pass grid search with an additional grid search. In the first pass, the domain scanned was 1-6 ns in each delay dimension using 50 ps increments. After 16 iterations of grid search, the resulting time delays are t_1 = 3.55 ns, t_2 = 3.95 ns. Then, a second pass was performed over the domain 3.5-3.6 ns in the first delay dimension and 3.9-4.0 ns in the second delay dimension using 1 ps increments. After 12 iterations of grid search in the second pass, the resulting time delays are t_1 = 3.53 ns, t_2 = 3.95 ns. The impulse response produced by the optimization technique is shown in figure 5.4.6.

One interesting observation that should be made is the that the estimate of the time delay to the quartz glass is larger (3.53 ns) for the 500 MHz case than for the 4 GHz case (3.45 ns, see figure 5.3.5). Thus, it appears that the glass has moved in range. The cause of the 80 ps additional delay is due to the fact that the frequency scan in the 500 MHz case is from 14 GHz to 14.5 GHz, a band whose average frequency is less than the average frequency for the 4 GHz case which scanned from 14-18 GHz. Hence, from (5.3.2) the average group velocity is less for the 500 MHz sweep than for the 4 GHz sweep, and a longer time delay to the glass is expected.

The most important measurement is the difference in time delay between the two reflections. This delay difference is found to be t_2-t_1 = 0.42 ns. The theoretical value was calculated to be 0.422 ns. Hence, a delay error of only 2 ps is produced by the optimization approach in this case. This 2 ps error in the delay estimate corresponds to approximately 0.3 mm. This result clearly shows the resolution capability of the optimization approach. The IFFT for this measurement case (figure 5.3.6) was totally useless for determining the range to any reflection while the optimization approach has distinctly and accurately resolved both the reflection from the metal plate target as well as the reflection from the quartz glass.

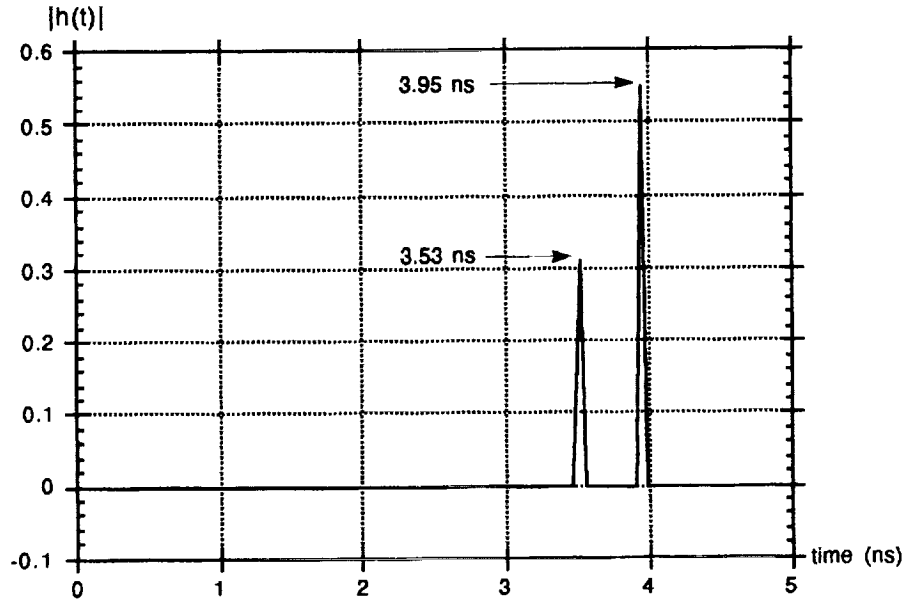

Figure 5.4.6 Normalized Impulse response of the MRIS test apparatus of figure 5.3.4 obtained using grid search (16 iterations, 14 iterations polished) on the amplitude-optimized objective function resulting from 500 MHz bandwidth HP8510 measurements. Target range is 2.25".

The results for the IFFT and optimization approaches for both the Beatty Standard and MRIS experiments are presented in the tables below.

Table 5.4.1 Comparison of reflection delay estimates produced by the IFFT and optimization approaches for the Beatty Standard.

BW = 18 GHz, n=801 measurements	Theoretical	IFFT	Optimization
Time delay to the first reflection:	83 ps	82 ps	82 ps
Time delay to the second reflection:	583 ps	585 ps	588 ps
BW = 2 GHz, n=801 measurements	Theoretical	IFFT	Optimization
Time delay to the first reflection:	83 ps	N/A*	82 ps
Time delay to the second reflection:	583 ps	N/A*	587 ps

Table 5.4.2 Comparison of target delay estimates produced by the IFFT and optimization approaches for the MRIS test apparatus. The distance from the outer surface of the quartz glass to the metal plate target is 12" for the 4 GHz case and 2.25" for the 500 MHz case. All time delays shown are two-way travel times from the center of the quartz glass to the metal plate.

BW = 4 GHz, n=801 measurements	Theoretical	IFFT	Optimization
Time delay from the quartz glass to the metal plate target:	2.073 ns	1.97 ns	1.96 ns
BW = 500 MHz, n=100 measurements	Theoretical	IFFT	Optimization
Time delay from the quartz glass to the metal plate target:	0.422 ns	N/A*	0.420 ns

* It is not clear from the IFFT results that there are two reflections. Even if two reflections are assumed, the time delays to the peaks in the IFFT results are erroneous to the point of being meaningless.

An existing parametric technique called the Matrix Pencil Method [Hua, Maricevic] was designed to recover amplitude-delay pairs from frequency domain data. The Matrix Pencil Method has been shown to perform significantly better than the IFFT approach. The results presented in this chapter for the optimization approach applied to the Beatty Standard are comparable to those presented for the Matrix Pencil Method [Maricevic]. However, the optimization approach is much more general. For example, time-gating [Artech84,87] can be implemented easily in the optimization approach. This is equivalent to searching only over certain regions in the delay plane. No physical constraints such as time-gating can be implemented in the Matrix Pencil Method without a significant modification in its derivation.

5.5 Summary

This chapter has presented the derivation and demonstration of a new algorithm for processing radar data produced by any frequency-stepped CW system. The derivation is based on minimizing the two-norm of the difference between the sequence of measured reflection coefficients and those produced by a model which assumes that the echoes from the radar channel are impulses in the time domain. A performance comparison between the IFFT and optimal processing techniques was presented in the context of two physical measurement sets. In the first set, the Beatty standard was terminated in a matched load and driven by an HP 8510 network analyzer. The measurement bandwidth was reduced from 18 GHz to 2 GHz and it was shown that while the IFFT produced meaningless reflection range estimates in the 2 GHz case, the

optimal processing approach was able to clearly resolve the reflections and the resulting reflection range estimates were more accurate using 2 GHz bandwidth than those produced by the IFFT using 18 GHz. In the second set of measurements, an MRIS test apparatus was also driven by an HP 8510 network analyzer. In this set of measurements the bandwidth, target range and the number of measurements were all reduced. First, the metal plate target was set at a range of 12" and 801 measurements spanning a total bandwidth of 4 GHz were analyzed using both the IFFT and optimal processing algorithms. The target range estimates resulting from both methods were of equal accuracy. Then the target was set to a range of 2.25", the number of measurements was reduced to 100 and the bandwidth was reduced to only 500 MHz. The range resolution and accuracy deterioration produced by IFFT processing was clearly evident. In this case, the IFFT could not distinguish the presence of two reflections nor could it determine accurately the range to either the interfering reflection or the metal plate target. However, the optimal processing approach could not only resolve the two reflections but could estimate both of their ranges with high accuracy. This result demonstrates the resolution enhancement offered by the optimal processing approach over IFFT processing.

Chapter 6

Conclusions and Future Research

This dissertation provides three original contributions to the field of microwave-millimeterwave radar. A model for electromagnetic planewave propagation in inhomogeneous media was derived in chapter 2 and its performance illustrated in the context of modelling EM propagation in non-uniform electron plasmas. This model is based on the theory of transmission lines and represents an inhomogeneous medium by thin cascaded slabs, each of which is homogeneous but whose combined structure is inhomogeneous. It has been shown that as the thickness of each slab is reduced, the response from the model asymptotically approaches the true physical response. The model can be implemented very efficiently using advanced computer programming techniques such as recursive programming which allow the use of hundreds of thousands of slabs while requiring little computation time.

A new formulation for the frequency-stepped double sideband suppressed carrier radar system was derived in Chapter 3. This reformulation included the effect of an interfering reflection. Simulation results were presented which illustrate that the DSBSC radar system is capable of accurate target range estimation even when the echo from the target is much weaker than the echo from the interferer.

A new globally optimal signal processing algorithm was derived in Chapter 5 for processing radar data produced by the frequency-stepped CW system. A non-linear least squares objective function is formulated, and its absolute minimum yields both the delay times and amplitudes of the reflections

from the target and any reflective interferer. The performance of the algorithm is demonstrated using physical radar data and it is shown to produce accurate and highly resolved target range estimates even when the bandwidth is reduced well beyond the point where the standard IFFT approach fails.

Several simulation results have been presented in the context of measuring non-uniform electron plasma densities that develop near the heat tiles of a space re-entry vehicle. Unfortunately, an appropriate plasma profile cannot be produced for ground testing. Hence, with the exception of performing an actual atmospheric aeropass, their measurement can only be performed by computer simulation. For this reason, the inhomogeneous media model derived in this dissertation, which can simulate accurately the propagation of planewaves in an electron plasma, is especially significant.

Several research problems are generated by the work presented in this dissertation. The inhomogeneous media model should be extended to include oblique incidence which will require the effects of polarization to be included as well. In [Pozar] the transmission line analogy for EM planewave propagation through dielectric slabs is extended to include oblique incidence. Hence, the framework for extending the cascaded slab model to include oblique incidence already exists. Another extension of interest would be the inclusion of antenna radiation pattern [Jordan, Silver]. The MRIS system described in Chapter 1 utilizes a circular horn antenna mounted behind the heat tiles of the AFE spacecraft. The radiation transmitted into the propagation path is approximated by planewaves incident normally on each of the media layers. However, because the antenna is so close to these media layers, the radiation is actually composed of spherical waves and therefore much of the radiation is obliquely

incident on the layer boundaries. The intensity of radiation as a function of angle constitutes the antenna radiation pattern and must be included in the inhomogeneous media model for a truly accurate representation of the physical measurement.

In the derivation of the DSBSC system in Chapter 2, as well as the stepped CW system in Chapter 3, it was tacitly assumed that both the target and interferer are stationary. If either the target or interferer move significantly during the time in which a measurement is made, the received echoes will contain a Doppler shift. The effect of target motion on the measurements made by these radar systems remains to be explored. Standard radar techniques such as pulsed radar, extract target velocity from the Doppler shifted echo. It is expected that target velocity estimation may be achieved by both frequency-stepped radars examined in this dissertation. However, this remains to be shown.

The DSBSC system was derived for exactly two reflections, one from the target and one from the interferer. This derivation provides a significant improvement in the applicability of the DSB technique. However, the technique should be generalized to include the effects of several reflections.

The derivation of the optimal signal processing algorithm in Chapter 5 for the stepped CW system made no assumption about the number of reflections. However, the simulations presented examined only the case of extracting two reflections from the radar data. For the case of two reflections, it was demonstrated that a simple grid search procedure can be used to find the global minimum of the objective function. The optimization process should be investigated for an arbitrary number of reflections. It is likely that the simple grid

search technique will fail in the more general case. A more sophisticated search technique, such as simulated annealing [Bev], may be required.

There may be applications for the two radar systems presented in this dissertation for which the propagation path induces significant noise in the radar measurements. This issue has not been addressed and remains as future research.

Chapter 7

References

[Ahn] S, Ahn, and A.K. Jordan, "Profile Inversion of Simple Plasmas and Non-Uniform Regions: Three-Pole Reflection Coefficient," *IEEE Transactions on Antennas and Propagation*, Nov. 1976.

[Artech84] Artech House, *Techniques of Radar Reflectivity Measurement*, Norwood, MA, 1984.

[Artech87] Artech House, *Principles and Applications of Millimeterwave Radar*, Norwood, MA, 1987.

[Bahar] E. Bahar, "Generalized WKB Method with Application to Problems of Propagation in Inhomogeneous Media," *Journal of Mathematical Physics*, vol 8, 1967.

[Balanis1] G.N. Balanis, "The Plasma Inverse Problem," *Journal of Mathematical Physics*, vol. 13, 1972.

[Balanis2] G.N. Balanis, "Plasma Density Determination," *IEEE Transactions on Antennas and Propagation*, vol. AP-22, 1974.

[Beatty] R.W. Beatty, "Calculated and Measured S11, S21, and Group Delay for Simple Types of Coaxial and Rectangular Waveguide 2-Port Standards," *National Bureau of Standards Technical Note* 657, U.S. Department of Commerce, Boulder, CO, December 1974.

[Bev] P.R. Bevington, *Data Reduction and Error Analysis for the Physical Sciences*, McGraw-Hill, New York, 1969.

[Bird] G.J. Bird, *Radar Precision and Resolution*, Wiley, NY.

[Bolomey] J.C. Bolomey, C. Durix, and D. Lesslier, "Determination of Conductivity Profiles by Time-Domain Reflectometry," *IEEE Transactions on Antennas and Propagation*, vol. 27, March 1979.

[Boyer] W.D. Boyer, "A Diplex, Doppler Phase Comparison Radar," *IRE International Convention Record*, 1962.

[Brown] R.G. Brown, R.A. Sharpe, Et. Al., *Lines, Waves, and Antennas*, Ronald Press, NY, 1973.

[Chen] F.F. Chen, *Plasma Physics and Controlled Fusion*, Plenum Press, NY, 1984.

[Collin] R.E. Collin, *Foundations of Microwave Engineering*, McGraw Hill, NY, 1966.

[Collins] Collins Publishers, *Modern Radar Technology*, London, 1987.

[Compton] R.T. Compton, *Adaptive Antennas: Concepts and Performance*, Prentice-Hall, Englewood Cliffs, NJ 1988.

[CRC] W.H. Beyer ed., *CRC Standard Mathematical Tables*, 25th Ed., CRC Press Inc, West Palm Beach, FL, 1978.

[Davies1] K. Davies, *Ionospheric Radio*, Peregrinus on Behalf of IEEE, London, 1990.

[Davies2] K. Davies, *Ionospheric Radio Propagation*, Peregrinus on Behalf of IEEE, London, 1990.

[Davies3] K. Davies, *Ionospheric Radio Waves*, Blaisdell Publishing Co., Waltham MA, 1969.

[Devlin] J.C. Devlin, P.L. Dyson, and P.R. Hammer, "A Pulse Synthesis Technique for Improving Ionosonde Resolution," *Radio Science*, Vol. 12, 1977.

[Dworsky] L.N. Dworsky, *Modern Transmission Line Theory and Applications*, John Wiley and Sons, 1979.

[Eden] P. Edenhofer, J.N. Franklin, and C.H. Papas, "A New Inversion Method in Electromagnetic Wave Propagation," *IEEE Transactions on Antennas and Propagation*, March 1973.

[EMS] Electromagnetic Sciences, "Proposal for the MRIS Distance Measurement System," Marrietta GA, 1988.

[Giraud] A. Giraud, *Ionospheric Techniques and Phenomena*, Reidel Publishing Co., Boston MA, 1978.

[Glisson] T.H. Glisson, Introduction to System Analysis, McGraw-Hill Inc., 1985.

[Golub] G.H. Golub, and C.F. Van Loan, *Matrix Computations*, Johns Hopkins University Press, Baltimore MD, 1989.

[Grimes] D.M. Grimes, and T.O. Jones, "Automotive Radar, A Brief Review," *Proceedings of the IEEE*, vol. 62, June 1974.

[Harrington] R.F. Harrington, *Time-Harmonic Electromagnetic Fields*, McGraw-Hill, New York, 1961.

[Halsted] Halstead Press, *Detection and Estimation: Applications to Radar*, Straudsburg, PA, 1976.

[Harris] F.J. Harris, "On the Use of Windows for Harmonic Analysis with the Discrete Fourier Transform," *Proceedings of the IEEE*, vol. 66, January 1978.

[Hearn] C.P. Hearn, C.R. Cockrell, and S.D. Harrah, "An Analysis of the Effects of Spurious Reflections in the MRIS Distance-Measurement System," *NASA Technical Report*, 1990.

[HP] *HP 8510 Network Analyzer Operating and Programming Manual*, Hewlett-Packard Company, Santa Rosa, CA, 1984.

[Hua] Y. Hua, and T.K. Sarkar, "Matrix Pencil Method for Estimating Parameters of Exponentially Damped/Undamped Sinusoids in Noise," *IEEE Transactions on Acoustic Speech and Signal Processing*, vol. 38, No. 5, May 1991.

[IEEE] IEEE Press, *Advances in Radar Technology*, London, 1985.

[Jordan] E.C. Jordan and K.G. Balmain, *Electromagnetic Waves and Radiating Systems*, Prentice-Hall, Englewood Cliff, NJ, 1968.

[Kay 81] S.M. Kay, and S.L. Marple, "Spectrum Analysis--A Modern Perspective," *Proceedings of the IEEE*, vol. 69, November 1981.

[Kay 88] S.M. Kay, *Modern Spectral Estimation: Theory and Application*, Prentice-Hall, Englewood Cliffs, NJ, 1988.

[Kelley] M.C. Kelley, *The Earth's Ionosphere: Plasma Physics and Electrodynamics*, Academic Press, San Diego, CA, 1989.

[Keuster] E.F. Kuester, and D.C. Chang, "Propagation, Attenuation, and Dispersion Characteristics of Inhomogeneous Dielectric Slab Waveguides," *IEEE Transactions on Microwave Theory and Techniques*, vol MTT-23, no. 1, Jan. 1975.

[Lawson] C.L. Lawson, and R.J. Hanson, *Solving Least Squares Problems*, Prentice-Hall, 1974.

[LePage] W.R. LePage, and S. Seely, *General Network Analysis*, McGraw-Hill, New York, 1952.

[Lesselier] D. Lesselier, "Determination of Index Profiles by Time Domain Reflectometry," *Journal of Optics*, vol. 9, pp. 349-358, 1978.

[Makhoul] J. Makhoul, "Linear Prediction--A Tutorial Review," *Proceedings of the IEEE*, vol. 63, no. 4, April 1975.

[Maricevic] Z.A. Maricevic et al., "Time-Domain Measurements with the Hewlett-Packard Network Analyzer HP 8510 Using the Matrix Pencil Method," *IEEE Transactions on Microwave Theory and Techniques*, vol. 39, NO. 3, March 1991.

[Marple] S.L. Marple, *Digital Spectral Analysis with Applications*, Prentice-Hall, Englewood Cliffs, NJ, 1987.

[Mess] D.G. Messerschmitt, "Transmission Line Modeling Program Written in C," *IEEE Transactions on Selected Areas in Communications*, Vol. SAC-2, pp. 148-153, January 1984.

[Meyer] D.P. Meyer, *Radar Target Detection*, Academic Press, NY, 1973.

[Miller] E.K. Miller, *Time Domain Measurements in Electromagnetics*, Van Nostrand Reinhold, NY, 1986.

[Most] M. Mostafavi, and R. Mittra, "Remote Probing of Inhomogeneous Media using Parameter Optimization Techniques," *Radio Science*, vol. 7, Dec. 1972.

[Nilssen] O.K. Nilssen, and W.D. Boyer, "Amplitude Modulated CW Radar," *IRE Transactions on Aerospace and Navigational Electronics*, December 1962.

[Noble] B. Noble, and J.W. Daniel, *Applied Linear Algebra*, Prentice-Hall, Englewood Cliffs, NJ, 1977.

[Opp] A.V. Oppenheim and R.W. Schafer, *Digital Signal Processing*, Prentice-Hall, 1975.

[Pozar] D.M. Pozar, *Microwave Engineering*, Addison-Wesley, 1990.

[Press] W.H. Press Et. Al., *Numerical Recipes in C*, Cambridge University Press, NY, 1988.

[Richmond] J.H. Richmond, "Transmission Through Inhomogeneous Plane Layers," *IRE Transactions on Antennas and Propagation*, May 1962.

[Riden] L.N. Ridenour, *Radar System Engineering*, Radiation Laboratory Series, Vol. 1, Ch. 5, McGraw-Hill Book Co., New York, 1947.

[Rybak] J.P. Rybak, and R.J. Churchill, "Progress in Reentry Communications," *IEEE Transactions on Aerospace and Electronic Systems*, vol. AES-7, no. 5, September 1971.

[Silver] S. Silver, *Microwave Antenna Theory and Design*, McGraw-Hill, New York, 1949.

[Skolnik] M.I. Skolnik, *Radar Handbook*, McGraw Hill Book Company, New York, NY, 1970.

[Sobelman] G.E. Sobelman, D.E. Krekelberg, *Advanced C Techniques and Applications*, Que Corporation, Indianapolis, IN, 1985.

[Sund] A. Sundarabu, *Fundamentals of Radar*, Asia Publishing House, NY, 1972.

[Van] Van Nostrand Reinhold, *Principles of Modern Radar*, NY, 1986.

[Wehner] D.R. Wehner, *High Resolution Radar*, Artech House, Norwood, MA, 1987.

[Ybarra1] G.A. Ybarra, S.H. Ardalan, R.E. Marshall, and R.T. Neece, "Performance Comparison of the Stepped Carrier and Stepped DSBSC MRIS Distance Measurement Systems," *NASA Contractor Final Report*, Sept., 1990.

[Ybarra2] G.A. Ybarra, S.H. Ardalan, C.P. Hearn, R.E. Marshall, and R.T. Neece, "Detection of Target Distance in the Presence of an Interfering Reflection Using a Double Side-Band Suppressed Carrier Microwave Radar System," *IEEE Transactions on Microwave Theory and Techniques*, May, 1991.

[Ybarra3] G.A. Ybarra, S.H. Ardalan, R.E. Marshall, and R.T. Neece, "Measurement of Non-Uniform Plasma Densities Developed During Space Vehicle Atmospheric Re-entry using a Millimeterwave Radar System," *Proceedings of the IEEE Int. Conf. on Geoscience and Remote Sensing*, June, 1991.

[Ybarra4] G.A. Ybarra, S.H. Ardalan, R.E. Marshall, and R.T. Neece, "Measurement of Electron Plasma Densities Developed During Space Vehicle Atmospheric Re-entry using a Stepped Double Sideband Suppressed Carrier Millimeterwave Radar System," *Proceedings of the IEEE Union of Radio Science*, July, 1991.

Chapter 8

Appendix: Derivation of Equation 3.2.14

$$F(x) = \int \frac{a+b\cos(x)}{c+d\cos(x)}\,dx = \frac{bx}{d} + \frac{2\left(a - \frac{bc}{d}\right)}{\sqrt{c^2 - d^2}} \tan^{-1}\left(\frac{\sqrt{c^2 - d^2}\,\tan\left(\frac{x}{2}\right)}{c + d}\right) \qquad (8.1)$$

Proof:

A substitution of variables will be made which will transform the trigonometric polynomial integrand of F(x) into a rational polynomial. Let

$$u = \tan\left(\frac{x}{2}\right) \qquad (8.2a)$$

This produces

$$x = 2\tan^{-1}u \qquad dx = \frac{2}{1+u^2}\,du \qquad (8.2b)$$

and

$$\cos(x) = \cos(2\tan^{-1}u) = 1 - 2\sin^2(2\tan^{-1}u) = 1 - 2\sin^2\left(\sin^{-1}\left(\frac{u}{\sqrt{1+u^2}}\right)\right) \qquad (8.3)$$

$$\cos(x) = 1 - \frac{2u^2}{1+u^2} = \frac{1-u^2}{1+u^2} \qquad (8.4)$$

F(x) may be decomposed into two simpler functions $F_1(x)$ and $F_2(x)$.

$$\int \frac{a+b\cos(x)}{c+d\cos(x)}\,dx = a\int \frac{dx}{c+d\cos(x)} + b\int \frac{\cos(x)}{c+d\cos(x)}\,dx = F_1(x) + F_2(x) \qquad (8.5)$$

Transforming the function $F_1(x)$ into the function $F_1(u)$ using the transformation (8.2) yields

$$F_1(u) = a\int \frac{\frac{2}{1+u^2}}{c+d\left(\frac{1-u^2}{1+u^2}\right)}\,du = 2a\int \frac{du}{c(1+u^2)+d(1-u^2)} \tag{8.6}$$

$$F_1(u) = 2a\int \frac{du}{c+d+(c-d)u^2} = \frac{2a}{c-d}\int \frac{du}{\frac{c+d}{c-d}+u^2} \tag{8.7}$$

Recognizing the integrand of (8.7) as a having the familiar derivative relation

$$\frac{d}{du}\tan^{-1}\left(\frac{u}{\beta}\right) = \frac{\beta}{\beta^2+u^2}\,du \tag{8.8}$$

allows $F_1(u)$ to be expressed as

$$F_1(u) = \frac{2a}{c-d}\sqrt{\frac{c-d}{c+d}}\tan^{-1}\left(u\sqrt{\frac{c-d}{c+d}}\right) \tag{8.9}$$

Simply replacing the variable u with tan(x/2) gives

$$F_1(x) = \frac{2a}{\sqrt{c^2-d^2}}\tan^{-1}\left(\frac{\sqrt{c^2-d^2}\tan\left(\frac{x}{2}\right)}{c+d}\right) \tag{8.10}$$

Now transforming the function $F_2(x)$ into the function $F_2(u)$ using the transformation (8.2) yields

$$F_2(u) = b\int \frac{\frac{1-u^2}{1+u^2}}{c+d\left(\frac{1-u^2}{1+u^2}\right)}\frac{2}{1+u^2}du = 2b\int \frac{1-u^2}{(c(1+u^2)+d(1-u^2))(1+u^2)}du \tag{8.11}$$

$$F_2(u) = \frac{2b}{c-d}\int \frac{1-u^2}{\left(\frac{c+d}{c-d}+u^2\right)(1+u^2)}du \tag{8.12}$$

The integrand of (8.12) may be decomposed into two simpler functions using partial fraction expansion giving

$$F_2(u) = \frac{2b}{c-d}\int \frac{A}{\left(\frac{c+d}{c-d}+u^2\right)}du + \frac{2b}{c-d}\int \frac{B}{(1+u^2)}du \tag{8.13}$$

where the constants **A** and **B** are easily determined to be

$$A = \frac{-c}{d} \qquad B = \frac{c-d}{d}$$

Inserting these coefficients into (8.13) gives

$$F_2(u) = \frac{-2bc}{d(c-d)}\int \frac{du}{\left(\frac{c+d}{c-d}+u^2\right)} + \frac{2b}{d}\int \frac{1}{(1+u^2)}du \tag{8.14}$$

The first anti-derivative in (8.14) is identical to (8.7) and the second is easily evaluated using the derivative relation (8.8) yielding

$$F_2(u) = \frac{-2bc}{d(c-d)}\sqrt{\frac{c-d}{c+d}}\tan^{-1}\left(u\sqrt{\frac{c-d}{c+d}}\right) + \frac{2b}{d}\tan^{-1}(u) \qquad (8.15)$$

Once again substituting u=tan(x/2)

$$F_2(x) = \frac{-2bc}{d\sqrt{c^2-d^2}}\tan^{-1}\left(\frac{\sqrt{c^2-d^2}\tan\left(\frac{x}{2}\right)}{c+d}\right) + \frac{bx}{d} \qquad (8.16)$$

Combining $F_1(x)$ with $F_2(x)$ completes the proof.